DEPARTMENT OF CHEMISTRY, UNIVERSITY OF JYVÄSKYLÄ
RESEARCH REPORT No. 166

COMPUTATIONAL INVESTIGATIONS ON ROTATIONAL AND VIBRATIONAL SPECTROSCOPIES OF SOME DIATOMICS IN SOLID ENVIRONMENT

BY
JOHAN LINDGREN

Academic Dissertation
for the Degree of
Doctor of Philosophy

To be presented, by permission of the Faculty of Mathematics and Natural Sciences of the University of Jyväskylä, for public examination in Auditorium KEM-4 of the University of Jyväskylä on June 28, 2013 at 12 noon

Jyväskylä, Finland
ISBN 978-951-39-5245-7
ISSN 0357-346X

Preface

The work presented in this thesis was done at the Department of Chemistry at the University of Jyväskylä during the years 2009-2013. The financial support from the Academy of Finland is greatly appreciated.

First of all, I want to thank Doc. Toni Kiljunen who offered me a position in his group and made this whole thing possible. Throughout my studies, his brilliant scientific knowledge and guidance has been the driving force towards finalization of my work. In this regard, I must especially thank you, Toni, for your patience. I feel privileged to have worked with you.

Special thanks goes to Prof. Mika Pettersson. Most of the experimental work come from the collaboration with him and his group and form the basis of my work. His comments and guidance are greatly appreciated. I wish to thank my colleague Dr. Eero Hulkko and collaborators Dr. Adriana Olbert-Majkut and Dr. Falk Königsmann for conducting the experiments and providing the results.

I am grateful to Dr. Burkhard Schmidt and Prof. Kalle-Antti Suominen for the thorough review of this thesis and for their insightful comments. I extend my gratitude also to Dr. Andre Clayborne for revising the language.

The journey here in the university would have been much harder, if not impossible, without the company I have been travelling with. Especially, the coffeeroom and lunch conversations about senseless topics have always offered a welcomed break from my studies. The people at the Physical Chemistry Department have been supportive and provided a great working environment. I thank my friends which I have met during the years in Jyväskylä, and my "old", childhood friends back in Hollola for keeping me relatively sane.

Last, but most importantly, I thank my whole family for their support during my studies. I thank my "royal barber", my sister Susan, for making me always look dazzling and of course for just being there. Äiti and Isä, your help is the most important thing to me — words are hard to find to express this enough.

Jyväskylä, June 2013

Johan Lindgren

Abstract

In this thesis, spectroscopic and structural properties of homogeneous para-hydrogen crystals and diatomic molecules embedded in rare gas crystals are explored by theoretical means. The agreement with experimental signatures indicates the suitability of the chosen quantum and classical methods to accurately describe the various low-temperature physical and chemical problems investigated at the laser laboratory.

A novel explanation of band structures in Raman and IR spectra is given for CO in Ar. Rotational transition rules are found to dictate the spectral broadening of infrared and Raman band structures as a function of temperature. The results show that after photodissociation of matrix-isolated formaldehyde, the formation of intermolecular complex CO-H_2 becomes energetically unfavourable in the cage of Ar lattice atoms. The molecular photodissociation products, CO and H_2, rotate in lattice sites of varying angular hindrance.

An extensive analysis of long-lived electronic coherences is performed for I_2 in Xe. Quantum beats in time-resolved CARS spectra are reproduced with the help of computed potentials. The predicted 2D (time and frequency) representations of the CARS signals and simulated resonance Raman intensity modulations are shown to complement the demonstration of electronic coherence observed as vibronically resolved absorption spectra. The doublet in resonance Raman progression is assigned to molecular iodine residing in two lattice sites of different geometry. The rapid line broadening of the other peak with increasing vibrational quantum number is explained by coupled rotation-translation dynamics in the crystal site that supports reorientations of the molecular axis. The other site fixes the orientation and maintains longer vibrational coherence.

An analytical model for quantum and polarization beat frequencies in the CARS spectra are presented for CN in Xe. The rotational coherences in the ground and electronic states are studied numerically and a predictive control scheme for the detection and emergence of interferences is introduced.

Nonadiabatic molecular alignment is considered as the underlying mechanism in excitation and probing of rotons in para-hydrogen crystals. The relative orientation between the laboratory frame (pump polarization) and the crystal axes is shown to dictate the roton dynamics observed through the pump-probe optical Kerr effect spectroscopy. The numerical results suggest a control over the spatial composition of the rotons by changing the laser beam focus along the surface plane of the crystal.

Author's address Johan Lindgren
Department of Chemistry
University of Jyväskylä
Finland

Supervisor Docent Toni Kiljunen
Department of Chemistry
University of Jyväskylä
Finland

Reviewers

PD Dr. Burkhard Schmidt
Institute for Mathematics
Freie Universität Berlin
Germany

Prof. Kalle-Antti Suominen
Department of Physics and Astronomy
University of Turku
Finland

Opponent

Prof. Dr. Oliver Kühn
Institute of Physics
Rostock University
Germany

List of publications

The results presented in this thesis are based on the publications and manuscripts listed below and they are herein referred by their Roman numerals (I-V).

I J. Lindgren, A. Olbert-Majkut, M. Pettersson, and T. Kiljunen, Librational motion of CO in solid Ar: Raman and IR spectra and quantum simulations, *Low Temp. Phys.* **38**, 708 (2012).

II J. Lindgren, A. Olbert-Majkut, M. Pettersson, and T. Kiljunen, Raman spectroscopy and crystal-field split rotational states of photoproducts CO and H_2 after dissociation of formaldehyde in solid argon, *J. Chem. Phys.* **137**, 164310 (2012).

III J. Lindgren, E. Hulkko, T. Kiviniemi, M. Pettersson, V. A. Apkarian, and T. Kiljunen, Dynamics Behind the Long-Lived Coherences of I_2 in Solid Xe, *J. Phys. Chem. A*, *accepted* **2013**.

IV J. Lindgren, E. Hulkko, M. Pettersson, and T. Kiljunen, Rotational coherence imaging and control for CN molecules through time-frequency resolved coherent anti-Stokes Raman scattering, *J. Chem. Phys.* **135**, 224514 (2011).

V J. Lindgren and T. Kiljunen, Excitation of rotons in parahydrogen crystals: the intense-field alignment mechanism, *submitted to Phys. Rev. A*.

Author's contribution

Author has done most of the numerical work in Publications I,II, IV, and V, and the wavepacket simulations in III. The author has written the first draft of Publications I and IV, written Publication II, and participated in the writing of III and V. The author also wrote parts of the code in all Publications.

Other contributions

List of Author's other publications which are not included in this thesis:

A1. E. Hulkko, J. Lindgren, T. Kiljunen, and M. Pettersson, Long-Lived Electronic Coherence of Iodine in the Condensed Phase: Sharp Zero-Phonon Lines in the B↔X Absorption and Emission of I_2 in Solid Xe, *J. Phys. Chem. Lett.* **3**, 1847 (2012).

A2. E. Hulkko, J. Ahokas, J. Lindgren, P. Myllyperkiö, and M. Pettersson, Electronic spectroscopy of I_2-Xe complexes in solid Krypton, *J. Chem. Phys.* **136**, 174501 (2012).

CONTENTS

Abbreviations

TISE	time-independent Schrödinger equation
TDSE	time-dependent Schrödinger equation
CARS	coherent anti-Stokes Raman scattering
TIFR	time-integrated frequency-resolved
TGFR	time-gated frequency-resolved
IR	infrared
CW	continuous-wave
RGS	rare gas solid
CFT	crystal-field theory
fcc	face-centered cubic
hcp	hexagonal close-packed
MD	molecular dynamics
FGH	Fourier-Grid-Hamiltonian
FWM	four-wave mixing
RR	resonance Raman
OKE	optical Kerr effect
SS	single-substitution
DS	double-substitution
TS	triple-substitution

1 Introduction

In absorption spectroscopy a photon, provided by a coherent light source such as laser for example, is absorbed by the molecule which becomes energetically excited to a higher state. The excess energy can be released radiatively by an emission of a photon either spontaneously or stimulatively. In the stimulated emission, an incident radiation field induces the emission which leads to creation of an additional photon in the radiation field. The light frequency determines which degrees of freedom are excited during the interaction. Transition between states is most likely to occur in resonance, when the incident frequency matches the energy difference between eigenstates. Another type of transition in molecular systems was recognized in 1928 by Raman [1]. In this case, the incoming photon is scattered from the sample either with higher, lower, or the same wavelength as the incident photon. The intensity for the transition increases dramatically when the field is tuned on-resonance with some higher electronic state. The spectroscopic research field is generally termed as Raman spectroscopy and the transitions between states as Raman transitions. The work presented in this thesis is for most parts based on Raman-type excitations. The absorption, emission, and Raman spectroscopies are widely used tools for determining molecular structures, may they be in gas or condensed phase.

The diatomics are the simplest molecular systems; a familiar example is the oxygen molecule (O_2) — lifeline of all aerobic organisms. Another example is H_2, which is the key molecule in interstellar chemistry and is the most abundant molecule in the universe [2]. Also, from a theoretical point-of-view, H_2 is interesting as it has only two electrons and two nuclei and is therefore a suitable benchmark for *ab initio* calculations [3]. Diatomics can only vibrate along one coordinate, namely the interatomic distance, and the rotational motion can be considered to be two-dimensional. For their seemingly simple properties, they are often used as prototypes for more complicated systems. The simplicity of diatomics is somewhat misleading: the theoretical considerations are still very involved and the properties are a subject of textbooks [4, 5]. In the gas phase they are by far the most studied systems and thus the electronic, vibrational, and rotational states are usually known to high precision. A great example in this regard is the experimental and theoretical work to determine the electronic potential curves of molecular iodine, I_2 (see for example [6] and references therein). The known properties in the gas phase, the reduced number of nuclear degrees of freedom, and the relatively small size makes the diatomics suitable for condensed phase studies. In this work, the rotation and vibration of some diatomics are considered in rare gas matrices or in homogeneous crystals without restricting to a particular method;

the work is based on experimental projects which were seen to require an additional theoretical consideration.

The spectroscopic properties of diatomics change when embedded in a crystalline environment. The matrix-isolation technique, developed in the 1950's, was meant as a method for studying species which were too unstable for gas phase studies [7–9]. In this technique the principal idea is to isolate the molecules in a "cage" formed by the so-called host species. Rare gases, i.e., noble gases, usually interact weakly with other species and thus are excellent candidates for such hosts. However, it should be noted that rare gases — already anticipated by Pauling [10] — can combine with other elements to form stable molecules [11]. At low temperatures, the rare gas atoms arrange to a face-centered cubic (fcc) lattice [12] with weak van der Waals interactions between particles. The rotational and vibrational motion of any guest molecule introduced in rare gas crystals become hindered. The rotation can even be suppressed altogether, as for example in the cases of iodine and carbon monoxide discussed later. The rare gas solids offer a system which is simple enough for quantitative modelling of solute-solvent interaction and complex enough to exhibit dephasing behavior. As a host, molecular solid of para-hydrogen is an example of a van der Waals solid where the weak interactions between species lead to less hindered molecular motion when compared to rare gas solids; recent article [13] includes a short review to this field of research. The minimally perturbing condensed phase of pure para-hydrogen is dominated by quantum effects and can support long-lived coherences as observed, e.g., in recent pump-probe experiments [14]. The ultimate goal in chemistry can be considered to be the control of chemical reactions; altering the thermodynamical variables such as pressure, temperature, or concentration at the equilibrium, the reaction shift — either toward products or reactants — can be predicted by Le Châtelier's principle. In quantum control, coherent dynamics of molecular wavepacket is exploited using tailored, femtosecond laser pulses to drive the chemical reaction toward desired pathway. As the control is inherently based on interference aspect of quantum mechanics, successful manipulation requires the understanding of dephasing processes [15]. Concerning chemical reactions in condensed phase, many-body interactions pose a challenge in this regard [16,17]. Although the work presented in this thesis does not concern quantum control *per se*, steady-state and time-resolved experimental observations can be related to structural and dynamical properties, whose understanding is crucial for control in condensed phase, with the help of quantum and classical simulations.

The steps in scientific work can be categorized as follows: (1) characterization; (2) hypothesis; (3) prediction; (4) testing the previous steps (1)-(3). The process of acquiring knowledge through these steps is referred as scientific method. The step (1) concerns of making observations or experiments of the phenomena, preferably followed by a hypothesis, which is formally speaking an explanation for the observations or an "educated guess". Theory and hypothesis are not synonyms; theory is something more "complete" which has been exhaustively tested and has been generally accepted

to describe the phenomena. The logical continuation of a hypothesis is the step (3): prediction. This step is sometimes considered to be the highest ranked step or task. The predictions require new experiments and if a disagreement should arise, the underlying hypothesis becomes under suspicion. In a nutshell, this is the essence of step (4).

The case studies with iodine, carbon monoxide, and hydrogen all concern newly found observations or spectral fingerprints and the numerical work concentrates on formulating hypotheses which explain the observed features by relying to quantum mechanics. The predictive part of the work is seen most clearly in the cases of molecular iodine and cyano radical CN in the form of two-dimensional, time- and frequency-domain coherent anti-Stokes Raman scattering (CARS) images. The carbon monoxide embedded in solid argon has been extensively studied by IR absorption spectroscopy but not with Raman spectroscopy. The present experimental and numerical results point to a different physical origin for the observed features than what some recent studies based on IR spectroscopy suggest. Therefore, a revision of the previous hypotheses was made.

The main body of the text is divided into two chapters: 2. Computational considerations and 3. Main results and discussion. Sec. 2.1 introduces the nuclear degrees of freedom of an isolated diatomic which does not interact with surroundings. This corresponds physically to, e.g., molecules in the gas phase, where they are well-separated from each other. The general effects of weakly interacting environment on the molecular properties is considered in Sec. 2.2. The case where the molecule is trapped in a rare gas solid is discussed first, followed by an introduction of homogeneous crystal of para-hydrogen whose peculiar properties have led to naming of the solid as quantum crystal.

The molecular properties in condensed phase can in principal be investigated either in the time-domain or in the frequency-domain. This separation corresponds to an ideal case, where the fields are either much shorter than the period of motion under study or stationary in time, respectively. In frequency space, the dynamic information of the molecular system shows up in the line shapes (widths) and peak positions. In time-domain techniques the same information is encoded in decaying oscillation of the signal. Secs. 2.3-2.5 introduce both approaches through case studies. A Raman and IR spectroscopic study of CO and H_2 in Sec. 2.3 falls in the frequency-domain category. Additionally, the concept of adiabatic rotation is presented and the theoretical framework behind the simulations of Raman and IR spectra are shown. The molecular wavepacket and its properties, such as dephasing, are introduced in Sec. 2.4. Resonance Raman (RR) in the frequency-domain and time-domain techniques CARS and pump-probe optical Kerr effect (OKE) spectroscopies in the femtosecond regime are introduced in Sec. 2.5. All involve a Raman process where the incident photon is either resonant or off-resonant with any electronic state. The relevant macroscopic

variable is the induced polarization, which acts as the source for the radiation field which carries the information of the system. The focus is on the introduction of the methods from a simulational point-of-view.

The principal results are gathered in Chapter 3. Models for rotation of CO and H_2 in solid argon are presented in Sec. 3.1 within a static approach which gives a qualitative explanation for the Raman and IR spectra [I,II]. Then the local structure and dynamics of matrix-isolated iodine in xenon are interpreted from the simulation runs in Sec. 3.2. Trapping site geometries in solid Xe are given as the explanation for the bimodal resonance Raman spectral lines. The RR intensity distributions and the femtosecond time-resolved CARS signal oscillations are then reproduced. A predictive portion of the investigation comprises of the two-dimensional time-frequency images or interferograms [III]. For CN, time- and frequency-resolved CARS spectra for the rotational coherences or dynamics are given in Sec. 3.3. The results presented therein concern future experiments with CARS spectroscopy of matrix-isolated CN in Xe [IV]. The final section 3.4 is devoted for the rotational anisotropy in solid para-hydrogen. The pump-probe OKE signals are reproduced qualitatively using an induced Hamiltonian derived from first principles of matter-light interaction [V].

The key results are summarized in Sec. 4. A more detailed account of the systems can be found in Publications I-V.

2 Computational considerations

2.1 Molecular eigenstates of diatomic molecules

Without any external perturbance, the molecular motion of a diatomic molecule is governed by the center of mass (c.m.) translational motion (kinetic energy), internal degrees of freedom (vibrational, electronic), and external degrees of freedom (rotational). The c.m. motion is bypassed below. Assuming that the nuclei move slowly compared to electrons, the Born-Oppenheimer (BO) approximation is invoked. In this approximation, the electronic and nuclear motions are decoupled and the electronic energy is calculated in fixed nuclear configuration. The breakdown of the BO approximation results in so-called nonadiabatic dynamics but these are not considered in this work. For the current status of theory of nonadiabatic dynamics, see Ref. [18]. Further simplification to the many-body problem can be achieved by invoking the rigid rotor model where the vibrational and rotational degrees of freedom become separated as the interatomic distance is assumed to be fixed during rotation. The total molecular wavefunction can then be written as $\Psi_{\mathrm{mol}} = \psi_{\mathrm{el}}\psi_{\mathrm{vib}}\psi_{\mathrm{rot}}$, which is a solution of the time-dependent Schrödinger equation

$$i\hbar\frac{\partial|\Psi\rangle_{\mathrm{mol}}}{\partial t} = \hat{H}_0|\Psi\rangle_{\mathrm{mol}}\,, \tag{2.1}$$

where the Hamiltonian is a sum

$$\hat{H}_0 = \hat{H}_{\mathrm{el}} + \hat{H}_{\mathrm{vib}} + \hat{H}_{\mathrm{rot}}\,. \tag{2.2}$$

The electronic part of the wavefunction depends on electron positions and parametrically on the internuclear distance whereas the nuclear part $\psi_{\mathrm{vib}}\psi_{\mathrm{rot}}$ is a function of the internuclear distance r only. Physically the above separation means that the nuclei move in an effective potential determined by the electronic energy plus the nuclear repulsion as a function of interatomic distance. The potentials are referred as adiabatic potentials and are used throughout this work. The Morse potential [19]

$$V(r) = V_{\mathrm{min}}[1 - \exp(-a(r - r_e))]^2 \tag{2.3}$$

is widely used to represent the molecular potential energy in the solution of vibrational Hamiltonian. The parameter V_{min} is the well depth, measured from the curve minimum at equilibrium distance r_e up to dissociation limit and therefore relates to the dissociation energy.

Let's now assume that the diatomic vibration takes place in an effective potential described by a Morse potential where the rotation of the molecule is neglected. The vibrational energy levels in Morse potential can be shown to be (see, for example, Ref. [20])

$$E_{\mathrm{vib}} = \hbar\omega_e(\nu + \frac{1}{2}) - \hbar\omega_e x_e(\nu + \frac{1}{2})^2 \,. \tag{2.4}$$

We see that the first term is the energy of harmonic oscillator while the second term is a correction to the potential due to the curvature at high energies. A Morse oscillator has a finite number of bound states, contrary to the harmonic oscillator. The harmonic frequency ω_e and the anharmonic term $\omega_e x_e$ are related to the molecular and potential parameters in a following way:

$$\begin{aligned} \omega_e &= a\left(\frac{2V_{\mathrm{min}}}{\mu}\right)^{\frac{1}{2}} \quad \text{and} \\ x_e &= \left(\frac{\hbar\omega_e}{4V_{\mathrm{min}}}\right) \,, \end{aligned} \tag{2.5}$$

where μ is reduced mass. The vibrational states are solved with the Fourier-Grid-Hamiltonian (FGH) method described in Sec. 2.1.1 with a potential term $V(r)$ which is not necessarily a Morse type.

We now turn to the rotational degree of motion which is the smallest term in the total Hamiltonian [Eq. (2.2)]. The rotation is defined with respect to an external axis frame, termed space-fixed frame $\{X, Y, Z\}$. The parametrization of the rotation is done using the Euler angles $\{\theta, \phi, \chi\}$. For general definition, see for example the book by Zare [21]. For a diatomic molecule, two of the Euler angles θ and ϕ suffices and χ can be chosen freely. Rotation of a molecule parametrized by the polar angle θ and azimuthal angle ϕ is depicted in Fig. 2.1. Only the z-axis, which is parallel to the internuclear (vibrational) coordinate, is shown here. If one chooses $\chi = 0$, the x-axis is perpendicular to the plane of rotation which is the yz-plane. Generally, the molecule axis frame is referred as body-fixed frame $\{x, y, z\}$ and the z-axis points along the symmetry axis.

For a linear molecule with zero electronic orbital (Λ) and spin (Σ) angular momentum, $\Omega = \Lambda = \Sigma = 0$, the rotational wavefunction is given in the representation that diagonalizes the operators $\hat{J}^2$ and $\hat{J}_Z$. In coordinate space the spherical harmonics $Y_{JM}(\theta, \phi)$, which are solutions of the Schrödinger equation for a particle moving on the surface of a sphere, satisfy this condition. The spherical harmonics are a product of two functions, one depending on the polar angle θ and the other on the azimuthal angle ϕ:

$$\begin{aligned} Y_{JM}(\theta, \phi) &= \Theta_{JM}(\theta)\Phi_M(\phi) \\ &= e^{-iM\phi}(-1)^M \left[\frac{2J+1}{2}\frac{(J-M)!}{(J+M)!}\right]^{\frac{1}{2}} P_J^M(\cos\theta) \,, \end{aligned} \tag{2.6}$$

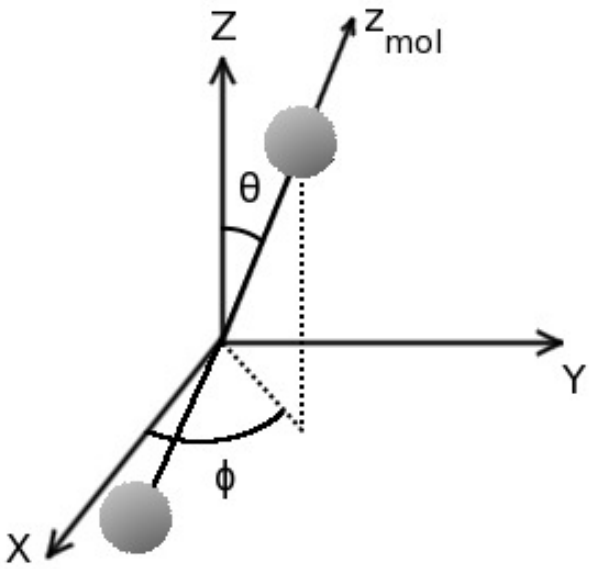

Figure 2.1: Molecular axis orientation for a diatomic in a space-fixed coordinate system $\{X, Y, Z\}$. The two Euler angles θ, ϕ suffice for a general diatomic and the third Euler angle χ is redundant. Usual choice is to put $\chi = 0$ (e.g. Ref. [21]), but other choices could be made, for example $\chi = \pi/2$ [22,23].

where $P_J^M(\cos\theta)$ are the associated Legendre functions. The rotational Hamiltonian of the diatomic is

$$H_{\text{rot}} = \hbar^2 \frac{\hat{J}^2}{2\mu r^2} = B_e \hat{J}^2 \,, \tag{2.7}$$

where μr^2 is the inertia and B_e is the rotational constant. As the spherical harmonics are eigenfunctions of J^2 with eigenvalues $J(J+1)$, the rotational energy is

$$E_{\text{rot}} = B_e J(J+1) \,. \tag{2.8}$$

The above case refers to situation where the molecule rotates, but does not vibrate. Going beyond the rigid rotor model, the molecular bond can stretch due to centrifugal forces which elongates the bond and hence increases the moment of inertia. The first approximation for the rotational energy is

$$E = B_e J(J+1) - D_e[J(J+1)]^2 \,, \tag{2.9}$$

where D_e is the centrifugal constant. Of course, when the rigid rotor model is abandoned, the rotation becomes affected according to which vibrational state the molecule occupies. The rotational constant B_e is a hypothetical value which corresponds to a vibrationless molecule. The rotation and vibration become coupled as the expectation value $\langle\nu|1/r^2|\nu\rangle$ is in general different from the equilibrium value $1/r_e^2$. The rotational constant is therefore dependent on the vibrational state and is described by the

relation (see e.g. Ref. [4])

$$B_\nu = B_e - \alpha_e(\nu + \frac{1}{2}) \,. \tag{2.10}$$

The term α_e is a correction that accounts for the deviation between the expectation value $\langle 1/r^2 \rangle$ and the equilibrium value $1/r_e^2$. Similar expression for the centrifugal constant is

$$D_\nu = D_e + \beta_e(\nu + \frac{1}{2}) \,. \tag{2.11}$$

The above expressions are enough for the present diatomics, except for the CN in solid Xe (Sec. 3.3). In this case, the coupling between electronic and rotational motion must be considered. The coupling schemes are known as the Hund's cases a-d, and CN is considered to belong to the Hund's case b. The I_2 molecule is considered to belong to Hund's case c, but we dot explicitly calculate its rotational states. The other cases, CO, ortho- ($o\mathrm{H}_2$) and para-hydrogen ($p\mathrm{H}_2$), belong to Hund's case a. The electronic ground state is a Σ state and Eq. (2.9) is used in Secs. 3.1 and 3.4. The ground electronic state of CN is a $^2\Sigma$ state meaning that the electronic spin angular momentum is $S = 1/2$ and the orbital electronic angular momentum is $\Lambda = 0$. The coupling between the nuclear angular momentum **N** and the spin angular momentum **S** leads to a splitting of rotational levels into two manifolds:

$$E^+ = B_e N(N+1) + \frac{\gamma}{2} N \qquad J = N + \frac{1}{2} \tag{2.12}$$

$$E^- = B_e N(N+1) - \frac{\gamma}{2}(N+1) \quad J = N - \frac{1}{2} \,. \tag{2.13}$$

The levels with $J = N + \frac{1}{2}$ are called the F_1 branch and the ones with $J = N - \frac{1}{2}$ are called F_2 branch [21]. In the case of rotational CARS with CN, we neglect the spin-rotation coupling γ but retain the quantum number N. The levels N then become double-degenerate which is taken into account in the Boltzmann distribution.

In molecular spectroscopy, transitions between eigenstates are induced by the interaction with light. Concentrating on the electric dipole allowed transitions, the quantity of interest is the transition dipole moment. The gross and specific selection rules are derived by determining when the transition dipole moment is non-zero.

Gross selection rules concern the properties that the molecule, here diatomic, must possess in order to show a transition. Such a rule in IR is that the diatomic must have a permanent electric dipole moment in order to show pure rotational transitions. Also, the vibrational transitions require that the dipole moment varies during elongation or contraction of the bond. Therefore, homonuclear molecules such as I_2 and H_2 are infrared inactive and their properties remain "dark". In Raman spectroscopy, the molecule must possess anisotropic polarizability to exhibit pure rotational transitions, and the polarizability must change during bond stretch in order to show vibrational

transitions. Diatomics fulfill these conditions and their rotational and vibrational transitions are observed in Raman spectroscopy.

Specific transition rules concern the changes in quantum numbers that occur in transitions and are given below for the relevant cases in this work. Some words about nomenclature: rotational transitions between states in the same vibrational state are termed pure rotational transitions; if the vibrational quantum number changes during the rotational transition, it is called rovibrational transition, or rovibronic when the vibrational states are in different electronic states. For a diatomic without electronic orbital angular momentum ($\Lambda = 0$), the rovibrational selection rules are

$$\Delta J = \pm 1 \qquad \text{IR} \tag{2.14}$$

$$= 0, \pm 2 \quad \text{Raman}\,. \tag{2.15}$$

The above rules also concern the pure rotational transitions, except for the $\Delta J = 0$ rule which does not result in observable transition. The vibrational quanta ν can change in general by any integral value due to anharmonic effects, but the most intense Raman and IR lines correspond to $\Delta\nu = \pm 1$. For a harmonic oscillator, this transition rule becomes exact. In a vibronic transition, Franck-Condon approximation is normally used where the momentum and position of the atoms are unchanged in the electronic transition (so-called vertical transition). The transition intensity is then proportional to the squared overlap between the vibrational eigenfunctions in their respective electronic states — generally referred as Franck-Condon factors — and the vibrational quantum number can change by any integer. The selection rules for rovibronic transitions are, however, much more diverse. This arises from the coupling between rotational and electronic motion, i.e., from the dependence on the Hund's coupling case. The case of relevance in this thesis is the electronic transition $^2\Sigma - {}^2\Sigma$ for the CN and the selection rules are [4]

$$\Delta N = \pm 1 \tag{2.16}$$

$$\Delta J = 0, \pm 1\,. \tag{2.17}$$

For the electronic transition between X and B electronic states of matrix-isolated iodine (Sec. 3.2), the rotational transitions are not resolved and thus the rotational manifold is left out from the simulations.

2.1.1 Solving the vibrational states

The chosen numerical method for the evaluation of the vibrational manifold was the Fourier-Grid-Hamiltonian (FGH) [24, 25]. In this method, the Hamiltonian matrix in the position representation

$$\langle x_i|\hat{H}|x_j\rangle = \langle x_i|\hat{T}(\hat{p})|x_j\rangle + \langle x_i|\hat{V}(\hat{x})|x_j\rangle \tag{2.18}$$

is solved in Fourier pseudospectral scheme, where the coordinates are discretized at evenly spaced grid. The calculation of the Hamiltonian then reduces to finding the eigenvectors and eigenvalues of matrix H. The potential energy matrix $V(\hat{x})$ is diagonal in the coordinate space,

$$\langle x_i|\hat{V}(\hat{x})|x_j\rangle = V(x_j)\delta_{ij} \,, \tag{2.19}$$

whereas the kinetic energy operator is diagonal in the momentum space p: $\hat{T} = \hat{p}^2/2\mu$. We now invoke the result for the kinetic energy matrix (see Ref. [26] or [27]):

$$T_{ij} = \frac{\hbar^2}{2m} \begin{cases} \frac{K^2}{3} & i = j \\ \frac{2K^2}{3}\frac{(-1)^{j-i}}{(i-j)^2} & i \neq j \end{cases}$$

where $K = \pi/\Delta x$. Symmetric relation between the spacings in the discretized coordinate (Δx) and k-space (Δk) exists:

$$\Delta k \Delta x = \frac{2\pi}{N} \,, \tag{2.20}$$

where N is the number of grid points in coordinate space. Note that the grid size N and spacing Δx define the grid spacing in the momentum space. The maximum wavelength or minimum frequency is determined by the length $N\Delta x$ of the coordinate space through the relation $\lambda_{\max} = N\Delta x$. We noticed that a grid size of $N = 256$ is enough when the vibrational state space is solved in Morse or Morse-like potentials. The eigenvalues and eigenvectors of the Hamiltonian matrix

$$H_{ij} = T_{ij} + V_{ij}(x)\delta_{ij} \tag{2.21}$$

are then found by diagonalizing the matrix with $i, j = 1, \ldots, 256$.

For the solution of Eq. (2.21), the potential matrix elements V_{ij} must be known. In our case the potential term is the ground or excited adiabatic electronic state of the molecule and the relevant coordinate is the internal vibration coordinate r (bond length). Three different approaches for the calculation of this term appears in this thesis. For the CN radical (Sec. 3.3), gas phase Morse potentials are used. In the case of rotating CO in solid Ar (Sec. 3.1), the fundamental vibrational frequency ($\nu : 1 \leftarrow 0$) is solved by writing the potential term as a sum

$$V(r) = V_{\mathrm{CO}}(r) + \sum_i V_{\mathrm{Ar}_i-\mathrm{CO}}(r, \theta, R) \,, \tag{2.22}$$

where the summation is over sufficient number of nearest argon atoms and r is the bond length. The potential V_{CO} is an empirical gas phase potential for the isolated CO molecule and $V_{\mathrm{Ar}_i-\mathrm{CO}}$ is the three-dimensional pair-potential of Ar-CO complex [28]. As will be described in Sec. 2.3, the rotational adiabatic potentials give the preferred orientation of the molecular axis. By choosing a potential energy minimum

from the 2D angular surface, the corresponding point dictates the variables R and θ in $V_{\mathrm{Ar}_i-\mathrm{CO}}(r,\theta,R)$ as the distance R and angle θ can be calculated from the equilibrium positions of the center of mass of CO and surrounding argon atoms. The results were also compared to *ab initio* calculations with RI-MP2/def2-TZVPP level of theory using Turbomole program package [29].

The third method for the calculation of the potential energy $V(r)$ is the molecular dynamics (MD) approach in I_2-Xe (Sec. 3.2). During the MD simulations, the molecular bond remains practically unchanged and the potential energy curve for the I_2 vibration is obtained after simulation run by manually stretching the bond in otherwise frozen matrix. The simulations are repeated over 500 trajectories, obtaining the ensemble averaged potential curve:

$$V(r) = V_{\mathrm{I}_2}^{X/B}(r) + \underbrace{V_{\text{Xe-Xe}}^{\text{ave}}(R) + V_{\text{I-Xe}}^{\text{ave}}(R,r)}_{V_{\text{bath}}} \,. \tag{2.23}$$

The I-I potential energy curve for the ground X [30] and excited B state [31] is of the standard Morse form. The isotropic part in the I-Xe and the Xe-Xe interaction energies are described by the Tang-Toennies parametrization [32] and the anisotropic part in I-Xe ($|3/2,3/2\rangle$ and $|3/2,1/2\rangle$ states, Ref. [33]) is constructed by the diatomics-in-molecules method [34, 35].

2.2 Solid state effects on molecular states

The nuclear degrees of freedom in a pure solid, such as solid para-hydrogen, or when the rare gas matrix is doped with guest (diatomic) molecule are briefly discussed here. The interaction which induces deviations from the isolated level structure is termed crystal-field effect. The molecular Hamiltonian becomes

$$H_{\mathrm{mol}} = H_0 + H_{\mathrm{cry}} \,, \tag{2.24}$$

where H_0 is the unperturbed molecular Hamiltonian and H_{cry} is the crystal-field Hamiltonian which includes all the intermolecular interactions between the diatomic and the environment. The formal solution of the crystal field term is done in the free rotor basis, assuming further that the quantum numbers of the isolated molecule are still "good". Furthermore, usually the transition rules still pertain to the isolated case. First, we consider the degrees of freedom when the molecule is embedded in solid rare gas (RG). Then the rotation in pure para-hydrogen is discussed and the concept of quantum crystal is introduced.

2.2.1 Diatomic impurities in rare gas matrices

In matrix-isolation spectroscopy (MIS), a mixture of so-called host and guest gases is condensed on a cold substrate; this process is called deposition and the crystalline host structure referred to as matrix. The principal idea is to study photophysical or dynamical properties of isolated molecules in a weakly interacting medium — this requirement is satisfied in the rare gas solids (RGSs) Ne, Ar, Kr, Xe due to weak van der Waals forces. The MIS technique is well described in Ref. [7].

When the gas mixture solidifies, the guest replaces the lattice site(s) of host atoms, i.e., substitution of host atom(s) with guest molecule(s) takes place. The number of substituted atoms depends on the size of the molecule and the rare gas. For example, iodine usually takes double-substitution (DS) site in rare gas matrices, i.e., replacing two RG atoms from their perfect lattice sites [36–39]. The guest molecule can also aggregate which depends on the balance between guest-guest and host-guest interactions. The atoms effectively form a cage around the molecule which has a profound impact on the molecular properties, often referred as the cage effect. In this thesis, the term cage effect is used to describe the effect of the surrounding cage on the photodissociation event and on the molecular energy levels.

In general, three cases for the rotational motion arise when a molecule is isolated in atomic rare gas solids: (1) librational motion, where the molecular axis oscillates about some equilibrium orientation; (2) the intermediate case termed hindered rotation, which is best described as a rotational tunneling; (3) the nearly-free rotation. All these cases arise in this work. In the case (1), the rotational level structure resembles that of a harmonic oscillator when bound states are considered; the rotational states are superpositions of $|JM\rangle$ states. Libration occurs when the interaction energy has a large anisotropic part, for example when the molecule resides in a double-substitution site. The rotational potential well is deep, resulting in a large zero-point energy (ZPE) with respect to rotation. In the hindered rotation case (2), energy levels shift from the gas phase and split into different $J = 0, 1, 2, \ldots$ manifolds that are further split into M-substates. In the third case, the intermolecular forces are weak and the level structure closely resembles that of an isolated (gas phase) molecule. As the rotational barriers are not too high in this case, the ZPE of the motion is close to isotropic limit (zero), and a less pronounced splitting of rotational manifolds is observed. Overall, the actual level structure depends on the interplay between molecular properties (rotational constant), local geometry in the solid (symmetry), and the anisotropic interaction strength. Furthermore, the energy level shift is due to the isotropic interaction whereas the splitting results from the anisotropic part. There is another effect which is not included in above discussion: the reduction of rotational constant B_ν (also the centrifugal constant may change) from the gas phase. As will be mentioned in Sec. 2.3, rotation about the interaction center (rotation-translation coupling) and the additional inertia of synchronous movement of lattice atoms cause an increase in

moment of inertia which lowers the rotational constant. This can be seen to counteract the static effects of the crystal field, namely by reducing the energy spacing.

Coupling between the internal, i.e., vibrational and electronic, and the bath (surroundings) degrees of freedom generally induces a shift in the energy levels; term matrix-induced shift is used. Usually, the electronic states are red-shifted with respect to the gas phase and the Onsager model [40] is often applied to estimate the inductive shift in electronic energy. The magnitude of the shift depends on the nature of the electronic potential and the polarizability of the matrix. Generally, larger red-shifts are observed for the ionic states than the valence states due to increased dipole moment in the ion-pair states. However, the Rydberg states are blue-shifted in RGSs since the extended electron cloud is strongly repelled by the filled electron shells of the rare gas atoms. A collection of electronic shifts in different rare gas matrices can be found in Ref. [41].

Similarly, the vibrational states on a certain electronic levels are shifted due to the intermolecular forces. The relative shifts from the gas phase depend on the relative contributions from dispersion, induction, and repulsion forces [42]. Another shift induced by the cage effect is the so called "geometrical shift", where the molecular atoms collide with the surrounding cage. The potential curve for the diatomic then becomes "bent" above the dissociation limit. For iodine, the ground state X harmonic frequency and electronic origin of the $B \leftarrow X$ show increased red-shifts when going from Ar to Kr, and further to the most polarizable matrix studied, Xe [43, 44].

2.2.2 Pure quantum crystals of para-hydrogen

Atomic crystals formed by Ar, Kr, and Xe are sometimes referred as classical solids. The nomenclature refers to the fact that due to large mass and deep interatomic potential well, the atoms are highly localized in the lattice (small zero-point motion of translation). In solid hydrogen, however, this is not the case. Due to light mass and weak intermolecular forces, a quantum diffusion takes place; the molecule can change positions in the lattice. The properties of pure solid hydrogen are explained in more detail in the book by Manzhelii and Freiman [3].

Due to the Pauli exclusion principle, hydrogen molecules exist in two forms which are called para- ($p\mathrm{H_2}$) and ortho-hydrogen ($o\mathrm{H_2}$). These are spin isomers, ortho-hydrogen has a total nuclear spin $I = 1$ and para-hydrogen has $I = 0$. The spin wavefunction of ortho-hydrogen is symmetric, whereas for para-hydrogen the spin part is antisymmetric. As the vibrational wavefunction does not change sign in permutation of the nuclei, nor does the electronic wavefunction due to the ${}^1\Sigma_g^+$ ground state, the rotational wavefunction must be either symmetric (J even) or antisymmetric (J odd). Thus para-hydrogen only has $J = 0, 2, 4 \ldots$ rotational states.

In solid para-hydrogen, all the molecules are in the ground state $J = 0$ which corresponds to the spherically symmetric wavefunction $Y_{00}(\theta, \phi)$. The small moment of inertia, i.e., large rotational constant, effectively renders the thermal excitation to $J = 2$ impossible. With external perturbance such as laser pulse, the molecule can be excited to the $J = 2$ state. As the molecular hydrogen does not have any permanent dipole moment, the first nonzero electric multipole moment is the quadrupole moment. When the molecule is in the (nonspherical) $J = 2$ state, quadrupole-quadrupole interaction between molecules arises. This leads to the splitting of $J = 2$ to three substates $|M| = 0, 1, 2$. The quantum nature of the rotational motion now exhibits itself; the rotationally excited $J = 2$ states correspond to Bloch-waves traveling in the crystal. As they propagate, the excitation hops from molecule to molecule, effectively transferring angular momentum in the process. This is referred to as collective excitation, or roton in the case of rotational excitation. Kranendonk considered theoretically the excitations in solid para-hydrogen and derived the crystal-field splitting of $J = 2$ state to $|M| = 1, 2, 0$ substates [45–48]:

$$H_{\text{cry}} = 0.903 \frac{Q_0^2}{5R_e^5} \begin{cases} -4, & |M| = 1 \\ 1, & |M| = 2 \\ 6, & M = 0 \end{cases}, \tag{2.25}$$

where Q_0 is the matrix element of quadrupole moment in the ground vibrational state and R_e is the nearest-neighbor distance (lattice constant). Since Kranendonk, the roton dynamics has been investigated by several authors [49–53]. Very recently Königsmann *et al.* [14, 54] used optical Kerr effect (OKE) spectroscopy to detect roton dynamics. In Sec. 2.5.3, OKE method is discussed from a molecular alignment point-of-view. Similarly, the internal vibration can be excited collectively and the traveling wave is called vibron, separate from the collective vibration between molecules; phonons. In ortho-hydrogen, also the excitation of the molecular orientation M with respect to the crystal axis can become delocalized; these are called librons [55, 56].

2.3 Photodissociation products of H_2CO in Ar

Phototodissociation of molecules in RGS offers a great opportunity to study the effect of solvent cage on the dynamics of photochemical reactions. The fragments can undergo a cage exit, geminate recombination, or even form a new compound with the host matrix; first argon compound HArF was recognized after photolyzation of HF in crystalline argon [57]. In Publication II, experimental Raman spectra of CO and H_2 were measured after laser-induced dissociation of formaldehyde. This section is devoted to the end-products of the reaction.

The photodissociation of formaldehyde has been thoroughly investigated both experimentally and theoretically; the latter concentrating in the gas phase, see Refs. [58–61]

and references therein. Two primary photodissociation channels can be recognized:

$$H_2CO + h\nu \rightarrow H_2 + CO \quad (1)$$

$$H_2CO + h\nu \rightarrow H + HCO \quad (2)$$

The channel (1) produces molecular products; hence it is referred to as the molecular channel. Channel (2) is called the radical channel as the end products are open shell atoms/molecules (radicals). We speculate in Publication II that the cage effectively blocks the (2) even though the gas phase studies suggest that the radical channel is the dominant pathway at the used laser energy. In previous accounts in the condensed phase, namely in RGS, the main photoproduct of interest has been the molecular CO, identified by infrared spectroscopy [62–66]. As an end-product of the H_2CO dissociation, H_2 has been observed in the gas phase by Raman spectroscopy [67, 68] but not in rare gas matrices. The atomic H as a radical channel product has been investigated previously by electron paramagnetic resonance (EPR) [66] and ultraviolet-visible (UV-Vis) [69] spectroscopies. Vaskonen and Kunttu identified also the HCO radical through EPR [66]. The first measured Raman spectra of the photoproducts CO and H_2 in RGSs, presented in Publication II, give new information on photochemistry of formaldehyde in the condensed phase. In our laboratory, Raman spectroscopy has been used before to study the laser-induced dissociation of formic acid and its dimer in solid argon [70, 71].

The CO molecule has received a lot of attention in the matrix-isolation community. As a dopant, it has been isolated in solid pH_2 [13,54,72,73], solid rare gas matrices [74–88], and in many other solid environments (see Ref. [13] and references therein). The earliest study dates back to 1961, when Maki measured the IR absorption spectrum of solid CO and when embedded in crystalline Ar, N_2, and CH_4 [74]. Since then, numerous experimental [75–82, 84–89] and theoretical [84, 86, 89, 90] investigations of the fundamental absorption frequency have been performed. The assignment of the bands have varied during the decades. Manz developed the concept of pseudorotating lattice which is described below and implemented it on the CO/Ar case. His results suggested transitions between crystal-field split states as the reason behind observed features. The experimental work by Abe *et al.* [85] gave the first clear indication that CO actually rotates in sites of two kinds. The essential difference is that one site allows rotation whereas the other is more confining, resulting in librational motion. Anderson and Winn approached the problem using line shape theory by considering the so-called "cluster" and "crystal" configurations. They explained the spectra as a sum of components originating from CO residing in a double-substitution site in both configurations. Other explanations include CO-N_2 complex [78], CO dimer [65, 84] or CO polymers [76, 77, 83, 89]. Our starting point was the experimental work by Abe *et al.* [85, 87, 88] where spectral features were assigned to monomeric CO, a CO-CO dimer and a CO-H_2O complex.

Previous studies on matrix-isolated normal hydrogen in rare gas matrices [91–98]

all point to the fact that molecular hydrogen rotates almost freely in RGSs. The rotational ($S_0(0)$, $S_0(1)$) Raman spectrum consists of a single band for para- and ortho-hydrogen — absolute shifts from the gas phase depending on the experimental conditions (e.g. matrix, temperature, resolution). The first vibrational transition ($Q_1(0)$, $Q_1(1)$) frequency region exhibits a (vibrational) doublet separated by 6 cm^{-1} due to different B_ν in the upper $\nu = 1$ and lower $\nu = 0$ states. Aggregation and introduction of an additional impurity in Ar resulted in a split structure in the rotational and vibrational transition regions [94]. Matrix-isolation studies on H_2 in solid carbon monoxide [98] and in other molecular solids N_2 and O_2 [91, 92, 94, 98] showed also a more complex band structure for the rotational transitions $S_0(0)$ and $S_0(1)$.

Turning to the present account, the experimental Raman signatures in the region of the fundamental transition frequency $\nu : 1 \leftarrow 0$ of CO and in the region of the rotational transitions $J : 2 \leftarrow 0$ ($p\mathrm{H}_2$) and $J : 3 \leftarrow 1$ ($o\mathrm{H}_2$) showed a triplet split structure in all cases [II]. In order to explain the observed features, additional Raman and IR measurements were performed on the isolated CO in solid Ar [I]. The infrared spectrum was in accord with recent IR studies of CO in solid Ar [85–88]. The broadening of the center band after raising the temperature in the IR spectra was not observed in the Raman spectra. Therefore, it was necessary to study CO-Ar system more closely as the previous assignments for the bands were done on the basis of IR spectra alone. In addition to the CO case, the Raman spectra raised questions of the rotational level structure of H_2 in solid argon and the possibility of a nearest-neighbor CO-H_2 complex as the reason behind the spectral fingerprints. Therefore, the rotational degrees of freedom of CO and H_2 in an argon cage called for theoretical investigation. The outline of the simulation methods for the rotation of both photofragments is given below.

The first theoretical treatment pertaining to the rotation of diatomics in crystals was given by Pauling [99]. Devonshire approached the same problem by considering the rotation of a diatomic in a field of octahedral (O_h) symmetry; this corresponds, for example, to rotation of a diatomic in a single-substitution site in fcc lattice [100]. This model, termed crystal-field theory (CFT), has since been generalized for molecules rotating in any symmetry [101]. In the simplest form of CFT, the center of mass of the rotor at the trapping site and the surrounding cage atoms are fixed; the atom/molecule positions corresponding to a perfect lattice symmetry. The crystal-field Hamiltonian H_{cry} is in this case written as a combination of spherical harmonics with parameters related to the crystal-field strength. The rotational states are presented in a basis set which consists of the elements in the O_h symmetry group.

The CFT with above approximations corresponds to a static model for the rotational motion. Lifting the restriction of fixed center of mass leads to rotational-translational coupling (RTC) models, where the molecule rotates about the so-called "center of interaction" (c.i.), which coincides with the initial single-substitution trapping site.

Furthermore, the rigid lattice assumption can be lifted, which leads to the coupling between the rotation and the motion of host atoms. We take the latter viewpoint, i.e., relax the surrounding lattice and allow the molecular c.m. to move and use the pseudorotating cage model developed by Manz [90]. In this method, the motion of the rare gas atoms is assumed to be faster than the reorientation of the molecular axis; the relaxation toward the equilibrium positions is done at a fixed orientation. This can be considered as a dynamical model and is referred to as adiabatic rotation due to the different time-scales in rotation, translation, and vibrations of the host atoms. The pseudorotating cage introduces additional moment of inertia due to rotation about the c.i. and hindrance by the cage motion; these lead to a lowering of the rotational constant. It is worth noting that the model assumes the molecule takes a single-substitution site and cannot be used when the molecule replaces two or more rare gas atoms.

The intermolecular forces (potential) define the interaction strength between the host and the guest molecule, and subsequently dictate whether the rotating molecule exhibits libration, nearly free rotation, or some intermediate of these two. The usual approach is to represent the potential as a sum over pair-wise potentials between the molecule and the host. Considering the system of CO-H_2 trapped in solid Ar, the full interaction potential for V_{CO} is

$$V_{\mathrm{CO}}^{(\mathrm{sph})} = \sum_{i<j} V_{\mathrm{Ar_i,Ar_j}} + \sum_i V_{\mathrm{Ar_i,CO}}(r_{\mathrm{CO}}, \tilde{R}, \tilde{\Theta}) + \sum_i V_{\mathrm{Ar_i,H_2}}^{(\mathrm{sph})}(R) + V_{\mathrm{H_2-CO}}^{(\mathrm{sph})}(R_{\mathrm{mol}}, \Theta_2)\,. \tag{2.26}$$

When the molecular CO is rotated, we assume that it "feels" only a spherically symmetric hydrogen species. This is done by taking the isotropic part of the interaction potentials in which hydrogen is the other constituent; hence the subscript (sph). The Ar-Ar potential is of Tang-Toennies type [32] where the distance between atoms is the sole parameter. The potential between CO and argon is from Pedersen *et al.* [28] which is a three-dimensional surface. The parameters are the bond length r_{CO}, distance $\tilde{R}$ between molecular c.m. and argon, and angle $\tilde{\Theta}$ which describes the orientation of the molecular axis with respect to the distance vector $\tilde{R}$. The isotropic surface Ar-H_2 [102] above has only the distance R between argon and isotropic hydrogen as parameter. The isotropic CO-H_2 intermolecular potential [103] has the same parameter space as the CO-Ar intermolecular potential energy except for the bond length dependence. In the case of H_2, the Ar-H_2 and CO-H_2 potentials have to be considered in their total

dimensionality:

$$V_{\mathrm{H_2}} = \sum_{i<j} V_{\mathrm{Ar_i,Ar_j}} + \sum_i V_{\mathrm{Ar_i,CO}}(r_{\mathrm{CO}}, \tilde{R}, \tilde{\Theta}) + \sum_i V_{\mathrm{Ar_i,H_2}}(r_{\mathrm{H_2}}, R, \Theta) + V_{\mathrm{H_2-CO}}(R_{\mathrm{mol}}, \Theta_1, \Theta_2, \Phi)\,. \tag{2.27}$$

The 3D Ar-H_2 potential surface [102] has similar parameter dependence as the CO-Ar potential. The intermolecular potential energy surface for the CO-H_2 is, in its full form, a four-dimensional surface. Variables are the intermolecular distance R_{mol} (c.m. to c.m.), relative angles Θ_1 and Θ_2 of molecular axes H_2 and CO, respectively, with respect to the distance vector, and the dihedral (torsion) angle Φ [103].

The guest molecule is placed in a single-substitution (CO and H_2), interstitial (H_2) or double-substitution (CO) site in a fcc simulation cube with 256 argon atoms. In addition to the guest molecule(s), the nearest-neighbor atoms are allowed to relax to their equilibrium positions. In the case of isolated CO and H_2 molecules, two coordination shells around the impurity were relaxed. For the intermolecular complex, we considered four sites for the hydrogen molecule with CO at the origin. In this case, nearest argon atoms to both molecules were relaxed. The equilibrium positions were obtained by finding the minimum potential energy with the pair-wise potentials using gradient descent. For the hydrogen, a single relaxation was done using the isotropic potentials. In the gradient descent method, the forces acting on the particles is calculated and a step is accepted if the potential energy decreases. The molecular orientation of the molecule is relative to the crystal frame, which coincides with the space-fixed frame in Fig. 2.1. The orientational space $\{\theta, \phi\}$ is then mapped to obtain the adiabatic three-dimensional rotational potential surfaces, calculating the total energy at every orientation using the pair-potentials.

The Hamiltonian for the system is of the form shown in Eq. (2.24), with potential $V(\theta, \phi)$:

$$H_{\mathrm{mol}} = H_0 + V(\theta, \phi) = B_{\mathrm{eff}}\hat{J}^2 - D_{\mathrm{eff}}\hat{J}^4 + V(\theta, \phi)\,. \tag{2.28}$$

The small centrifugal constant of CO ($6.1\times10^{-6}\mathrm{cm}^{-1}$ [104]) is neglected. For hydrogen, the centrifugal term is taken into account, as $D_0 = 0.0456$ cm^{-1} [105]. In the case of isolated CO in single-substitution site, the pseudorotating model gives an estimate of 1.24 cm^{-1} for the effective rotational constant B_{eff}. For the double-substitution site we used the gas phase value $B_{\mathrm{eff}} = B_0 = 1.92$ cm^{-1}. The parameters for H_2 are scaled to reproduce the experimental Raman frequencies. The Hamiltonian matrix H

is constructed in the (real-form) spherical harmonics $Y_{JM}(\theta,\phi)$ basis:

$$H_{JM,J'M'} = \left[B_{\text{eff}}J(J+1) - D_{\text{eff}}\left(J(J+1)\right)^2\right]\delta_{JJ'}\delta_{MM'} + \int \mathrm{d}\Omega\, Y^*_{JM}(\theta,\phi)V(\theta,\phi)Y_{J'M'}(\theta,\phi)\,. \tag{2.29}$$

Another, symmetry-adapted (SASH) basis can be used, as was done, e.g., in a study of ClF rotation in Ar [106]. The symmetry elements of O_h point group are special combinations of $Y_{JM}(\theta,\phi)$ [107] and the corresponding SASH basis was used for comparison purposes [I,II].

The intensity for the Raman transition from initial rotational state i to a final state f is the absolute square of the transition matrix averaged over crystal orientations with respect to the laboratory-frame [I]:

$$I_{i\to f} = \frac{16\pi\Delta\alpha^2\epsilon^4}{15^2}\sum_{M=-2}^{2}|\langle\,\Psi_i^{\text{rot}}|Y_{2M}(\theta,\phi)|\,\Psi_f^{\text{rot}}\rangle|^2\,, \tag{2.30}$$

where ϵ is the electric field amplitude and $\Delta\alpha = \alpha_\parallel - \alpha_\perp$ is the polarizability anisotropy. For the IR transition we get a similar expression:

$$I_{i\to f} = \frac{\mu^2_{\nu',\nu}\epsilon^2}{5}\sum_{M=-1}^{1}|\langle\,\Psi_i^{\text{rot}}|Y_{1M}(\theta,\phi)|\,\Psi_f^{\text{rot}}\rangle|^2\,, \tag{2.31}$$

where $\mu_{\nu',\nu} = \langle\nu|\hat{\mu}|\nu\rangle$ is the transition dipole moment between vibrational states ν and ν'. The calculation of the prefactors in Eqs. (2.30) and (2.31) is omitted and they are set to unity. The polarizability and dipole moment are expected to be of comparable magnitude in the trapping sites considered. For CO, quantum chemical IR and Raman intensities were somewhat larger in the SS case [I].

The rovibrational Raman and IR transitions of CO are obtained by adding the vibrational transition energy $\nu : 1 \leftarrow 0$ to the rotational energy manifold. The band origin is calculated by the FGH method (Sec. 2.1.1).

2.4 Molecular wavepacket dynamics on adiabatic potentials

A wavefunction $\Psi_n(x,t) = \psi_n(x)e^{-iE_nt/\hbar}$ which is a solution of TDSE [Eq. (2.1)] with eigenenergy E_n leads to nondynamical observables as the probability density $|\Psi_n(x,t)|^2$ is time-independent. However, the general solution of TDSE is a superposition of eigenstates:

$$\Psi_{\text{tot}}(x,t) = \sum_{n=1}^{\infty} a_n(t)\psi_n(x)e^{-iE_nt/\hbar}\,. \tag{2.32}$$

In a two-state model, e.g., with electronic states g (ground) and e (excited), the probability density shows time-dependence through the cross term, or interference term $\exp\left[-i(E_e - E_g)t/\hbar\right]$. The concept of coherence in the case of wavepackets refers to the interference of waves, namely to what extent the oscillatory interference term retains its phase. If the temporal phase relation between waves is constant in time, the wavepacket is said to be coherent (in time). This is also related to excitation of a wavepacket; in molecular systems, if the time-dependent perturbation has a shorter duration than the characteristic period of motion under study, the excitation is coherent. This means the components of the molecular wavepacket are initially in phase.

If the wavepacket propagates on a harmonic potential, the dynamics of the quantum system can be described in classical terms; the expectation values for the center and the momentum of the wavepacket follow classical mechanics (Ehrenfest theorem). The quantum system is characterized by the classical period $T_{\mathrm{cl}} = 2\pi/\omega$, where ω is the classical frequency of harmonic oscillator. In an anharmonic potential, such as Morse potential, the expectation values do not follow exactly the classical trajectories. Now the spatial part shows dispersion: as the packet propagates in space, the individual components move with different phase velocities and the packet loses its localization in coordinate and momentum space. This does not refer to a loss of coherence as the components still have a fixed phase relation in time (coherence survives). The relocalization of the packet in coordinate and momentum space does not occur anymore at the multiples of T_{cl} only. Instead, the wavepacket now shows revivals at longer times than the classical period, characterized by the revival time T_{rev} [108].

The situation above describes the motion of a wavepacket that evolves in a potential defined by the Hamiltonian H_0 or H_{mol}. In spectroscopy, the properties of matter (molecules) are studied by shining light, either pulsed or with stationary amplitude in time, on the sample. A coherent and spectrally broad laser pulse in the femtosecond regime excites a superposition of eigenstates on the other state, weights depending on the overlap with the initial state, thus forming a coherent wavepacket. For a review on wavepacket dynamics in the femtosecond time-scale, see for example Ref. [109].

2.4.1 Creation and propagation of wavepackets

We consider the excitation of molecules by an oscillating classical electric field. The interaction between the laser field and the molecule is defined in the dipole approximation:

$$\hat{H}_{\mathrm{ind}} = -\hat{\mu} \cdot \vec{E}\,. \tag{2.33}$$

Generally, the electric field is written as

$$E(t) = \hat{\epsilon}\epsilon_m f(t-\tau)\left[e^{-i\omega(t-\tau)}e^{i\mathbf{k}\cdot\mathbf{x}}\right] + \mathrm{c.c.} \tag{2.34}$$

The pulsed field E is centered around τ in time and oscillates with amplitude ϵ_m at carrier frequency ω. The wave propagates in the $\mathbf{k}$ direction with a polarization $\hat{\epsilon}$ which can be linear, circular or elliptic. In all the cases considered, the field is linearly polarized. With lasers in the continuous wave mode (Sec. 2.5.1), the envelope $f(t-\tau)$ becomes time-independent (constant). With pulsed laser fields the envelope is a Gaussian $\exp\left[-2\ln(2)(t-\tau)^2/\tau_{\text{pulse}}^2\right]$, where τ_{pulse} is the full-width at half maximum (FWHM) of the field intensity (Secs. 2.5.2 and 2.5.3).

If the fields can be considered weak, as in Secs. 2.5.1 and 2.5.2, dynamics are solved in the framework of time-dependent perturbation theory [27]. In the wavepacket representation, the Schrödinger equation

$$i\hbar\frac{\partial|\Psi(t)\rangle}{\partial t} = \left[\hat{H}_{\text{mol}} + \hat{H}_{\text{ind}}(t)\right]|\Psi(t)\rangle \tag{2.35}$$

is solved by expanding the molecular state as a series

$$|\Psi(t)\rangle = |\psi^{(0)}(t)\rangle + |\psi^{(1)}(t)\rangle + |\psi^{(2)}(t)\rangle + |\psi^{(3)}(t)\rangle + \dots \tag{2.36}$$

The different order wavepackets $|\psi^{(n)}\rangle$ are given by the perturbative expression

$$|\psi^{(n)}(t)\rangle = (i\hbar)^{-1}\int_{-\infty}^{t} dt' e^{-i\hat{H}_{\text{mol}}(t-t')/\hbar}\hat{H}_{\text{ind}}(t')|\psi^{(n-1)}(t')\rangle\,, \tag{2.37}$$

where the explicit dependence on the wavevector $\mathbf{k}$ has been suppressed. The $\hat{H}_{\text{mol}}$ and $\hat{H}_{\text{ind}}$ above are the Hamiltonians for the molecular system in ground and excited electronic states [Eq. (2.24)] and the time-dependent perturbation [Eq. (2.33)], respectively.

Numerically, the nth order wavepacket is propagated in time using the iterative scheme:

$$\begin{aligned}|\psi^{(n)}(t+\Delta t)\rangle &= e^{-i\hat{H}_{\text{mol}}\Delta t/\hbar}|\psi^{(n)}(t)\rangle \\ &\quad - \frac{i}{\hbar}\Delta t\hat{H}_{\text{ind}}|\psi^{(n-1)}(t+\Delta t)\rangle\,,\end{aligned} \tag{2.38}$$

where $\hat{H}_{\text{ind}} = \hat{\mu}E(t+\Delta t)$ and Δt is the time step. The time-propagator $\exp[-i\hat{H}_{\text{mol}}\Delta t/\hbar]$ is approximated using the split-operator method [110], where the operator is a product of kinetic and potential energy operators (given in Sec. 2.1.1):

$$e^{-i\hat{H}_{\text{mol}}\Delta t/\hbar} = e^{-i\hat{T}\Delta t/\hbar}e^{-iV(\hat{r})\Delta t/\hbar}\,. \tag{2.39}$$

When the operator acts on a wavepacket ψ, the $\exp\left[-iV(\hat{r})\Delta t/\hbar\right]\psi$ is just a multiplier. For the kinetic energy part, the wavepacket is first Fourier transformed to momentum space and then multiplied by the operator. The result is then transformed back to

coordinate space: $\mathcal{F}^{-1}\left\{e^{-i\hat{T}\Delta t/\hbar}\mathcal{F}\left\{e^{-iV(\hat{r})\Delta t/\hbar}\psi(\hat{r})\right\}\right\}$. The spatial amplitude of the wavepacket is evolved in $N = 256$ grid points with spacing $\Delta r = r_{\text{range}}/(N-1)$ where r_{range} was a suitable range of internuclear coordinates. Owing to the properties of the r and p transform pair (see Sec. 2.1.1), the range in k-space is simply $2\pi/(N\Delta r)$. The initial state $|\psi_i^{(0)}\rangle$ in the iteration is generally a single rovibrational state in the ground electronic state and acquires only a phase term $\exp[-iE_it/\hbar]$ during propagation.

2.4.2 Dephasing

Above we considered a quantum system (molecule) prepared in a single quantum state $|\psi_i\rangle$. The system is then said to be in a pure state. In reality, there is a probability distribution associated with the state in which the molecule resides. It turns out that the molecule cannot be assigned a single wavefunction. The system is then in a mixed state, often referred to as ensemble average or statistical average. The general density operator $\rho = \sum_k p_k|\psi_k\rangle\langle\psi_k|$, where p_k is the probability to be in the quantum state k, offers the formal definition of a mixed state. The definition of a pure state follows when the probability p_i for a state i is exactly one; the rest of the terms are zero. The equation of motion for the density matrix is given by the Liouville-von Neumann equation [111]:

$$\frac{\partial\rho(t)}{\partial t} = -\frac{i}{\hbar}\left[\hat{H}, \rho(t)\right] . \tag{2.40}$$

It is clear that if the density matrix (corresponding to pure or mixed state) commutes with the Hamiltonian, ρ is a constant of motion. An important example is the equilibrium canonical density operator $\rho = e^{-\beta\hat{H}_{\text{mol}}}/Q$, where $\beta = 1/k_bT$ (k_b is the Boltzmann constant and T is temperature) and Q is the canonical partition function. Being a function of an operator $\hat{H}_{\text{mol}}$, the matrix is diagonal in the energy representation. Turning again to a pure state, restricted to the two-level $\{g, e\}$ case, the density matrix can be written as

$$\rho(t) = \begin{pmatrix} |c_g|^2 & c_gc_e^*e^{-i(E_g-E_e)t/\hbar} \\ c_g^*c_ee^{i(E_g-E_e)t/\hbar} & |c_e|^2 \end{pmatrix} \tag{2.41}$$

where the diagonal elements are in general called populations and the off-diagonal terms coherences. The time-dependence is again due to the interference term. The density matrix which represents a mixed state can be thought as a superposition of pure state density matrices. Considering a single pure state as the one in Eq. (2.41), we see that the coherence terms should decay to zero and the population distribution relax to Boltzmann distribution in order to reach equilibrium. The latter process is inelastic by nature; terms energy relaxation, dissipation, and population decay are used synonymously. The characteristic time-scale for the process is termed T_1. The loss (decay) of coherence is often called decoherence or dephasing and the phase correlation can be lost due to inelastic (population decay) and/or elastic (pure dephasing)

processes. The time constant for the dephasing is termed T_2. The pure dephasing, with time scale called T_2^*, refers to loss of coherence without dissipation. Formally, the dephasing can be introduced through an additional term in the equation of motion

$$\frac{\partial \rho(t)}{\partial t} = -\frac{i}{\hbar}\left[\hat{H}_{\mathrm{mol}} + \hat{H}_{\mathrm{ind}}, \rho(t)\right] + \left(\frac{\partial \rho(t)}{\partial t}\right)_{\mathrm{dph}}, \tag{2.42}$$

where the second term accounts for the dephasing [112].

In this work, the coherence between rovibrational states in different electronic states is studied through numerical simulations of resonance Raman and time-frequency resolved coherent anti-Stokes Raman scattering spectroscopies. First, the coherences between vibrational states in different electronic levels are called electronic coherences; the loss of coherence is termed electronic dephasing. In this case the states in the density matrix (2.41) are vibrational states in different electronic levels e and g. Similarly, terms vibrational coherence and dephasing are used when considering vibrational states of the same electronic state.

A semi-classical model of the vibrational (pure) dephasing is presented pictorially in Fig. 2.2 (a). The underlying process is stochastic by nature and described by Kubo's stochastic theory [113] where the system (molecule) is treated quantum-mechanically and the solvent classically. The potential shape becomes deformed by the solvent-molecule interaction and the energy difference becomes time-dependent; fluctuation depending on the solvent configuration. In this semi-classical model, a single molecule does not exhibit decoherence; the oscillation period changes with time but the interference (off-diagonal) term in the density matrix maintains its amplitude. However, experiments usually probe the ensemble average which is an incoherent sum over individual components. In this case the oscillation pattern will decay in time. Therefore, in the case of pure dephasing, the physical origin is the statistical fluctuation in the local environment for different members of the ensemble [114].

Turning to the electronic dephasing depicted in Fig. 2.2, the solvent-molecule interaction may induce a shift in the electronic origin ΔE and/or in the equilibrium distance ΔR contrary to the vibrational case where the solvent changes the shape of the potential curve. Physical reason behind the loss of coherence is again due to the fluctuations in the local environment, but now the off-diagonal term has the coherence between vibrational states in different electronic levels. Note that shift in energy or equilibrium distance does not lead to vibrational dephasing, as the relative vibrational energies do not change with time, and the vibrational dephasing contributes to the electronic dephasing. The Brownian oscillator model for the microscopic theory of dephasing, where both the molecule and the solvent are treated quantum mechanically, is widely used [111].

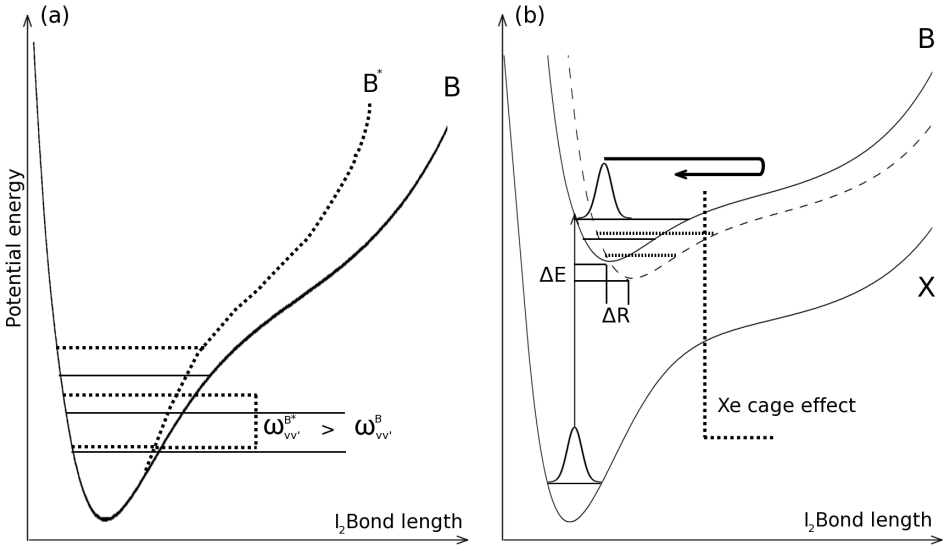

Figure 2.2: A schematic representation of the physical origin for (a) vibrational and (b) electronic dephasing. Potential curves X and B of I_2 in Xe from MD runs are used to illustrate the mechanism. The potentials are bent above the dissociation limit where the I-atoms collide with the Xe-cage atoms. (a) The effective (MD) potential (solid) is changed due to tightening (dot) cage. This relates to shifting of the vibrational levels to higher in energy, shown for hypothetical energy spacing $\omega_{\nu\nu'}$. (b) The electronic coherence, created by e.g. resonant laser field, depends on the relative position of the effective B and X electronic states. The electronic gap ΔE and/or equilibrium distance ΔR are influenced by the cage in a random (stochastical) way which eventually destroys the coherence. Additionally, the vibrational dephasing in (a) leads to electronic decoherence as the potential shape gets deformed and the level spacing changes.

2.5 Spectroscopic signatures

Hulkko *et al.* observed a surprisingly long-lived electronic (vibronic) coherence in I_2/Xe system. In the low-energy part of the absorption spectrum, corresponding to transition $B\,^3\Pi_u \leftarrow X\,^1\Sigma_g$, vibronic transitions were resolved as zero-phonon lines (ZPL) accompanied by phonon side bands (PSB). In the same study, resonance Raman showed two progressions of lines, where overtones were resolved up to $\nu = 18$ and $\nu = 8$. The former progression lines were sharp and showed only slight dependence on the vibrational quantum number ν, whereas the latter lines broadened rapidly with increasing vibrational state ν [115]. The electronic coherence in other rare gas matrices has been observed to be very short-lived (< 100 fs), dephasing occurring before the first recursion in the upper B-state as deduced from four-wave mixing (FWM) measurements [116–118]. To confirm the electronic coherence and elaborate on the differences in progression lines, quantum simulations of resonance Raman (Sec. 2.5.1) and CARS spectroscopies (Sec. 2.5.2) were performed. The propagation of the wavepacket was done on adiabatic potentials that were obtained from molecular dynamics (MD) simulations. The two spectroscopic techniques are discussed in the perturbative limit, adopting the viewpoint of Sec. 2.4.1.

Recent femtosecond pump-probe optical Kerr effect (OKE) measurements [14, 54] revealed a rotational coherence which lasted over 12 ps. The beating was observed in frequency sidebands using 2D (time-frequency) imaging. The signal was shifted from the probe center by an energy equal to $J : 2 \leftarrow 0$ transition. Furthermore, a beating consistent with a lattice phonon was observed at the center frequency. Our interest was focused on the roton sideband and we considered the time-evolution of the roton wavepacket in the basis set of crystal-field split states [Eq. (2.25)]. Here, the perturbative expansion cannot be applied due to high pulse intensities. The theoretical framework behind the molecular alignment and the simulation methods in the non-perturbative regime are presented in Sec. 2.5.3 along with a brief introduction to the optical Kerr effect spectroscopy.

2.5.1 Resonance Raman spectroscopy

We now enter the field of Raman spectroscopy, where an incident photon with frequency ω_I excites the initial molecular eigenstate $|\psi_i\rangle$ to an intermediate state, termed virtual state, and a scattered photon with frequency ω_S brings the system to a final state $|\psi_f\rangle$. If the scattering is elastic, the process is called Rayleigh scattering, $\omega_I = \omega_S$, and the molecule returns to the initial state. When the final state $|\psi_f\rangle$ is higher in energy than the initial state $|\psi_i\rangle$, term Stokes Raman scattering is used. The opposite case, where the $|\psi_f\rangle$ is lower in energy, is called anti-Stokes Raman scattering.

The incident photon can be either on-resonance or off-resonance with electronic state (or with any molecular eigenstate in general). The former is called resonance Raman (RR), where the scattering emanates from excited electronic state, and is the topic of this section.

In order to explain the Raman amplitude progression in the I_2-Xe we must go beyond the familiar Kramers-Heisenberg-Dirac (KHD) expression for the (vibronic) polarizability tensor α [27]:

$$(\alpha_{fi})_{\kappa\lambda}(\omega_I) = -\sum_{\xi}\sum_{\nu}\Big[\frac{\langle\psi_f|\hat{\mu}_{\xi,\kappa}|\psi_\nu\rangle\langle\psi_\nu|\hat{\mu}_{\xi,\lambda}|\psi_i\rangle}{E_i+\hbar\omega_I-E_{\xi\nu}+i\hbar\Gamma} + \frac{\langle\psi_f|\hat{\mu}_{\xi,\kappa}|\psi_\nu\rangle\langle\psi_\nu|\hat{\mu}_{\xi,\lambda}|\psi_i\rangle}{E_i-\hbar\omega_S-E_{\xi\nu}+i\hbar\Gamma}\Big]\,. \tag{2.43}$$

We use subscripts κ and λ for the field polarization and the summation is over excited electronic states (ξ) and vibrational states (ν) within the electronic state ξ. The first term is called the resonance term as the denominator approaches zero when the resonance condition $E_{\xi\nu} = E_i + \hbar\omega_I$ is met. Using the same reasoning, the second term is called the nonresonant term. In resonance Raman spectroscopy the latter term is dwarfed by the former and can be neglected. When the incident radiation is resonant with some excited electronic state, the summation over the electronic state manifold is unnecessary. It is important to note that even with the resonant condition the calculation of the Raman amplitude requires the knowledge of all vibrational eigenstates in both electronic states. More importantly, the above expression for the Raman amplitude is in the energy (frequency) domain where the system can be thought to have evolved for an infinitely long time. We are interested in the short-time dynamics of the wavepacket when it propagates on the upper potential surface. Therefore we use the time-dependent picture of the Raman scattering [119]. It should be noted after the transformation, the RR is still a frequency-domain technique, where the peaks positions match the vibrational transition frequencies $\Delta\nu = (E_f - E_i)/hc$. The line widths and intensities then show the dynamics in the ground and excited states.

In the CW case, the interaction Hamiltonian in the sequential two-photon Raman process is [27]

$$\hat{H}_{\text{ind}}(t'') = -\frac{1}{2}\hat{\mu}\cdot\epsilon_I e^{-i\omega_I t''} \quad \text{Incident} \tag{2.44}$$

$$\hat{H}_{\text{ind}}(t') = -\frac{1}{2}\hat{\mu}\cdot\epsilon_S e^{+i\omega_S t'} \quad \text{Scattering}\,, \tag{2.45}$$

and a perturbative expansion to second-order suffices. Contrary to the pulsed laser, the incident field is characterized by a single frequency. The time-domain expression of the vibronic polarizability $\alpha_{fi}(\omega_I)$ is [119]

$$\alpha_{fi}(\omega_I) = \frac{i}{\hbar}\int_0^\infty \langle\tilde{\psi}_f|\tilde{\psi}_i(t)\rangle e^{+i(\omega_I+\omega_i)t}\mathrm{d}t\,, \tag{2.46}$$

where $|\tilde{\psi}_f\rangle = \hat{\mu}_{ge}|\psi_f\rangle$ and $|\tilde{\psi}_i(t)\rangle = e^{-i\hat{H}_e t/\hbar}|\tilde{\psi}_i\rangle$. We see that the dynamics in the upper state is imprinted on the cross-correlation function $C_{fi} = \langle\tilde{\psi}_f|\tilde{\psi}_i(t)\rangle$ which gives the overlap between vibrational states f in the ground state g and the propagated molecular wavepacket at times t. Physically, this means that depending on the dynamics (or the nature of potential surface) the cross-correlation function can show recurrences. This arises if the wavepacket survives coherent long enough in the upper state and returns periodically to the initial Franck-Condon window. If the upper state is dissociative or decoherence is fast, the cross-correlation function decays monotonically in time and shows no recurrences. Therefore, the amplitude modulations in the polarizability gives insight on the dynamical properties of the wavepacket on the excited state.

Using the concept of Raman wavefunction $|R_{\omega_I}\rangle$ [120], the polarizability can be written alternatively in the frequency-domain

$$\alpha_{fi}(\omega_I) = \frac{i}{\hbar}\langle\psi_f|\hat{\mu}_{ge}|R_{\omega_I}\rangle \,, \tag{2.47}$$

where

$$|R_{\omega_I}\rangle = \int_0^\infty e^{-i\hat{H}_e\tau/\hbar}\hat{\mu}_{eg}e^{i(\omega_I+\omega_i)\tau}|\psi_i\rangle \mathrm{d}\tau \,, \tag{2.48}$$

which is related to the first-order wavefunction $|\psi^{(1)}\rangle$ as

$$|\psi^{(1)}(t')\rangle = -e^{-i\tilde{\omega}_I t'}\frac{\epsilon_I}{2i\hbar}|R_{\omega_I}\rangle \,. \tag{2.49}$$

The Raman wavefunction is what is usually termed the virtual state in Raman spectroscopy [27, 120]. Using the sequential two-photon point-of-view, the Raman wavefunction ($|R_{\omega_I}\rangle$) is the state from which the scattering ω_S (emission) emanates and dynamics is observed through the Raman wavefunction.

The resonance Raman intensity profile, expressed using $|R_{\omega_I}\rangle$, is

$$I_{\mathrm{RR}}(\omega_S) = \omega_I\omega_S^3\int \mathrm{d}t\, \langle\tilde{R}_{\omega_I}|e^{-i\hat{H}_g t/\hbar}|\tilde{R}_{\omega_I}\rangle \,, \tag{2.50}$$

where $|\tilde{R}_{\omega_I}\rangle = \hat{\mu}_{ge}|R_{\omega_I}\rangle$. The above equation can be interpreted as follows: the Raman wavefunction, which has the dynamical information of the excited state, now evolves on the ground state. While the modulation of the intensity is a manifestation of vibronic coherence, the line widths in I_{RR} reflect the vibrational coherence in the ground state. If the dynamics is short-lived, Rayleigh line $\Delta\nu = 0$ is dominant and is accompanied by rapidly weakening intensities for Raman overtone transitions $\Delta\nu > 1$. The same behaviour is seen if the incident laser frequency is tuned away from resonance. However, when the coherence survives for a time period that approaches vibrational period in the upper state, the Raman progression lines show stronger

overtone transitions. For gas phase iodine, the resonance Raman intensity I_{RR} has been observed to resolve the rotational branches $\Delta J = \pm 1$ as well as vibrational overtone transitions of $\Delta\nu = 9$ and higher, when the laser frequency was resonant with the B-state [121]. The intensities varied depending on the final state and the decay of the intensity was not monotonical. This is due to slow dephasing mechanisms (e.g. collisions) in the gas phase. In contrast, numerical study of resonance Raman of I_2 in Ar and Xe clusters showed a long, monotonically decaying overtone progression [122] which were consistent with the experimental spectra from Ar matrix [123] and in liquid Xe [124,125]. The dephasing time showed dependence on the cluster size as more lattice modes participated in the dephasing process. However, it was already speculated in Ref. [122] that recurrences might be observed in solid xenon. This would require that the coherence survives for a time interval longer than a half-vibrational period, that is, after the I atoms have collided with the Xe host.

In the present case [III], due to instrumental limitations, the true line widths of the Raman progression lines were obscured. Therefore we do not represent the I_{RR} spectra, but give the results as the Raman cross section $\sigma^{f\leftarrow i}$ instead:

$$\sigma^{f\leftarrow i} = \frac{8\pi\omega_I\omega_S^3}{9c^4}|\alpha_{fi}(\omega_I)|^2 \,. \tag{2.51}$$

In solid state conditions, the molecular rotation of iodine becomes suppressed and the steady state spectroscopy does not exhibit the doublet branch owing to the rotational transitions. As will be discussed in Sec. 3.2, RR progression from I_2/Xe exhibits a doublet, due to different trapping sites of I_2, whose positions in the energy domain are dictated by the matrix-induced shifts (Sec. 2.2.1). Additionally, the low temperature allows to limit the computational consideration to single initial vibrational state, $\nu = 0$.

The numerics are done using Eq. (2.47) for the initial state $i = 0$ and laser wavelength $\lambda_I = 532$ nm. In the numerical propagation scheme, as Eq. (2.49) shows, the iteration [see Eq. (2.38)] can be stopped at $n = 1$:

$$\begin{aligned} |\psi^{(1)}(t+\Delta t)\rangle &= e^{-i\hat{H}_e\Delta t/\hbar}|\psi^{(1)}(t)\rangle \\ &\quad - \frac{i}{2\hbar}\Delta t\mu(r)\epsilon_I e^{-i\tilde{\omega}_I(t+\Delta t)}|\psi^{(0)}(t+\Delta t)\rangle \,, \end{aligned} \tag{2.52}$$

and the intensity profile is gained by projecting $|R_{\omega_I}\rangle$ onto the effective ground vibrational states $|\tilde{\psi}_f\rangle = \hat{\mu}_{ge}|\psi_f\rangle$. The dependence of the transition dipole moment on the bond length r was taken into consideration through the expression in Ref. [126]. Note that now only the vibrational states on the ground electronic state are required in contrast to the KHD expression. The loss of coherence during the excursion on the upper state is done by introducing dephasing function $\exp[-g(t)]$, where

$$g(t) = \begin{cases} t^2/2\sigma^2, & \text{or} \\ t/T_2 & . \end{cases} \tag{2.53}$$

2.5.2 Coherent anti-Stokes Raman scattering

In RR, being a CW frequency-domain spectroscopy, the dynamics is observed through the intensity distribution of the Raman progression lines. The coherent anti-Stokes Raman scattering (CARS) spectroscopy is a four-wave mixing technique and is widely used for interrogation of molecular coherences. When applied in the time-domain using femtosecond laser pulses, vibrational states either in the ground or excited electronic state can be resolved. In the weak-field limit, three incoming fields create a third-order polarization $P^{(3)}(t)$ which then emits a photon in a direction other than the incoming fields. The first pulse is termed pump, the second as Stokes or dump, and the third as probe. The electric field that carries the information on the polarization is propagating in the phase-matching direction $\mathbf{k}_{\mathrm{aS}} = \mathbf{k}_{\mathrm{pump}} - \mathbf{k}_{\mathrm{Stokes}} + \mathbf{k}_{\mathrm{probe}}$. Manipulation and detection of coherences are controlled by the wavelengths and the time intervals between pulses. The theory is well established and in the weak field limit the third-order polarization $P^{(3)}(t)$ is [111]:

$$P^{(3)}(t) = \langle \psi^{(0)}(t)|\hat{\mu}|\psi^{(3)}(t)\rangle + \langle \psi^{(2)}(t)|\hat{\mu}|\psi^{(1)}(t)\rangle + \text{c.c.}\,, \tag{2.54}$$

where the wavepackets in different perturbation orders n are given by Eq. (2.37). In general, eight double-sided Feynman diagrams that correspond to CARS experiment arise [127], here the diagram shown in Fig. 2.3 (a) and its complex conjugate are enough. The approximation is sufficient as long as the pulses do not overlap; the pump excitation is near the absorption maximum and therefore the dump absorption should be weak; and/or as long as the dump and probe frequency difference does not correspond to a thermally populated initial state.

The evaluation of the third-order polarization $P^{(3)}(t)$ now reduces to calculation of the first term and its complex conjugate in Eq. (2.54):

$$P^{(3)}(t) = \langle \psi^{(0)}(t)|\hat{\mu}|\psi^{(3)}(t)\rangle + \text{c.c.} \tag{2.55}$$

Using time-dependent perturbation theory up to third-order, $P^{(3)}(t)$ obtains an expression [128]

$$\begin{aligned} P^{(3)}(t) = \frac{-i}{\hbar^3}\int_{-\infty}^{t}\mathrm{d}t_3\int_{-\infty}^{t_3}\mathrm{d}t_2\int_{-\infty}^{t_2}\mathrm{d}t_1 \langle \psi^{(0)}(t)|\hat{\mu}_{ge}|e^{-i\hat{H}_e(t-t_3)/\hbar}\,[\hat{\mu}_{eg}E_3(t_3)] \\ \times e^{-i\hat{H}_g(t_3-t_2)/\hbar}\,[\hat{\mu}_{ge}E_2^*(t_2)]\,e^{-i\hat{H}_e(t_2-t_1)/\hbar}\,[\hat{\mu}_{eg}E_1(t_1)]\,e^{-i\hat{H}_g t_1/\hbar}|\psi^{(0)}\rangle\,. \end{aligned} \tag{2.56}$$

A dynamical interpretation can now be given. The initial wavepacket $|\psi^{(0)}\rangle$ acquires a phase under the ground state Hamiltonian H_g until time t_1 when the pump pulse interacts with the system. The first-order wavepacket then evolves under the Hamiltonian H_e for an interval $t_2 - t_1$. The dump pulse interacts at time t_2, creating second-order wavepacket to the ground state g where it evolves for time interval $t_3 - t_2$. At t_3, the

probe pulse excites the third-order packet to the e-state until at t anti-Stokes scattering is observed. The expression indicates the dynamics on the excited and ground state, imprinted on the third-order polarization, are controlled by the time periods $t_3 - t_2$ and $t_2 - t_1$ in a similar manner as in the pump-probe experiments. An energy level diagram of the CARS process is shown in Fig. 2.3 (b), with rovibrational states indicated in the figure. We see that CARS probes the coherences between rovibronic states, without creating intermediate populations. Therefore the population decay is not in effect and the loss of coherence is due to pure dephasing alone.

In general, there are two ways to detect the coherences imprinted on the anti-Stokes beam, the homodyne and heterodyne detection. In this section, the homodyne detection is considered. The heterodyne detection, where the signal field is mixed with so-called local oscillator field, is considered in the solid para-hydrogen case in Sec. 2.5.3. Due to square-law detection, the time-resolved signal S is proportional to the square of the polarization:

$$S = \int \mathrm{d}t \left| P^{(3)}(t) \right|^2 \tag{2.57}$$

for which Faeder *et al.* derived an expression in the time-domain [127]:

$$S = \frac{2}{\hbar^6} \sum_{ii',ff'} p_i p_{i'} \int \mathrm{d}T a_{fi}(T) a^*_{f'i'}(T) e^{-i(\omega_{fi} - \omega_{f'i'})T} \,. \tag{2.58}$$

The time $T = t - \tau_3$ is the time period between emission at t and the center of probe pulse τ_3, and corresponds with the time the third-order coherence lives in the excited state. Factors p_i are the Boltzmann weights of the initial state in the statistical ensemble. The product between the amplitudes $a_{fi}(T)$ and $a^*_{f'i'}(T)$ reveal the oscillatory nature of the signal as a function of delay between pump-dump (τ_{21}) and dump-probe (τ_{32}):

$$a_{fi}(T) a^*_{f'i'}(T) \propto \sum_{nn',jj'} e^{-i(\omega_{jj'} - \omega_{ii'})\tau_{32}} e^{-i(\omega_{nn'} - \omega_{ii'})\tau_{21}} \,. \tag{2.59}$$

The signal oscillates at the frequencies which correspond to the separation between energy eigenstates in the excited or ground state when time delay τ_{21} or τ_{32} is scanned, respectively. Therefore, knowledge of the level structure can be deduced from the beating. When the system is in pure state, $i = i'$, the signal oscillates at the difference frequencies in the wavepacket. The beats are commonly referred quantum beats which are an intramolecular effect. When $i \neq i'$, so-called polarization beats arise. These are understood as an intermolecular effect due to the interference of radiation from molecules in different initial states. Therefore, the polarization beats can be used to identify different species; in our laboratory, polarization beats were assigned between I_2-Xe complex and uncomplexed iodine [129,130] and between I_2 and I_2-benzene complex [131], in solid krypton. In Publication III, the computations describe iodine in a pure state as the polarization beats between two trapping sites, which manifest themselves in the RR spectra as the doublet progression, could not be identified from

the experimental traces. The time-resolved CARS traces are discussed in Sec. 3.2.2. Quantum beats in the frequency domain again manifest the static, matrix-induced shifts. The dynamical part (dephasing) can be interpreted either from the line widths or from the decay in time domain. The CARS signal of I_2, measured from crystalline Xe, exhibits only the vibrational motion of the molecule, and subsequently the time traces show only quantum beats belonging to vibrational energy spacings. In the gas phase, the fast vibrational oscillations in the CARS signals become modulated in the picosecond timescale due to rotation [132].

The polarization $P^{(3)}(t)$ can also be studied using two-dimensional (time-frequency) imaging by dispersing the anti-Stokes beam through a monochromator. Previously this approach has been used to interrogate and manipulate the molecular coherences of I_2 in the gas phase [133–135]. In time-gated frequency-resolved CARS (TGFCARS) (Ref. [133]), a time-slice of the signal is selected by an optical Kerr gate and then detected through a monochromator. This can be presented by taking a Husimi transform of the third-order polarization after fixing time delays τ_{21} and τ_{32}. Another choice is to collect the radiation without gating, and record the signal in a time-integrated mode [134, 135]:

$$S(\omega;\tau_{32},\tau_{21}) = \left| \int \mathrm{d}T e^{-i\omega T} i P^{(3)}(T;\tau_{32},\tau_{21}) \right|^2 . \tag{2.60}$$

By scanning the τ_{21} or τ_{32}, the first- or second-order coherences are interrogated, but the beating is observed as intensity variations in the power spectrum, having the same periodicity as in the time-resolved CARS signal. The dephasing time, which depends on the interactions between the medium and the impurity, dictates whether the (ro)vibrational transitions to the ground state become resolved in the frequency domain of time-integrated images. An intermediate case will be discussed in Sec. 3.2.2 for the surprisingly long-lived coherence observed in solid Xe. Clearly resolved rovibrational branches arise in the case of CN radical in Sec. 3.3. Additionally, the interactions between the host and guest dictate the degree of rotational hindrance, as was mentioned in Sec. 2.2.1, and may lead to greatly simplified time-frequency images in matrix-isolation studies as the interferences between rotational states in vibronic manifolds are not observed.

The time-domain propagation follows the same iterative scheme as in the RR, but now up to third-order. The field term has time-dependent Gaussian envelope and corresponds to pulsed laser field with duration in the femtosecond regime [Eq. (2.34)]. The center of the dump and probe pulses were fixed in time according to time delays τ_{21} and τ_{32}, and the first pulse was centered away from the $t = 0$. After propagation, dephasing was introduced as $\exp[-\Gamma t]$ where Γ is the inverse of dephasing time T_2.

The numerical implementation follows Eq. (2.57) by collecting the polarization up to a chosen decay time. This results in oscillatory signals, time traces, as a func-

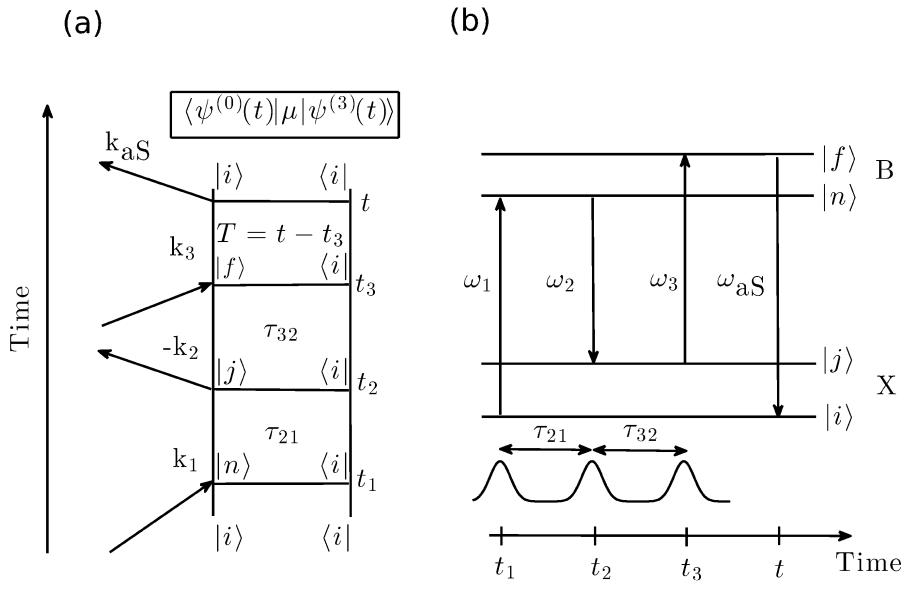

Figure 2.3: (a) The relevant double-sided Feynman diagram for the present CARS setup, assuming a two-level electronic system [127]. The Liouville pathway corresponds to $P^{(3)}(t) = \langle\psi^{(0)}(t)|\hat{\mu}|\psi^{(3)}(t)\rangle$ in the direction $\mathbf{k}_{\text{pump}} - \mathbf{k}_{\text{Stokes}} + \mathbf{k}_{\text{probe}}$. (b) Schematic representation of the excitation path $|gi\rangle \rightarrow |en\rangle \rightarrow |gj\rangle \rightarrow |ef\rangle$. The levels must be understood as superpositions of rovibronic levels in a general case. A special case of rotational states only is shown in Fig. 2.4.

tion of time delays. Taking a Fourier transform of the time trace, wavepacket composition can be observed as peaks in the frequency domain which correspond to the frequencies in $e^{-i(\omega_{jj'}-\omega_{ii'})\tau_{32}}e^{-i(\omega_{nn'}-\omega_{ii'})\tau_{21}}$. In time-integrated frequency-resolved CARS, the Fourier transform was systematically taken from the third-order polarization $P^{(3)}$, as Eq. (2.60) suggests. The two-dimensional imaging has advantage over TRCARS, namely that the frequencies between the final and initial states are observed [Eq. (2.58)]. This leads to observation of rotational branches in the case of CN. The hyperbolic trails seen in the experimental TGFCARS images for gas phase I_2 [133] are not predicted to show up in the case of CN, as low temperature limits the initial rotational population (Sec. 3.3).

We did not specify the molecular coherence above, the states were rovibronic states in electronic potentials. For I_2/Xe system, the vibronic manifolds suffice. In this case the iterative propagation scheme up to $n = 3$ is used with Gaussian shaped pulse envelopes. In the gas phase, Meyer *et al.* [132, 136–138] included the rotational states into the propagation by using the transition rule $\Delta J = \pm 1$ for the angular momentum J (with $M = 0$) when transitions between electronic states were considered. This sums up to propagation of six wavefunctions for a single initial vibrational state. We used same approach for CN in Publication IV, without the excitation of a vibronic superposition state.

The transition rule $\Delta N = \pm 1$ (Ref. [4]) is assumed to apply for CN in Xe. Schallmoser *et al.* observed weak Q-branch ($\Delta N = 0$) and speculated the origin to be slightly hindered rotation (increased moment of inertia). However, their results clearly indicate that the rotation of CN is least hindered in solid Xe as compared to other rare gas matrices [139–141]. A theoretical approach was taken for the CN rotation in Xe where the cage effect is neglected and adiabatic potentials are taken to be Morse potentials. The parameters ω_e and $\omega_e x_e$ pertain to the gas phase values (taken from Ref. [141]) and we neglected the red-shifted vibrational and electronic energies in Xe [139–141]. The inclusion of electronic and vibrational energy level shifts from gas phase would affect the experimental realization but not the physical picture.

Peculiarity of CN, when compared to I_2, is the large (~ 2000 cm^{-1}) vibrational energy level separation. Therefore, even with broad bandwidth femtosecond laser pulses only a single vibrational state ν is picked during each interaction with pump, dump, and probe. Effectively, this reduces to choosing a single path in the vibrational space. For CN, the pathway where $\nu : 0 \to 0 \to 1 \to 1$ was chosen. The vibrational path follows the sequential order of the pulses. The rotational energies are incorporated in the simulations by considering the potential as a sum of vibronic and rotational energies

$$V = V(r) + \frac{\hbar^2 N(N+1)}{2\mu r^2} \,, \tag{2.61}$$

where the rotational quantum number N was introduced in Sec. 2.1. Six rotational paths p can then arise in general; the rotational wiring diagram can be seen in Fig. 2.4. For initial states $N_i = 0, 1$ the number of possible paths is two and five respectively. The propagation scheme in Eq. (2.38) is expanded to include the wavefunctions of rotational paths p and the couplings between them:

$$\begin{aligned} |\psi_p^{(n)}(t+\Delta t)\rangle &= e^{-i\hat{H}_0 \Delta t/\hbar} |\psi_p^{(n)}(t)\rangle \\ &- \frac{i}{\hbar} \Delta t \mu_{pp'} E_n(t+dt) |\psi_{p'}^{(n-1)}(t+dt)\rangle \,. \end{aligned} \tag{2.62}$$

Effectively this means that after the first interaction two first-order wavefunctions are propagated, then four second-order and finally six third-order wavefunctions propagate in the excited state after the third (probe) interaction. For each wavefunction, the vibrational state on which the rotational coherence evolves is obtained by the FGH method (Sec. 2.1.1). The dipole moment for a parallel transition between electronic states was considered to be a constant and the rotational line strength factors $\sum_{M_N''} \langle N' M_N' | \cos\theta | N'' M_N'' \rangle$ for each of the paths were used.

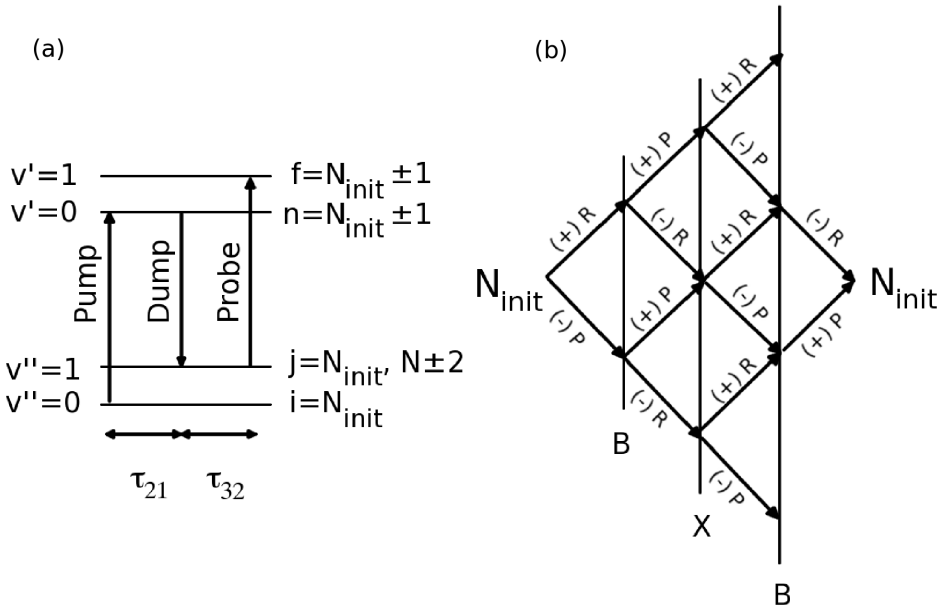

Figure 2.4: A schematic representation of the general rotational excitation pathway in CN radical with three time-delayed pulses. The double-sided Feynman diagram shown in Fig. 2.3 applies here too, only the states are rotational eigenstates in a single vibrational state in either ground or excited electronic surface. (a) The vibrational path $0 \to 0 \to 1 \to 1$ along with the possible rotational states after the pump, dump, and probe. After the three interactions, the polarization emits a photon in the phase-matched direction and the system returns to initial rovibrational state. (b) The rotational "wiring" or connection diagram for the six possible paths p. The plus and minus signs denote the change $\Delta N = \pm 1$ in the rotational quantum number N.

2.5.3 Femtosecond pump-probe optical Kerr effect spectroscopy

In an isotropic sample, the molecules are initially randomly oriented but after application of a laser pulse, the molecules can become aligned or oriented along the polarization direction of the applied field. The case of interest here is the molecular alignment of para-hydrogen by short and intense laser pulses off-resonant with any electronic, vibrational or rotational states. The excitation takes place via Raman-type transitions $\Delta J = 0, \pm 2$ and the molecule remains in the ground vibrational state. Additionally, as the fs-pulses are short compared to rotational period $\tau_{\text{rot}} = 1/2Bc = 280$ fs, where $B = 59.32$ cm^{-1} is the rotational constant and c is the speed of light, the interaction with the pulsed laser initiates the time-evolution of a coherent rotational (roton) wavepacket. The full revival time in the case of rotational wavepackets is given by the rotational period τ_{rot} which also dictates the periodicity in all the expectation values obtained from the wavepacket. The width in the rotational space and the spatial localization of the wavepacket in angular space can be controlled by the field intensity and pulse duration [142]. Effectively, it is the reorientational motion persisting after the pulse that induces anisotropy in the sample as the electronic response decays rapidly after the pulse.

The alignment of a linear molecule with linearly polarized light has been exhaustively studied in the gas phase (see e.g. Ref. [143]). The induced Hamiltonian in this case is dependent on the polar Euler angle θ between the molecular axis z and the laboratory axis Z (polarization direction of the laser field):

$$H_{\text{ind}}^{\text{gas}} = -\frac{1}{4}\varepsilon(t)^2 \left(\Delta\alpha \cos^2\theta + \alpha_\perp\right) . \tag{2.63}$$

Few remarks of the above equation: (1) the prefactor $\varepsilon(t)^2$ includes the intensity of the radiation and the pulse envelope (Gaussian); therefore the control by pulse duration and intensity is through this term; (2) the anisotropic polarizability of the molecule, $\Delta\alpha = \alpha_\parallel - \alpha_\perp$, mediates the interaction between the field and molecule when no permanent dipole moment exists. The polarizability tensor α of a diatomic has only two nonzero components, i.e., the components parallel ($\alpha_\parallel$) and perpendicular ($\alpha_\perp$) to the molecular axis. The polarizability cannot distinguish the two ends of diatomic and therefore the laser field only aligns not orients.

The optical detection of the nuclear response in the present case was done with pump-probe optical Kerr effect spectroscopy. In this technique the first field, termed pump, induces the anisotropy as the molecules get aligned along the field polarization. Using nomenclature and concepts from the field of optics, the media becomes birefringent, i.e., the refractive index becomes dependent on the propagation direction of the pulse. The birefringence is then investigated through the change in polarization state of a time-delayed second pulse, the probe. The birefringent media, due to different optical axes, induces a phase shift between polarization vectors that rotate in a plane

perpendicular to beam propagation. This is identical to an induction of an elliptical component to the initially linearly polarized light.

The case where both pulses are weak can be considered by calculating the third-order polarization $P^{(3)}(t)$ and this was done e.g. by Morgen *et al.* [144, 145] where they studied the tensorial nature of the birefringence. They termed their technique as Raman induced polarization spectroscopy (RIPS) but there is no principal difference between OKE and RIPS techniques. The optical polarization $P(t)$ in the direction $\mathbf{k}_{\mathrm{s}} = \mathbf{k}_{\mathrm{pump}} - \mathbf{k}_{\mathrm{pump}} + \mathbf{k}_{\mathrm{probe}}$ after application of intense pump and weak probe pulses was considered by Yan and Mukamel [146]. Here, the latter approach is of relevance; the pump interaction is carried out by numerical simulations in the nonperturbative, field-free alignment regime after which the time delay between probe and pump is varied and the signal computed using square-law detection.

The nonlinear pump-probe scheme can be described by using double-sided Feynman diagrams (see Fig. 2.5) [147, 148]. Two Liouville pathways, corresponding to different physical processes occurring via stimulated Raman scattering, give a Stokes-like and an anti-Stokes-like transition frequencies. A two-dimensional time-frequency imaging reveals the Raman transitions as red- and blue-shifted bands, respectively, from the probe center frequency by the transition energy between $J = 0$ and $J = 2$ roton states (the upper manifold split into three substates). The present account corresponds to a measurement in the time-domain without dispersion.

The pump beam is linearly polarized in the space-fixed Z-direction and the probe polarization (linear) is turned 45 degrees with respect to pump polarization. The analyzer behind the sample is used to block the probe field when no anisotropy is present. As the probe passes the sample, it acquires elliptic component due to pump-induced birefringence, and can now partially pass through the analyzer. To increase the signal-to-noise ratio, the signal field, i.e. the elliptic component of probe, is mixed with a local oscillator. Due to square-law detection, the intensity $I = |E_s + E_{\mathrm{lo}}|^2$ has a homodyne part $I_{\mathrm{hom}} = |E_s|^2$, a heterodyne part $I_{\mathrm{het}} = 2\mathrm{Re}\{E_s E_{\mathrm{lo}}^*\}$, and a local oscillator part $I_{\mathrm{lo}} = |E_{\mathrm{lo}}|^2$. The homodyne intensity carries the low frequency beats of the system response: the oscillation periods match the energy differences between $|M|$-states in Eq. (2.25). The heterodyne part carries the high frequency beats of the $J : 2 \leftarrow 0$ roton excitation (transition frequencies to $|M|$-split manifold). The introduction of local oscillator is experimentally realized by turning the probe polarization by a small angle so that actually a small portion of the probe can initially pass through the analyzer and subsequently to the detector. The time-dependent response is imprinted in the intensity modulation of I_{hom} and I_{het} and the local oscillator adds a time-independent background to the signal.

The para-hydrogen crystals are grown from gaseous para-hydrogen at low temperatures and the hexagonal axis (c-axis) of the hcp lattice becomes perpendicular to the

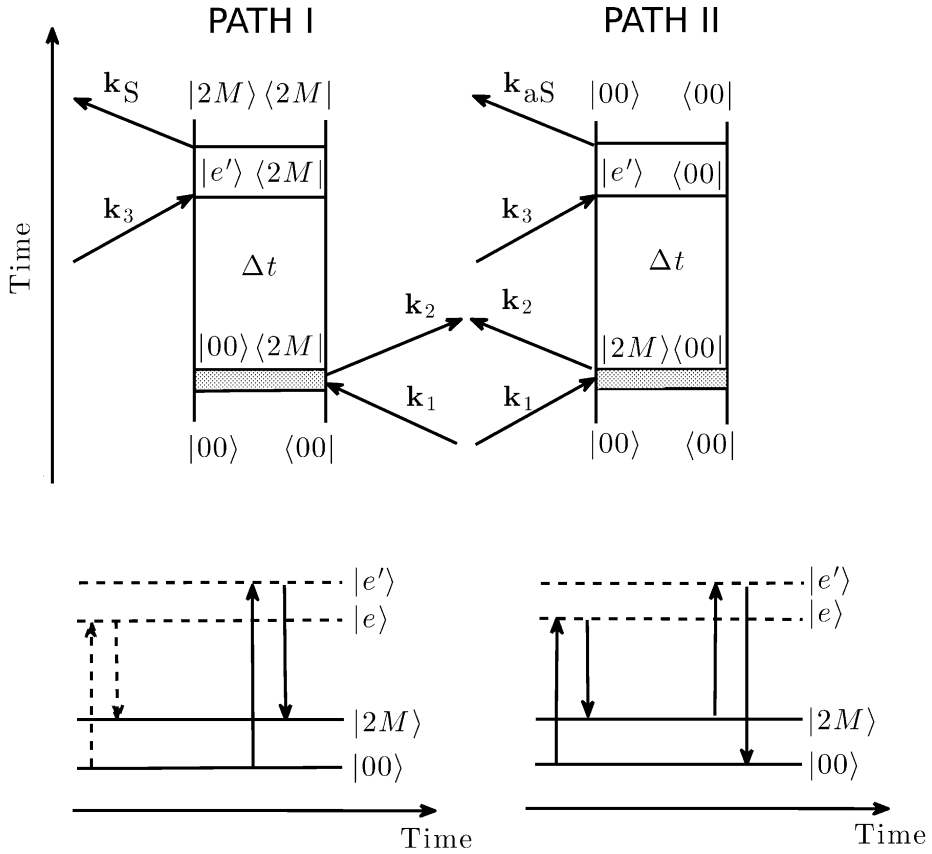

Figure 2.5: The two Liouville pathways that contribute to the optically detected birefringence [147]. The pumps are considered to coincide temporally, the darkened area in Feynman diagram describes the imprecision in the pump centers. The third interaction is with probe, delayed by Δt. The two processes, however, have a different physical interpretation. In path I, coherence is first created via pump-stimulated scattering from the virtual state $|e\rangle$. The spontaneous scattering of the probe then ensues. The final population lies on the $J = 2$ manifold and the resulting Stokes-like radiation is red-shifted from the probe center frequency. In path II, all the interactions are from the left, and this is recognized as CARS process, except now the stimulated Raman scattering originates from virtual state. The scattering is therefore anti-Stokes-like and a blue-shift from the center frequency is observed. In the energy level diagram, a solid arrow represents interaction from the left and dashed arrow interaction from the right. The figure is adapted from Ref. [147].

copper cylinder surface which hosts the matrix. The beam propagation direction coincides with the cylinder axis and has certain consequences on the theoretical treatment which is discussed below.

To quantify the alignment, three coordinate frames must be defined: laboratory, crystal, and molecular. The polarization of the field again defines the laboratory frame, with Z-axis taken to be the polarization direction. Contrary to the gas phase, the molecular orientation is not defined with respect to space-fixed frame (laboratory frame), but relative to hcp lattice frame (crystal axes). The definition of the Euler angles $\{\theta', \phi', \chi'\}$, which describe the orientation of the crystal frame with respect to the laboratory frame, is done using the definition of Zare [21]. The angle ϕ', corresponding to the first Euler rotation, must be zero as the beam path is fixed along the space-fixed axis Y. This specific situation is depicted in Fig. 2.6. The rotation of the molecule is defined in the crystal frame using the polar angle θ and azimuthal angle ϕ that were shown already in Fig. 2.1 (Sec. 2.1).

The system Hamiltonian in the solid para-hydrogen case becomes

$$\frac{\mathrm{d}|\Psi_{\mathrm{rot}}(t)\rangle}{\mathrm{d}t} = -\frac{i}{\hbar}\left[\hat{H}_{\mathrm{rot}} + \hat{H}_{\mathrm{cry}} + \hat{H}_{\mathrm{ind}}(t)\right]|\Psi_{\mathrm{rot}}(t)\rangle \tag{2.64}$$

where the crystal field part $\hat{H}_{\mathrm{cry}}$ is the one derived by Kranendonk [Eq. (2.25)] and $\hat{H}_{\mathrm{rot}}$ is the rotational part of the molecular Hamiltonian [Eq. (2.9)]. Now the pump field is considered to be intense which necessitates going beyond the perturbative approach. The solution is done in the eigenbasis of the free rotor:

$$|\Psi_{\mathrm{rot}}(t)\rangle = \sum_{JM} c_{JM}(t)|JM\rangle\,. \tag{2.65}$$

Inserting the trial solution to the TDSE, a coupled differential equation must be solved in order to obtain the coefficients c_{JM}:

$$i\hbar\dot{c}_{JM}(t) = \sum_{J'M'}\left[\langle JM|\left(\hat{H}_{\mathrm{rot}} + \hat{H}_{\mathrm{cry}}\right)|J'M'\rangle + \langle JM|\hat{H}_{\mathrm{ind}}(t)|J'M'\rangle\right]c_{J'M'}(t)\,. \tag{2.66}$$

The first term $(\hat{H}_{\mathrm{rot}}+\hat{H}_{\mathrm{cry}})$ is diagonal in the free rotor $|JM\rangle$ basis, given by Eqs. (2.9) and (2.25) respectively. The rotational and centrifugal constants along with the constant in the crystal field term were rescaled in order to achieve agreement with the experimental transition frequencies.

The field-molecule interaction is defined in the crystal frame and expressed using the field components in laboratory frame and the polarizability tensor elements in the molecular frame. Using short-hand notation $Y_{2m} = Y_{2m}(\theta, \phi)$, the Hamiltonian is

written as [V]:

$$\begin{aligned} H_{\text{ind}} &= -\frac{1}{4}\varepsilon(t)^2\Delta\alpha \times \Big[Y_{20}\sqrt{16\pi/45}(\cos^2\theta' - \frac{1}{2}\sin^2\theta') \\ &+ (Y_{22}+Y_{2-2})\sqrt{2\pi/15}\sin^2\theta'(\cos^2\chi' - \sin^2\chi') \\ &+ (Y_{21}-Y_{2-1})\sqrt{8\pi/15}\sin\theta'\cos\theta'\cos\chi' \\ &+ i(Y_{22}-Y_{2-2})\sqrt{8\pi/15}\sin^2\theta'\sin\chi'\cos\chi' \\ &+ i(Y_{21}+Y_{2-1})\sqrt{8\pi/15}\sin\theta'\cos\theta'\sin\chi'\Big] \ . \end{aligned} \tag{2.67}$$

The individual wavepacket components with c_{JM} are now functions of the Euler angles θ' and χ' whereas the absolute square of the coefficients, $|c_{JM}|^2$ are independent of the angle χ'. It is the angle dependence that dictates here the appearance of optical Kerr effect signal. It is important to note that the transition rule $\Delta M = 0$, which is in effect when gas phase alignment with linearly polarized pulses is considered, does not apply in the case of roton excitation in solid para-hydrogen. This is clear from the inclusion of spherical harmonics $Y_{2M}(\theta,\phi)$ with $M \neq 0$ to the above Hamiltonian.

Numerically, only the two lowest J-manifolds $J = 0$ and $J = 2$ are considered, consistent with the roton excitation. This equates to wavepacket having six states in the $|JM\rangle$ basis with coefficients $c_{JM}(t)$. The calculation of the spherical harmonic matrix elements $\langle JM|Y_{2m}(\theta,\phi)|J'M'\rangle$ in Eq. (2.66) reduces to tabulation of Clebsch-Gordan coefficients [21]. The coupled equations (2.66) were solved using Runge-Kutta method. The emphasis is put on the spatial (θ',χ') part in the crystalline case, not on the pulse properties, because at low temperatures only the $J = 0$ is thermally populated and is the main component in the roton wavepacket at the intensities used in the experiments.

The intensity I of the signal after the propagation of the probe through the birefringent media is implemented in Publication V as

$$I(\tau) \ = A \int \mathrm{d}t\, \varepsilon^2_{\text{probe}}(t-\tau)\left[I_\Gamma(t)^2 + 2CI_\Gamma(t)\right] \ , \tag{2.68}$$

where

$$I_\Gamma(t) = \frac{\Delta\alpha}{2}\left[\langle\cos^2\Theta\rangle(t) - \langle\sin^2\Theta\cos^2\Phi\rangle(t)\right]e^{-\Gamma t} \ . \tag{2.69}$$

The parameter C controls the relative contributions from the homo- and heterodyne parts. The angles between laboratory and molecular axis orientation are denoted by capital letters Θ and Φ to distinguish them from the angles θ and ϕ defined in crystal frame. The dephasing time is 90 ps ($= \Gamma^{-1}$), as the measurements suggest. The probe field $\varepsilon_{\text{probe}}$ was Gaussian with a duration of 130 fs, consistent with the experimentally estimated [54].

The states $|JM\rangle$ are defined in the crystal frame, but the operators are defined by the relative orientations of the molecular and laboratory frames. Therefore, the operators

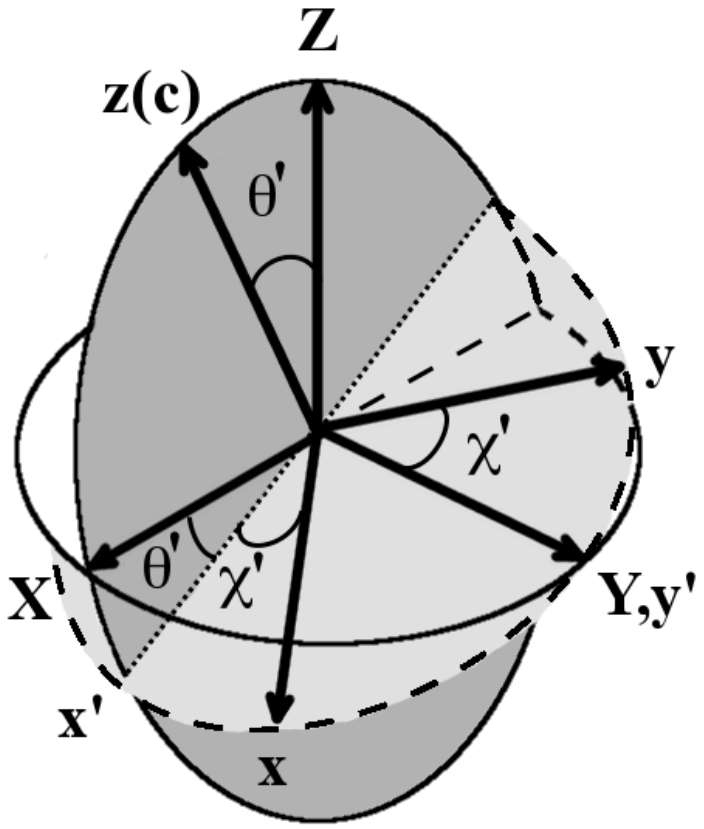

Figure 2.6: A schematic picture of the relative orientation between the crystal $\{x, y, z\}$ and laboratory $\{X, Y, Z\}$ frame. The laser beam propagates along the Y-axis which in turn dictates that angle ϕ' must be zero. The second Euler rotation by an angle θ' around the Y-axis (or y') occurs in the XZ-plane (dark gray). The final rotation by angle χ' is around the hexagonal $z(c)$-axis and defines the xy-plane (light grey). Copyright © 2013 by The American Physical Society.

must be expressed in the crystal frame or the states in the laboratory frame. In Publication V, we chose to express operators using spherical harmonics (tensor operators) $Y_{2m'}(\Theta, \Phi)$ and relate the components m' to the crystal frame with the help of Wigner D-functions. For the expectation value of $\cos^2\Theta$, the procedure gives

$$\langle \cos^2\Theta \rangle \;=\; \frac{1}{3} + \sqrt{\frac{16\pi}{45}} \sum_{m'} d^{(2)*}_{0,m'}(\theta') e^{im'\chi'} \langle Y_{2m'}(\theta, \phi) \rangle \; . \tag{2.70}$$

The calculation requires the knowledge of Wigner $d^{(2)*}_{0,m'}$-functions, which are readily available [21], along with the expectation values of spherical harmonics with $m' = -2, \ldots, 2$ in the rotational wavepacket. The expectation value $\langle \sin^2\Theta \cos^2\Phi \rangle$ can be expressed as a sum of spherical harmonics $Y_{22}(\Theta, \Phi)$, $Y_{2-2}(\Theta, \Phi)$, and $Y_{20}(\Theta, \Phi)$. The functions are then expressed as in above equation [V].

3 Main results and discussion

3.1 Raman and IR spectroscopy of CO and H_2 in solid argon

The photodissociation of the precursor formaldehyde was done at dilution ratios 1/150 and 1/750 at 9 K in Publication II. After annealing, the rovibrational spectra for CO showed similar spectral band structure as found previously for CO as a single dopant in argon, see e.g. Ref. [85]. The results are in accord with similar photolysis measurements made by Vaskonen and Kunttu [66]. The photoproduct bands were located at 2136.5 cm^{-1}, 2138.3 cm^{-1}, 2139.9 cm^{-1}, and 2149 cm^{-1} and are referred as bands A, B, C, and D, respectively. After annealing, brodening of band B was observed in IR, but not in Raman spectra. This made us to consider the isolated case further by both IR and Raman spectroscopies in Publication I. The isolated case was investigated theoretically by constructing the rotational potential. A two-site model was developed which parallels the model in Ref. [86]. The assignment of the bands and the model are discussed Sec. 3.1.1.

The rotational Raman spectra of spin isomers pH_2 and oH_2 were dominated by a sharp central band at 347.2 cm^{-1} and 578.3 cm^{-1}, respectively. This was the case regardless of dilution ratio. Additionally, a split sub-structure was observed, more pronounced with lower concentration of formaldehyde: side bands were resolved at 344.8 cm^{-1} and 350.5 cm^{-1} for pH_2 at 10 K after annealing cycle. Similarly for oH_2, a side band at 572.1 cm^{-1} was resolved and a band at 583.6 cm^{-1} appeared after annealing. Also a shoulder band at 580.4 cm^{-1} emerged at higher concentration. A possible origin for the spectral fingerprints is given in Sec. 3.1.2.

3.1.1 The two-site model for monomeric CO

Infrared spectra corresponding with $\nu : 1 \leftarrow 0$ transition were found [I] to be consistent with previous results by Abe *et al.* [85,87,88]. The emphasis was put on the two most red-shifted bands A and B. The C and D bands were assigned to CO-CO dimers and CO-H_2O intermolecular complexes.

To resolve the origin of bands A and B, calculations of rotational potentials were

performed on CO in single- and double-substitution sites. Two approaches for the SS case were considered: (1) The adiabatic potential method where the host/guest positions are relaxed at every orientation. The pseudorotating lattice model was then used to estimate the reduction of B_0 from the gas phase. (2) The fixed lattice method, where the atoms and molecule positions are relaxed only for a single orientation and the rest of the angular space is sampled in the once relaxed configuration. The FGH calculations gave the value of 2141.6 cm^{-1} for the band origin in (1) and (2) as the molecular orientation is set to equivalent minimum energy directions.

The fully adiabatic rotational potential showed minima in the six crystal axis directions $\langle 100 \rangle$, maxima at eight $\langle 111 \rangle$ directions (three-atom window), and saddle points at twelve $\langle 110 \rangle$ directions where molecular axis points toward a nearest argon. The pseudorotating lattice model gave for B_0 an effective value $B_{\mathrm{eff}} = 1.24$ cm^{-1}. The ground librational $n = 0$ manifold was split into three substates which correlate asymptotically with the free rotor states $J = 0 - 2$. Using the irreducible representations of the O_h group, these states were designated as $A_{1\mathrm{g}}(1)$, $T_{1\mathrm{u}}(3)$, and $E_{\mathrm{g}}(2)$ where the number in parentheses indicate the level degeneracy. The next librational manifold of states, $n = 1$, was energetically close to the rotational barriers. The orientational motion can be categorized as hindered rotation. The potential landscape and the value of B_{eff} are in qualitative agreement with Manz [90]. However, we obtained higher rotational barriers along with larger energy separation between states; these indicate stronger crystal-field strength in our case, which must be attributed to different pair-potentials.

For the fixed lattice method, where relaxation was done for the minimum at $\theta = 0°$ orientation, the rotational motion was reduced to libration and the ground state $n = 0$ coalesced into a single state. Also the transition energy to the next state increased substantially in accord with a harmonic, orientational oscillation of the molecular axis. Contrary to the adiabatic result, no thermal excitations occur in the temperature range considered.

The transitions between the states in the ground librational manifold show a triplet in Raman and a doublet in IR spectra, which arises from the rotational transition rules for a diatomic. This is demonstrated in Fig. 3.1. The fixed lattice approach (top panel) gives a single band at band origin with no change in intensity over the temperature range. In the adiabatic approach (middle panel), the bands may lose intensity, which results in observable broadening of the bands. Then the stable sharp band B in Raman spectra is due to allowed transitions of $\Delta J = 0$ type between librational states. In infrared spectroscopy, the intensity of the center band B is redistributed to the side bands which correspond to the allowed $\Delta J = \pm 1$ type transitions. The reasoning behind the chosen two methods is that at low temperatures the fixed lattice approach becomes more suitable owing to the smaller amplitude motion of the lattice atoms. After raising the temperature, reorientations become allowed (adiabatic model) due

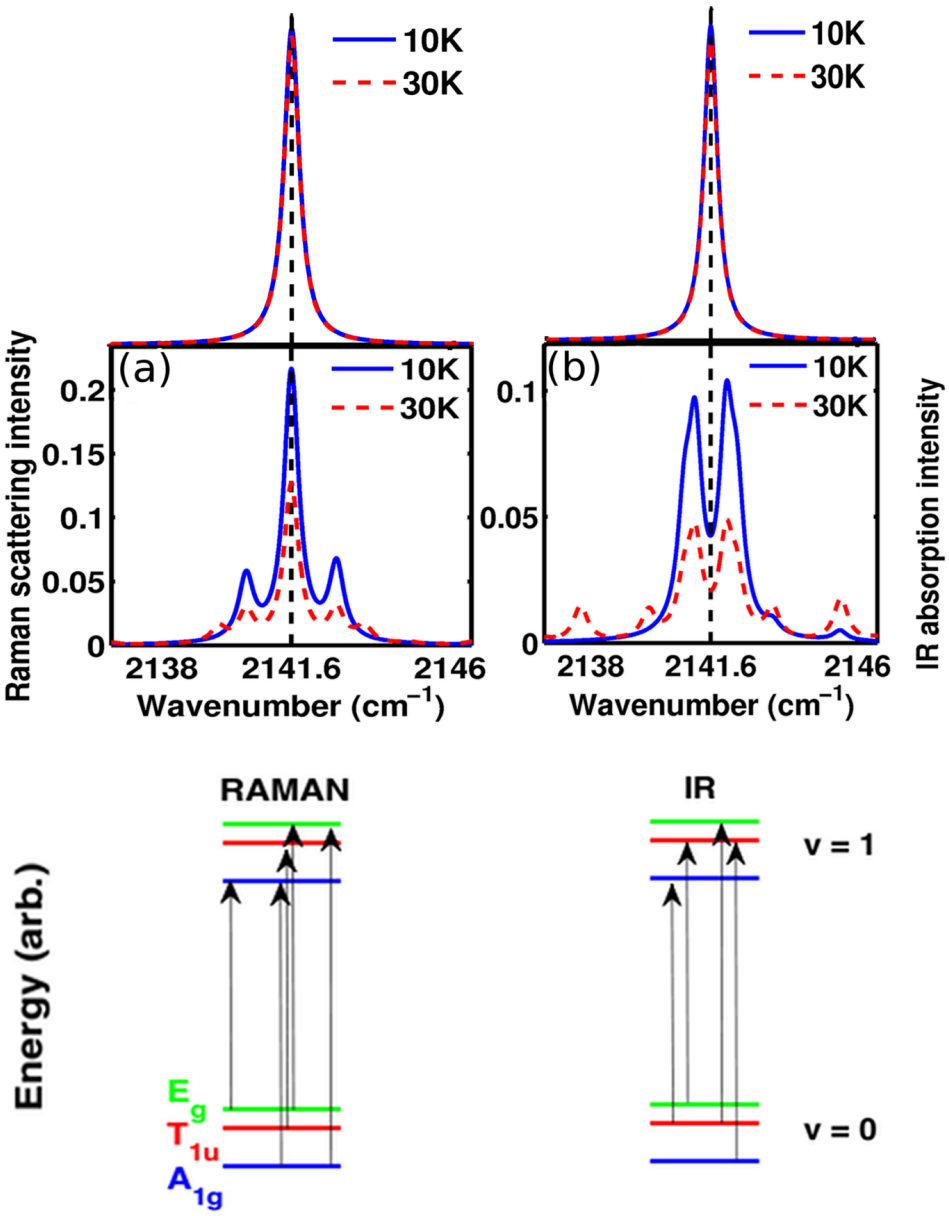

Figure 3.1: The effect of different angular momentum selection rules on (a) Raman and (b) IR spectra of CO in Ar. Top: the fixed lattice case, where the band origins do not change from the 2141.6 cm^{-1} and the spectra show only a single band at the fundamental vibration region. Middle: the adiabatic case, where the central band widths broaden as the higher librational states become populated at elevated temperatures. Bottom: schematic representation of the $n = 0$ librational states and the transitions to the excited vibrational state. In (a), the $\Delta J = 0$ creates a Q-branch type center band which loses some intensity after annealing. In (b), the Q-branch does not appear and the IR bands broaden rapidly.

to increased movement of the host atoms, thus providing more space around the molecule. The physical picture offers an explanation only for the band B, the stable band A must be considered separately.

The DS site has a nearest argon removed and the molecular axis prefers to be aligned along the cavity axis. The adiabatic potential shows two minima, both with respect to the vacancy $\times$: a global minimum which corresponds to OC$\cdots\times$ orientation and a local minimum which corresponds to CO$\cdots\times$. The pseudorotating lattice is not amenable here and $B_{\text{eff}} = B_0 = 1.92$ cm^{-1} is used in Eq. (2.28). The rotational motion reduces to libration and energy level structure consists of well-separated levels which are superpositions of $|JM\rangle$ states. The band origins are 2138.7 cm^{-1} and 2140.5 cm^{-1} for the OC$\cdots\times$ and CO$\cdots\times$ orientations, respectively, and the spectra show only a single band at those origins. The separation in energy is exactly the same as between bands A and B in the experiments. These configurations are considered to be stable with respect to annealing due to large separation between ground and excited librational states.

The results from the two cases, SS and DS, can now be summarized to give a qualitative assignment. The band A, at 2136.5 cm^{-1}, corresponds to monomeric CO in a DS site where the carbon end points toward the vacancy. The stability is explained by poor coupling to the lattice phonons. The band B at 2138.3 cm^{-1}, on the other hand, is understood to originate from two lattice geometries: the DS site with orientation CO$\cdots\times$ and from SS site where the rotation is hindered but not restricted to small-amplitude motion.

However, the band origins have to be shifted by different amounts for the SS and DS sites in order to match with the experimental positions. Also, the side bands from the Raman triplet in SS would coincide with bands A and C. Stronger crystal-field strength would scale the energetics to a more favourable direction, thus reducing the splitting, but to be consistent with the model presented, a broadening of the side bands is given as an explanation of not seeing them. Regarding the band origins, quantum chemical calculations support the interpretation that the fundamental vibrational transition coincides with the CO$\cdots\times$ orientation and the single-substitution site, making the bands to accidentally overlap.

Our interpretation should be contrasted with the "cluster" and "crystal" configuration model defined in Ref. [86], where the line shape calculations with vibration-translation coupling (VTC) scheme pointed to DS site as the dominant trapping geometry. This was consistent with their experimental IR results. The same model cannot be used here as the Raman spectra do not show the same line broadening. The model was tested but the band shapes were similar in both spectroscopies.

3.1.2 The hindered rotation of an isolated photoproduct H_2

Two trapping sites were considered for the H_2 molecule: a single-substitution (SS) and an interstitial site (O) of octahedral symmetry [II]. CO was removed from the simulation box. The isolated H_2 molecule rotates almost freely in SS and O sites as indicated by the low rotational barriers in the potential surfaces. In the SS site, the crystal-field splitting is nominal and rotational transitions $J : 2 \leftarrow 0$ and $J : 3 \leftarrow 1$ are observed as single bands. In the octahedral site the crystal-field strength increases which results in lifting of the degeneracy of $J = 2$ and $J = 3$ manifolds. The $J = 2$ state is split into a T_{2g} and E_g-doublet and the $J = 3$ becomes a A_{2u}, T_{2u}, T_{1u}-triplet.

The Raman spectra for matrix-isolated H_2 in Ar are shown Fig. 3.2. The experimental spectra are from the photolyzed sample at 10 K and the simulated spectra originate from the two lattice sites. Also Lorentzian fits to the experimental spectra are shown. The experimental values of $B_{\text{eff}} = 57.89$ cm^{-1} and $D_{\text{eff}} = 0.0046$ cm^{-1} were deduced from the sharp, center bands and used in Eq. (2.29). It can be seen that the isolated H_2 in substitution and interstitial sites explain quite well the observed spectral fingerprints even though CO molecules are generated in the sample. However, as the fit shows, more pronounced splitting of the $J = 3$ state is required in order to get perfect agreement with the experiments. This would require a larger crystal-field strength.

3.1.3 The question of intermolecular complex CO-H_2

As stated above, the photoproduct spectra can be explained by considering the rotation of both CO and H_2 in argon as if they were the single dopants [I,II]. For consistency, we considered the emergence of CO-H_2 complex and the effect on the spectra in Publication II. Four trapping sites for the hydrogen were chosen relative to molecular CO at the origin. These included the nearest-neighbor configuration, substitution sites at different locations in the unit cell, and an interstitial site of octahedral symmetry (same as the site O). The addition of CO as nearest-neighbor results in more pronounced splitting. For pH$_2$, the excited state $J = 2$ was split further into five states of varying composition. Similarly, the degeneracy of the $J = 3$ state was completely lifted and resulted in splitting to seven states. The ground states were considerably higher and for oH$_2$ the ground state T_{1u} ($J = 1$) was split into doublet. The Raman spectra had distinct sharp bands whose positions were not consistent with the experiments. In the furthest position considered, the rotational spectrum showed a single band as in the case of isolated H_2 in single-substitution site. The Raman spectra from other sites showed split band structure and the structure of the energy levels varied from case to case. The intermolecular complex where CO and H_2 take lattice positions nearest to each other cannot be responsible for the observed splitting due to discrepancy between simulation and experiments. The other configurations, where

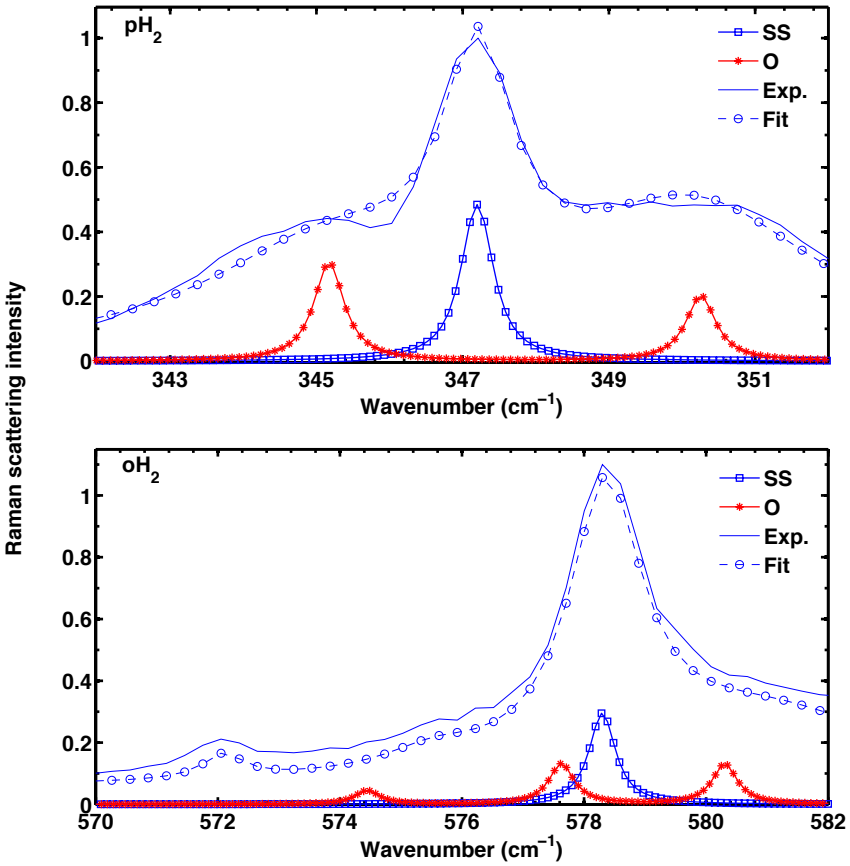

Figure 3.2: Simulated rotational Raman spectra for matrix-isolated H_2 in argon. The calculated spectrum consists of transition frequencies originating from substitution (SS, squares) and octahedral (O, asterisks) sites. The experimental spectra (solid blue line) are taken at 10 K after annealing to 30 K. A Lorentzian line shape (circles) was fitted to the experimental signals. The line shape fit was done in the pH$_2$ case by only adjusting the widths and intensities of the transitions, not the positions (wavenumbers).

CO and H_2 are at least a lattice constant away from each other, cannot entirely be ruled out.

The hydrogen had a similar impact on the rotation level structure of CO, namely that the degeneracies were further lifted from the isolated situation. The nearest-neighbor case is similar to the DS case considered earlier with calculated band origins at 2139.1 cm^{-1} ($OC\cdots H_2$) and 2141.5 cm^{-1} ($CO\cdots H_2$). However, the CO-H_2 pair-potential did not depend on the bond length of CO and the band origins are just an estimate. The splitting and the level composition varied in the other locations as the symmetry of the lattice is broken by the molecular hydrogen. This was observed to be independent on the chosen distances between the molecules; instead, it is the influence which the hydrogen has on the nearest argon atoms to CO. As was mentioned above, the experimental fundamental transition can be explained by considering the rotation of CO to be unaffected by the molecular hydrogen. The calculated spectra for the complexed case do not differ much from the isolated case, although the splitting increases; this could be balanced by the increased population in higher librational states which results in broadening of the side bands.

After the photodissociation, the fragments receive the excess energy. If the dissociation occurs via the molecular channel, most of the energy goes to the kinetic energy of the fragments. Therefore, one expects a ballistic trajectory leading to a cage exit of the molecular species. However, the EPR spectroscopy performed on the same system [66] showed an increase of atomic hydrogen as more energy was put into the dissociation. The low photon count in our case indicates a low yield for the radical products. It is also possible in practice that the H atoms form molecular hydrogen by abstraction of H from the radical HCO. The molecular CO can also originate from the HCO after photon absorption. A delayed cage exit of newly formed molecular hydrogen could then, at least in principle, lead to the separation between CO and H_2 fragments. Our hypothesis is that the molecular fragments undergo a cage exit, either direct or delayed, and the subsequent thermalization of the matrix does not lead to complex formation as the rotational zero-point energy within the complex becomes too high. A more thorough investigation of the photodissociation in the H_2CO/Ar system seems to be in order, including systematic monitoring of the molecular photofragment production as a function of incident photon count accompanied by e.g. semi-classical trajectory simulations.

3.2 Electronic coherence and local geometry of I_2 in crystalline Xe

In Publication III, the work on I_2 matrix-isolated in Xe was motivated by the observation of vibronic structure in the $B \leftrightarrow X$ absorption spectra in Ref. [115]. The purpose was to elaborate on the dephasing time T_2 in the upper state, approximated to be 600 fs on average as deduced from the absorption line widths. Additionally, the energy level structure and dynamics of matrix-isolated I_2 was probed by TR-CARS to complement the RR spectroscopy.

Experimentally, after 532 nm excitation, a bimodal line progression in the RR spectra was observed. The major component was a sharp line progression, accompanied on the blue side by a minor, broader progression line. The overtone transitions were resolved up to $\nu = 18$ and $\nu = 8$, respectively. As was mentioned in Sec. 2.5.1, the width of the progression lines reflect the ground state dynamics in so far as the line widths are not masked by the instrumentation. Due to the instrumental limitations, the resonance Raman progression intensity profile I_{RR} [Eq. (2.50)] is not calculated. Instead, the Raman cross section in Eq. (2.51) is used to compare with the experimental intensities. The time-resolved femtosecond CARS spectroscopy was used to probe the ground vibrational states. The pump-dump pulse pair was chosen to sample either the low-ν or high-ν energy regions of the ground state potential by adjusting the Stokes shift. By scanning the time interval τ_{32}, the beat frequencies $\omega_{jj'}$ in Eq. (2.59) for the two cases were assigned according to vibrational energy level composition. In the case of low-ν packet, the fundamental frequency at 201.2 cm^{-1} was assigned to beat between ν =7-8 states, addionally an overtone beat at 399.7 cm^{-1} was observed. For the high-ν, the fundamental beat at 190.1 cm^{-1} was assigned to ν =14-15 Stokes packet and similarly an overtone at 380.8 cm^{-1} appeared.

The modeling of resonance Raman and time-resolved CARS measurements was done to answer mainly to the following questions: (1) What is the physical origin for the bimodal Raman line progression? (2) what is the coherence-decay time in the B-state after excitation at 532 nm? The answer to question (1) comes from the molecular dynamics simulations which also provided the adiabatic potentials for the propagation of the vibrational wavepackets. Three lattice geometries for the Xe-trapped iodine was considered: a single-substitution (SS), double-substitution (DS), and triple-substitution (TS) site. Also a comparison fcc vs. hcp stacking was made in order to explain the RR intensity profile, but both gave similar spectral results. The fcc-type lattice, with above vacancies, was chosen.

In the SS case, averaged potential curves gave blue-shifted vibrational states, indicating a trapping geometry too tight to be physical. The vibrational energies showed large discrepancy with the experiments and the case was dropped from subsequent

numerical treatments.

Similar to the case considered in Sec. 3.1.1 for CO, the DS site reduces the rotations to librations. The molecular axis of iodine becomes oriented along the cavity axis with average angular displacement below five degrees. A net attractive interaction between the I_2 and axial Xe atoms leads to red-shifted vibrational energies from the gas phase. The line width simulations gave a narrow distribution of frequencies and indicated a sharp line shape for the Raman progression.

An additional vacancy was introduced nearest to I_2 in DS site. Four positions were considered and the position where reorientations of the molecule occurred was taken under more detailed inspection. The TS configuration, derived from the DS cavity, corresponds to geometry where an additional Xe atom was removed perpendicular to vacancy axis. The other three sites gave rather similar results to the DS case. The attractive interaction with axial atoms is partly lost as the molecular axis samples the larger void, which results in less red-shifted energies compared to the orientationally locked situation (DS). Additionally, MD-based line width analysis points to broadened frequency distribution which is due to the induced reorientations. The molecular dynamics approach to dephasing gave also faster decay times for the TS trapping configuration than for the DS configuration.

The MD results indicate clearly that the two Raman progression lines originate from different local trapping geometries. The sharp line progression originates from the double-substitution site where the cavity restricts the rotational motion. The minor progression arises from the triple-substitution site where the rotational-translational dynamics coupled with increasing vibrational motion broadens the spectral lines.

3.2.1 The electronic dephasing time between B and X electronic states

Considering question (2), resonance Raman simulations were done to elaborate on the coherence-time. The large uncertainty in the experimental RR intensities led us to consider only the sharp progression lines. The task is two-fold here: (i) compare the dynamics between MD-averaged potential and experimental Morse potential; (ii) find the coherence-decay time either using a Gaussian (σ) or exponential (T_2) dephasing function. The task (ii) is accomplished by fitting to the experimental intensities with a trial-and-error type approach.

Regarding task (i), the experimental Morse potential did not give satisfactory agreement with the oscillatory pattern in the intensity profile and the best fits gave coherence times $\sigma = 250$ fs and $T_2 = 170$ fs. The reason is that at higher energies the cage-induced bent potentials deviate more drastically from the gas phase situation and

the Morse shape becomes increasingly inadequate when higher states are involved in the wavepacket. The experimentally estimated electronic energy origin $T_e = 15212$ cm^{-1} for the B-state can be used, though [115].

The essential part concerning task (ii) is shown in Fig. 3.3, where a comparison between the experimental and numerical results is made for Gaussian decay with time constants σ =120, 235, and 350 fs. The oscillatory pattern did not deviate significantly when exponential decay function was used. The best-fit in this case was gained by putting $T_2 = 150$ fs. The Raman wavefunctions in the inset of Fig. 3.3 were produced in the manner described in Sec. 2.5.1. The intensity profile in the main panel of Fig. 3.3 was obtained as squared overlap between the $|R_{\omega_I}\rangle$ and vibrational states $|\psi_f\rangle$ in the X-state in accord with Eqs. (2.47) and (2.51).

The intensity modulation is a monotonically decaying function of the overtone in the faster decay ($\sigma = 120$ fs). Correspondingly, any recurrences in the Raman wavefunction are damped. In the slow decay case ($\sigma = 350$ fs), the long-lived coherence manifests in the Raman as the strong oscillatory intensity pattern. The best-fit is between these two limits; it has the intensity variation peculiar to the long-time limit, but begins to approach the monotonical case of short-time dynamics. An odd-even intensity modulation is seen, where the terminal even-states gain intensity when the dephasing time increases. The odd-even pattern was studied numerically by tuning the laser frequency over some doorway-states on the upper surface. At exact resonance, the Raman wavefunction is real and resembles a vibrational eigenstate on the B-surface. The interaction with the Xe-wall must induce a 0° phase-shift as the packet retains the memory of the parity and the even-states gain intensity. When the laser hits between vibrational resonances, the Raman wavefunction obtains an imaginary component and cannot represent an eigenstate. In this case, the odd-even pattern reverses: the intensity of terminal even-states lose intensity and drops below the smooth curve whereas for the odd-states the intensity remains intact.

As the outcome of the experiments and simulations, we show that the electronic coherence between the X and B survives for over half vibrational period, surpassing the coherence-time previously observed in Kr and Ar. The long vibrational coherence times in Xe has been attributed to the high symmetry of the cage [149]. However, the electronic coherence surpassing the initial collision with Xe atoms is a new and somewhat surprising result. We did not explicitly calculate the multidimensional correlation function which introduces, in a natural way, the bath correlation decay that ultimately quenches the RR signal [150]. The correlation function could be calculated, for example, by semi-classical trajectory simulations [151–153] or quantum/classical simulations [122]. In the present scheme, the correlation function can be considered to be separated to the chromophore and bath parts, and Gaussian or exponential function serving as the bath correlation function decay.

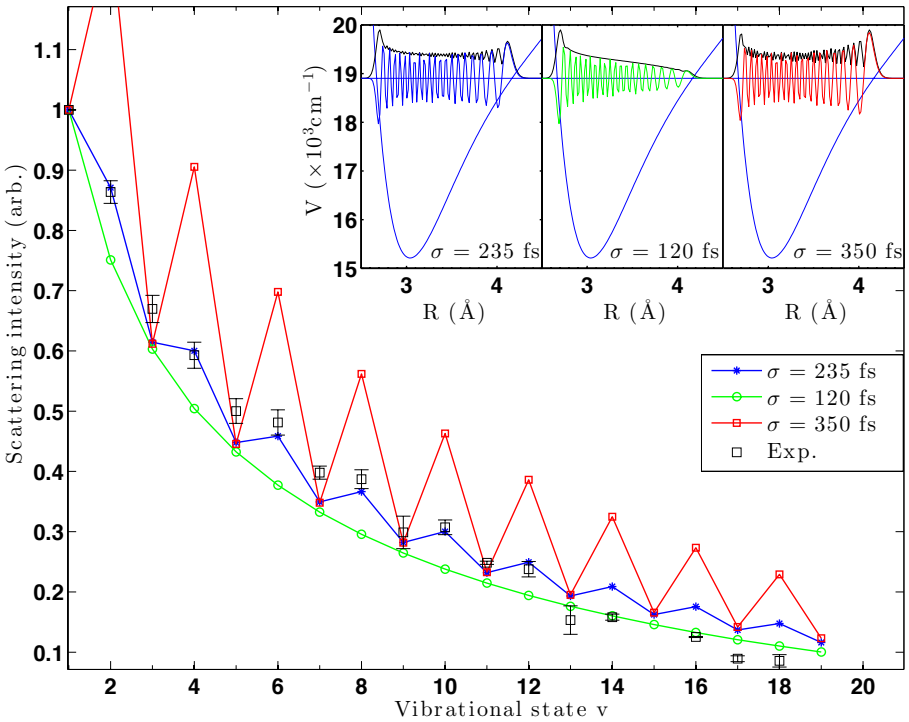

Figure 3.3: Main panel: the comparison between experiments (squares) and the three Raman progression lines with dephasing times 120 fs (green, circle), 235 fs (blue, star), and 350 fs (red, square) for the $|R_{\omega_I}\rangle$. The error bars in the experimental intensity indicate the fit uncertainty. Insets: absolute (black) and real parts of the accumulated Raman wavefunction for the three cases. Unpublished work copyright © 2013 American Chemical Society.

3.2.2 Time- and frequency-resolved CARS probing of coherences

The vibrational state structure of the electronic ground potential was investigated by adjusting the Stokes shift; the wavelength (nm) combinations (pump/dump/probe) 580/635/560 and 558.2/668.7/605.2 for the low-ν and high-ν were used, respectively. Pulse durations were in the 60-90 fs range. The same electronic coherence-decay times as for the RR case were used in the calculation of third-order polarization and the integration time was adjusted accordingly. The time-resolved CARS interrogates the second-order coherences, namely the vibrational coherences in the ground electronic state when the probe delay time τ_{32} is scanned. The pump and dump pulses coincided temporally ($\tau_{21} \simeq 0$ fs). In order to qualitatively reproduce the decay of the experimental time traces, the CARS signal was multiplied by an exponential decay function with dephasing times of 6 ps and 24 ps for the high and low vibrational wavepackets in the X-state.

The numerical beat frequencies for the fundamentals were in almost perfect agreement with experimental ones and can be reliably assigned to quantum beats ν =7-8 (low-ν) and ν =14-15 (high-ν). The overtone beats showed some deviation from the experiments, computed average from the 14-16 or 15-17 levels matches the experimental overtone beat for the high-ν case. Similarly, in the low-ν case, the average of 7-9 and 8-10 beats corresponded with the experimental overtone beat. A change in the $X \leftrightarrow B$ electronic coherence-time did not affect the beat frequencies. Test runs with probe wavelength matching the 532 nm resonance Raman excitation were done and the spectrum was not affected by the coherence-decay time.

A complementary view to the absorption measurements is shown in Fig. 3.4, which was generated numerically by scanning both time delays τ_{21} and τ_{32}, resulting in a two-dimensional signal in the time-domain. The pump wavelength (580 nm) coincides with the absorption maximum and the dump wavelength corresponds to ν =7-8 wavepacket. The time trace shows that by using the experimental average dephasing time of T_2=600 fs, the first-order electronic coherence persists up to 1.6 ps. This is consistent with the decay of correlation function $C(t)$, which was obtained after a Fourier transform of the resolved part of the absorption spectrum. In Publication III, an additional computational approach to TIFRCARS [Eq. (2.60)] was performed by taking Fourier transform along the τ_{32} domain of the time-integrated signal. The best-fit cases, $T_2 = 150$ fs or $\sigma = 235$ fs, did not fully resolve the beating between branches and resulted in a broad fundamental band in the two-dimensional frequency image. The compromised frequency resolution can explain the additional, smaller features in the Fourier transform of experimental time-resolved CARS signals.

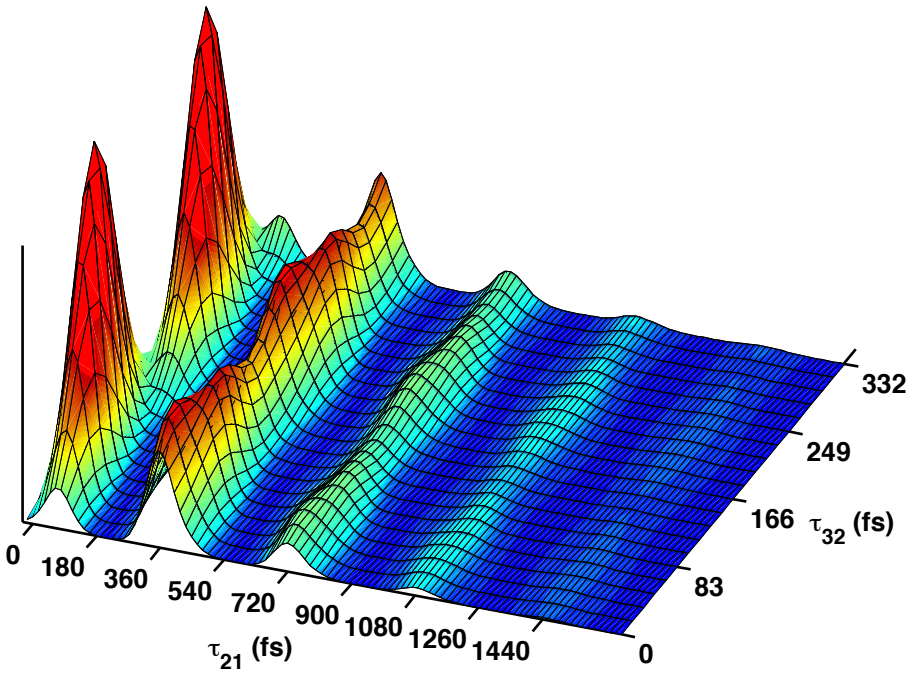

Figure 3.4: A 2D, time-domain (τ_{21} vs. τ_{32}) represention of CARS signal. The dynamics in the B-state is observed through the oscillation in the τ_{21} domain. The pattern becomes completely damped after 1.6 ps when time constant $T_2 = 600$ fs is used.

3.3 Imaging of rovibronic coherences of CN

The time-integrated interferogram [Eq. (2.60)] is shown in Fig. 3.5. At the chosen temperature of 10 K, $J = 1$ is the most populated state ($\sim 50\%$). The transition frequencies between final f and initial i states are given relative to the vibronic transition origin $\omega_0 = 27922$ cm^{-1}. The time delay τ_{21} was fixed arbitrarily to 200 fs as the first-order coherences were not interrogated. The pump-probe delay time τ_{32} extends to 15 ps, no decay is introduced during this period, and the third-order polarization was integrated up to 40 ps. Pulse durations (FWHM) of 50 fs were used and the pump, dump, and probe center frequencies were 388 nm, 423 nm, and 388 nm, respectively.

The R- and P-branches appear at the difference frequencies ω_{fi}, where the index f includes the $N_i + 1$ and $N_i - 1$ rotational states in the upper electronic state B, respectively. The branches $R(N_i)$ and $P(N_i)$ are assigned according to the initial rotational state N_i and are located in the shifted energy axis at wavenumbers

$$\omega_R = 2B_{1,B} + N_i(3B_{1,B} - B_{0,X}) + N_i^2(B_{1,B} - B_{0,X}) \tag{3.1}$$

$$\omega_P = \quad -N_i(B_{1,B} - B_{0,X}) + N_i^2(B_{1,B} - B_{0,X}) \quad (N_i > 1)\,, \tag{3.2}$$

where $B_{1,B} = 1.9356$ cm^{-1} and $B_{0,X} = 1.8901$ cm^{-1} are the rotational constants. The subscripts indicate the vibrational quantum number and the electronic state.

In Fig. 3.5, the beating within a branch in TIFR image reveals the second-order coherences as the time interval τ_{32} is scanned. These include quantum and polarization beats where the latter is negligible compared to the former if the third-order polarization has a long lifetime [127]. Here, the large empirical parameter $\Gamma = 0.1$ ps^{-1} (Ref. [140]) dictates that the polarization beats are overwhelmed by the quantum beats, which in the R-and P-branches have oscillation frequencies:

$$\omega_R^{(i)} = B_{1,X}(4N_i + 6) \tag{3.3}$$

$$\omega_P^{(i)} \overset{N_i>1}{=} B_{1,X}(4N_i - 2)\,, \tag{3.4}$$

where the $B_{1,X} = 1.873$ cm^{-1}. The R- and P-branches are also spectrally resolved due to the large decay constant. By shortening the decay time the spectral resolution is lost as the intermolecular interference (polarization beats) emerge.

By choosing the delay time, a control over the emission intensity can achieved. For example, as marked in Fig. 3.5 by dashed and dotted lines, the intensity pattern in the CARS beam can be tuned from nominal (dashed line) to maximum (dotted) value by changing the time delay from 4.45 ps to 8.90 ps. Therefore, the information encoded in the TIFR image can be used to switch the dominant branch in time-gated detection methods and/or to switch off a branch altogether.

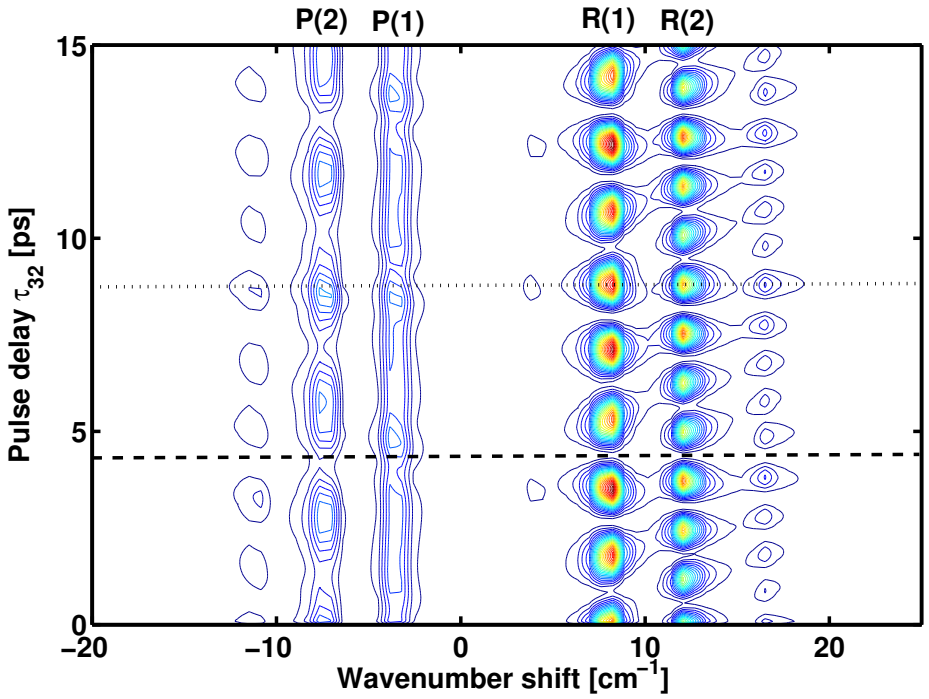

Figure 3.5: The two-dimensional time-integrated frequency-resolved CARS image for CN at 10 K. Thermal population has a maximum at $J = 1$ and the branches $R(1)$ and $R(2)$ are the main spectral components. The oscillation period is 1.78 ps in $R(1)$ and 1.27 ps in $R(2)$. The $P(1)$ branch amplitude should be unaffected by the time delay τ_{32}, but the adjacent $P(2)$ is not completely resolved and modulates the spectral intensity by interference. The wavepacket is completely dephased at 4.45 ps (dashed line) but rephases again at the full revival time $(2cB_{1,X})^{-1} = 8.90$ ps (dotted line).

The Husimi transform of the anti-Stokes radiation beam is shown in Fig. 3.6, which represents the two-dimensional time-gated frequency-resolved CARS image. The spectrograph is constructed for a measurement with intervals $\tau_{21} = \tau_{32} = 200$ fs. Here, the rotational temperature is set to 30 K in order to include states $N_i = 0-6$ in initial distribution. The beatings in the radiation beam show up during the time interval T with frequencies $\omega_{fi} - \omega_{f'i'}$. This leads to the intra- (ω_{RR} and ω_{PP}) and interbranch (ω_{RP}) polarization beating along with intramolecular (quantum beats) difference frequencies $\omega_{\mathrm{RP}}^{i=i'}$. An exact result for the observable frequencies can be found in Publication IV.

In Fig. 3.6, the Kerr gate delay extends to 35 ps and the gate width is either (a) 500 fs or (b) 3 ps. The motivation for the chosen widths is to demonstrate the imaging and control of rotational coherences by utilizing the length of the time slice (gate width). In case (a), the interference beats ω_{RP} occur alongside with the intrabranch beat wavenumbers ω_{RR} and ω_{PP} which have an average period of 8.7 ps. With gate width of 3 ps (case b), the interbranch beatings are seen to be washed out and only the interference within the branch is observed at multiples of $(2cB)^{-1}$. This is similar to alignment dynamics where the least common multiple of the frequencies governs the periodicity T_{rev} in the rotational wavepacket.

The nodal patterns in the spectra obtained via the time-integrated mode can be utilized in the time-gated detection. The spectral components or branches are suppressed or enhanced by carefully choosing the time delay. Although we only discussed the dump-probe delay time, the approach is amenable to manipulation of first-order coherence images as well. These offer a control scheme for the detection of rotational coherence in CN. It must be pointed out that the control extends only to the imaging of the third-order coherence as the populations in the Stokes packet are not affected.

Detailed knowledge about the difference frequencies accumulated after scanning τ_{32} and the detection of the interferences is obtained within the present theoretical framework. So far, CARS spectroscopy on the CN radical embedded in solid Xe has not been realized experimentally. Therefore, the test of the validity must await for a future comparison. The parameters were chosen such that the comparison is feasible. Schallmoser *et al.* [140] noticed the emergence of Q-branch in solid Xe environment. If this is the case in general, the CARS interferograms show more complicated oscillation patterns within the branches and the $Q(N_i)$-branch at zero frequency in the shifted scale would emerge in high-resolution images.

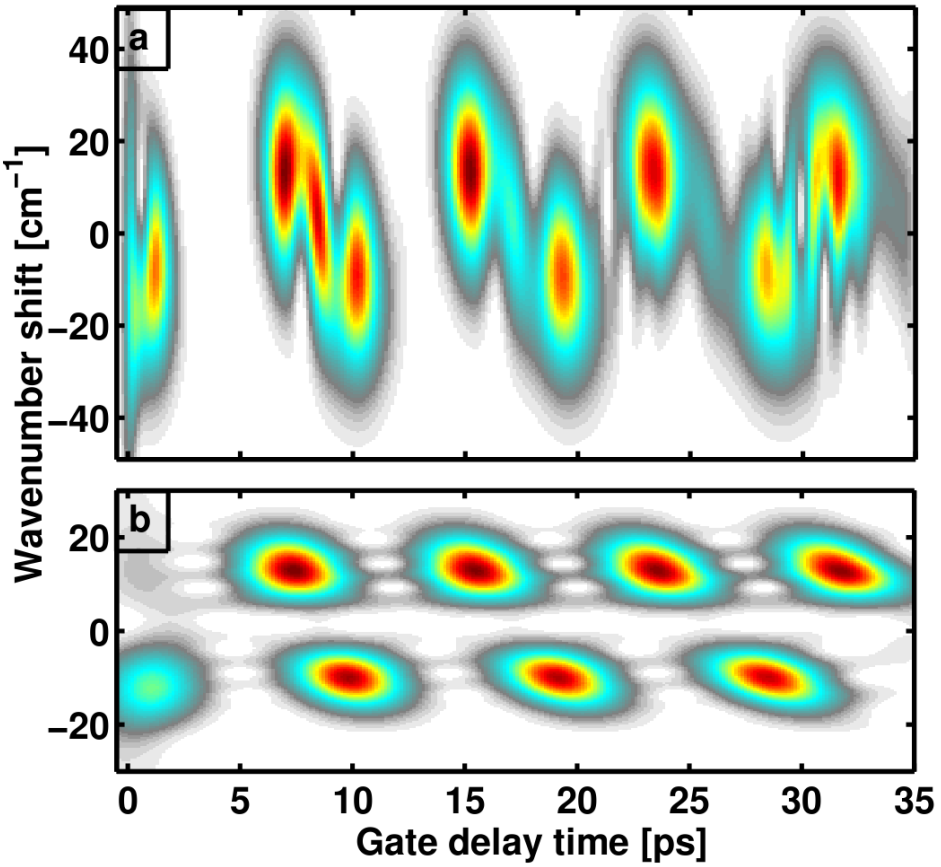

Figure 3.6: The time-gated frequency-resolved CARS interferograms for gate widths (a) 500 fs and (b) 3 ps. The temperature is set to 30 K and the initially populated states are $N_i = 0 - 6$ and the maximum of Boltzmann distribution corresponds to $N_i = 3$ state. The energies are given again relative to the vibronic origin 27922 cm^{-1}. (a) Sweeping over a short time slice of the third-order polarization compromises the spectral resolution and shows the oscillation pattern between branches in the time-domain. (b) Long time slices (compared to oscillation period between the branches) resolve the signal spectrally into R- and P-branches and the interbranch beatings disappear. The intrabranch (polarization) beating is now dominant in the spectrogram.

3.4 Molecular alignment in para-hydrogen

The optical Kerr effect spectroscopy applied to gaseous $p\mathrm{H}_2$ showed spectral and temporal signatures which were straightforward to interpret. In the gas phase, the rotational states are not split and the transition to excited $J = 2$ states is at 354.3 cm^{-1} corresponding to an oscillation period of 94 fs in the time-domain signal [54]. The effects of pulse duration on rotational excitation and the alignment degree was studied. These were compared with nitrogen which shows a revival time of 8.4 ps along with fractional revivals. The simulations yielded the range of pulse durations which correspond to field-free alignment and showed that the adiabatic regime is approached at 120 fs long pulses. The effect of intensity of the laser pulse on the alignment degree was bypassed in Publication V, only a constant $I = 10$ TW/cm^2 was considered. Even at this intensity, the rotational excitation is limited to $J = 0, 2$ states with $J = 0$ dominating the composition as deduced from the small expectation value $\langle J^2 \rangle$.

In the case of solid $p\mathrm{H}_2$, a single pair of pulse parameters was chosen, namely 1 TW/cm^2 and 100 fs for the intensity and pulse duration, respectively. The pulse intensity is taken directly from the experiments, but the pulse duration is shorter than the experimentally obtained (166 fs). The crystal field splits the $J = 2$ manifold and Eq. (2.25) is used. In order to match the experimental frequencies 356.00 cm^{-1}, 353.99 cm^{-1}, and 351.98 cm^{-1} with simulations, the molecular parameters B_0, D_0, and Q_0 were scaled while keeping the lattice constant R_e at 3.783 Å. The fit values were: $B_0 = 59.32$ cm^{-1}, $D_0 = 0.0646$ cm^{-1}, and $Q_0 = 0.4352$ a.u.

The control over the components in the roton wavepacket can be achieved by choosing the angle θ' between pump polarization and crystal c-axis. The M-state distribution ($|c_{2|M|}|^2$) is shown Fig. 3.7. The angle $\theta' = 77°$ (broken red line) is chosen as it reproduces qualitatively the experimental features. With this choice, all the $|M|$-split states of the $J = 2$ manifold have considerable weights. Of course, suppressing certain transition frequencies is possible as well. For example, $\theta' = 54°$ choice would make the contribution from $M = 0$ state to be nominal. Experimentally, the choice could be done by varying the pump beam spot along the cylindrical sample.

The Euler angle χ' affects the way the roton wavepacket composition emerges. The angle was defined in Fig. 2.6 and relates to the orientation of the crystal axes x, y to the pump beam propagation direction Y and to the XZ surface. In the crystalline sample, these directions can change from crystallite to crystallite. However, a signal from a single crystallite was most likely obtained during the measurements and a orientation of $\chi' = 20°$ was chosen to reproduce the experimental trace.

The numerical OKE signal is presented in Fig. 3.8 for $\theta' = 77°$ and $\chi' = 20°$. The probe duration was 130 fs and a dephasing time of 90 ps for the alignment was introduced

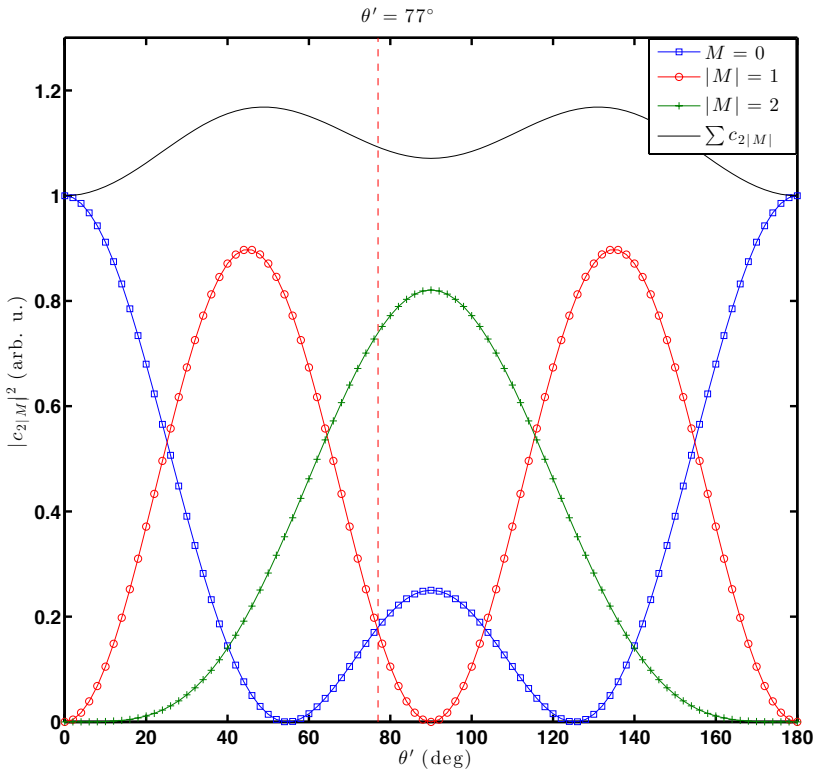

Figure 3.7: The square of the coefficients $c_{2|M|}$ in the roton wavepacket. The angle θ' is the angle between polarization direction of the pump and the hexagonal c-axis. The other relevant Euler angle χ' does not affect the weights $|c_{2|M|}|^2$. The vertical, red broken line indicates the choice of $\theta' = 77°$ to reproduce the pump-probe OKE signal.

as mentioned in Sec. 2.5.3. The intensity calculation follows Eq. (2.68).

The time trace in Fig. 3.8 (a) shows the heterodyne intensity modulation on top of the homodyne part and has an oscillation period of 94 fs (inset). This period is an average period of oscillation between the split $|M|$-states and initial $J = 0$ state. The slow beats of 17 and 8 ps belong to the homodyne part and match the difference frequencies 2 cm^{-1} and 4 cm^{-1}, respectively. The dephasing is twice as fast for the homodyne part and at longer times the heterodyne intensity becomes of comparable strength (not shown).

The frequency spectrum in (b), taken from the signal in (a), shows three high frequency beats at 352 cm^{-1}, 354 cm^{-1}, and 356 cm^{-1} for $|M| = 1, 2, 0$, respectively. The transition frequencies originate from the heterodyne part of the signal, I_{het}. On the other hand, the homodyne intensity part has the low frequency beats or difference frequencies 4 cm^{-1} and 2 cm^{-1}; shown in the inset of (b) are the energy separations between the crystal-field split $|M|$-states.

The molecular alignment was extended to the condensed phase in Publication V and a good agreement with the experimental time trace was obtained. The emphasis was put on the spatial (control) aspect of the experiments, namely on the orientational dependence θ', χ', and this originates from the geometry of the experimental setup. Difficulties in the comparison arise due to the aforementioned geometrical considerations and a correct angular parameter space is hard to determine. The experimental Fourier transform show larger $|M| = 1$ contribution to the signal than what the simulations with the chosen angles give. The experimentally dispersed, two-dimensional OKE signals showed in some occasions different dynamics in Stokes- and anti-Stokes branches [54], but the present simulations cannot give a definite mechanism for this observation, and the two-dimensional signal is left for future considerations.

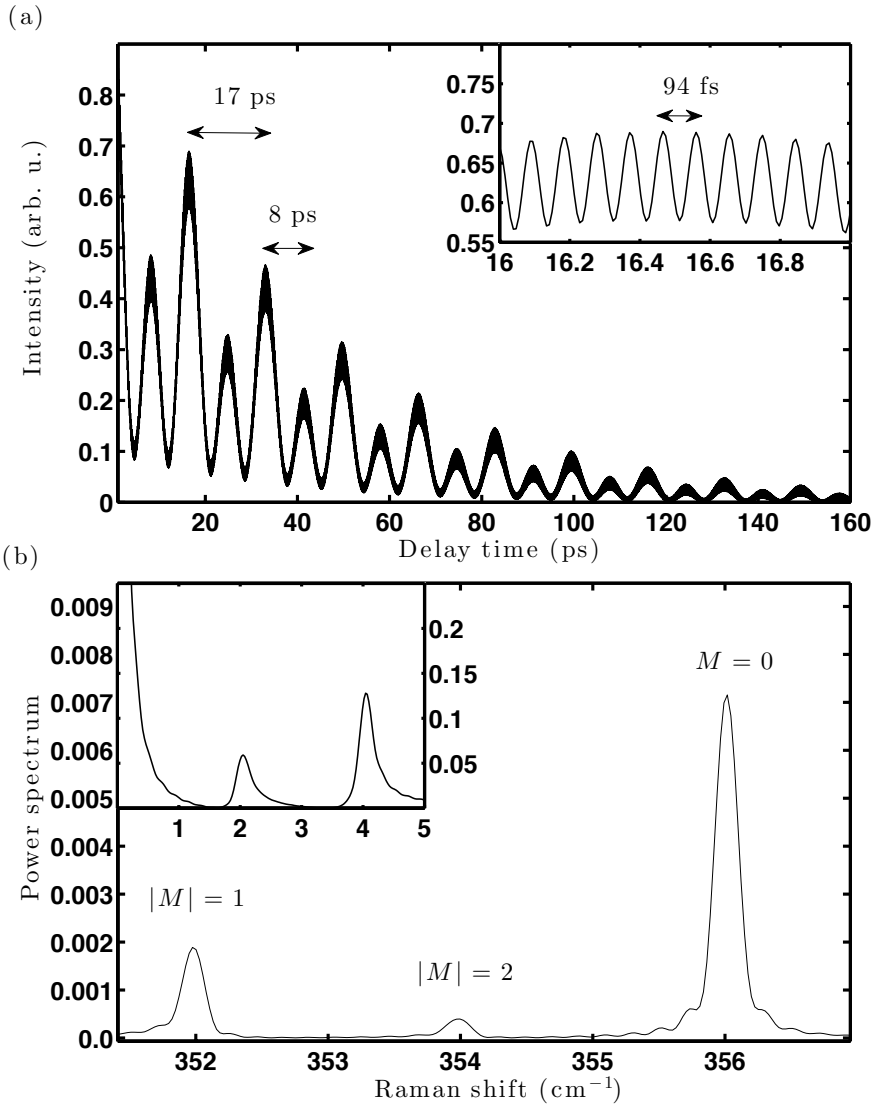

Figure 3.8: (a) The calculated OKE signal exhibiting the difference frequencies in the roton wavepacket when $\theta' = 77°$ and $\chi' = 20°$. In the inset is the 94 fs oscillation period in the wavepacket corresponding to transition $J : 2 \leftarrow 0$. (b) Fourier transform of the time trace showing the spectral density resolved for the indicated $|M|$-states. These correspond to the transition energies between $J = 0$ and $|M| = 1, 2, 0$ states respectively and arise from heterodyne intensity part. In the inset, the low frequency region shows the energy differences between the $|M|$-states. The sum combinations of the transition frequencies around 710 cm^{-1} are not shown.

4 Summary

The rotational and vibrational degrees of freedom of diatomic molecules CN, I_2, CO, and H_2 in condensed phase were studied by different numerical methods. The emphasis was on the explanation of the spectroscopic signals, not choosing or developing a specific computational method. The electronic structure was not under scrutiny and the contribution from the electronic part was constructed from state-of-the-art intermolecular pair-potentials taken from literature. We used these for the quantum mechanical propagation of the wavepackets and to obtain the vibrational eigenstate space. The reproduction of experimental details has provided a demanding test of the accuracy of the potentials and simulated dynamics.

New insight on the photodynamics of formaldehyde was gained from the adiabatic rotation model. New spectral fingerprints were attributed to H_2 (ortho and para) rotating almost freely in single-substitution site and in a more hindered manner in interstitial sites. The rotational band structure of an intense center band accompanied by satellite bands arose from the rotational manifolds which are unequally split by the crystal-field in the two lattice configurations. No measurements on isolated H_2 in Ar were made, but in previous Raman spectra such splitting was not observed until at high concentrations of the dopant molecule.

The two-site model for CO in argon offers a clear indication that the molecule preferentially resides in double- and single-substitution sites. The main difference is the rotational hindrance: in DS site, the rotational motion reduces to libration, whereas in SS the rotation is weakly hindered. The thermally induced line broadening of the IR bands, contrary to the Raman case, was attributed to rotational selection rule concerning the Q-branch. The present observations and explanations for the band structure in the fundamental vibrational frequency region gives additional information on the much studied system and perhaps, more importantly, a renewed assignment for the most debated bands.

The electronic coherence, resolved as ZPLs and PSBs in the absorption spectra, was investigated through numerical wavepacket propagations in statistically averaged adiabatic potentials. The coherence-decay time was obtained by comparing the numerical data to experiments. The results indicate that the electronic coherence $|B\rangle\langle X|$ survives for a time interval longer than the half-vibrational period in the B-state. The lattice geometry around I_2 was given as the reason behind the double peaked progression in RR. The sharp line belongs to iodine fixed orientationally in the direction of

the vacancy and the broader, blue-shifted progression belongs to triple-substitution site which allows reorientations of the molecular axis.

Computational study of two-dimensional time- and frequency-resolved CARS imaging was done on the CN radical. The second- and third-order coherences were analyzed with the help of analytically obtained beat frequencies. The oscillatory patterns can be recognized with the help of the simulations; deviations from our results would indicate a weakly allowed Q-branch, for example in solid Xe. A control over the 2D images can be achieved by tuning the pulse delay and/or Kerr gate width, which was demonstrated through the interferograms. The model used is considered predictive and any deviations from it should be considered as indication of more complex physics, not as a failure of the model.

The experimental time trace for the pump-induced birefringence signal from solid para-hydrogen was qualitatively reproduced with nonadiabatic molecular alignment as the underlying mechanism. The alignment scheme was extended to the condensed phase by deriving analytical Hamiltonian which takes into consideration the geometrical aspects of the system. From the theory, it was recognized that the orientation between the crystal frame and laboratory frame could play a key role in the detection of reorientations and this was supported by the numerical simulations of the pump-probe optical Kerr effect signals. A control over the molecular orientation is realized by taking advantage of the relation between laser polarization and geometry of the solid sample.

References

[1] C. V. Raman and K. S. Krishnan. *A New Type of Secondary Radiation.* Nature **121**, 501 (1928).

[2] F. Combes and G. Pineau des Forets, editors. *Molecular Hydrogen in Space.* Cambridge University Press, Cambridge, UK (2000).

[3] V. G. Manzhelii and Y. A. Freiman, editors. *Physics of Cryocrystals.* AIP, Woodbury, New York (1997).

[4] G. Herzberg. *Molecular Spectra and Molecular Structure. I. Spectra of Diatomic Molecules.* Krieger Publishing Company, Malabar, Florida, 2nd edition (1950).

[5] J. Brown and A. Carrington. *Rotational Spectroscopy of Diatomic Molecules.* Cambridge University Press, Cambridge, UK (2003).

[6] W. A. de Jong, L. Visscher and W. C. Nieuwpoort. *Relativistic and correlated calculations on the ground, excited, and ionized states of iodine.* J. Chem. Phys. **107**, 9046 (1997).

[7] I. R. Dunkin. *Matrix-Isolation techniques – A Practical Approach.* Oxford University Press, New York (1988).

[8] V. E. Bondybey, A. M. Smith and J. Agreiter. *New Developments in Matrix Isolation Spectroscopy.* Chem. Rev. **96**, 2113 (1996).

[9] V. A. Apkarian and N. Schwentner. *Molecular Photodynamics in Rare Gas Solids.* Chem. Rev. **99**, 1481 (1999).

[10] L. Pauling. *The Formulas of Antimonic Acid and the Antimonates.* J. Am. Chem. Soc. **55**, 1895 (1933).

[11] R. B. Gerber. *Formation of Novel Rare-Gas Molecules in Low-Temperature Matrices.* Annu. Rev. Phys. Chem. **55**, 55 (2004).

[12] M. L. Klein and J. A. Venables, editors. *Rare Gas Solids.* Academic Press, London (1976).

[13] M. E. Fajardo, C. M. Lindsay and T. Momose. *Crystal field theory analysis of rovibrational spectra of carbon monoxide monomers isolated in solid parahydrogen.* J. Chem. Phys. **130**, 244508 (2009).

[14] F. Königsmann, M. Fushitani, N. Owschimikow, D. T. Anderson and N. Schwentner. *Femtosecond pump-probe 2D optical Kerr effect spectroscopy of molecular hydrogen crystals.* Chem. Phys. Lett. **458**, 303 (2008).

[15] T. Brixner and G. Gerber. *Quantum Control of Gas-Phase and Liquid-Phase Femtochemistry.* ChemPhysChem **4**, 418 (2003).

[16] M. Dantus and V. V. Lozovoy. *Experimental Coherent Laser Control of Physicochemical Processes.* Chem. Rev. **104**, 1813 (2004).

[17] P. Nuernberger, G. Vogt, T. Brixner and G. Gerber. *Femtosecond quantum control of molecular dynamics in the condensed phase.* Phys. Chem. Chem. Phys. **9**, 2470 (2007).

[18] J. C. Tully. *Perspective: Nonadiabatic dynamics theory.* J. Chem. Phys. **137**, 22A301 (2012).

[19] P. M. Morse. *Diatomic Molecules According to the Wave Mechanics. II. Vibrational Levels.* Phys. Rev. **34**, 57 (1929).

[20] M. Tinkham. *Group Theory and Quantum Mechanics.* McGraw-Hill Book Company, New York (1964).

[21] R. N. Zare. *Angular Momentum.* Wiley, New York (1988).

[22] J. T. Hougen. *The Calculation of Rotational Energy Levels and Rotational Line Intensities in Diatomic Molecules.* N. B. S. Monograph 115. Washington DC (1970).

[23] H. Lefebvre-Brion and R. W. Field. *Perturbations in the Spectra of Diatomic Molecules.* Academic Press, Orlando (1986).

[24] R. Meyer. *Trigonometric Interpolation Method for One-Dimensional Quantum-Mechanical Problems.* J. Chem. Phys. **52**, 2053 (1970).

[25] C. C. Marston and G. G. Balint-Kurti. *The Fourier grid Hamiltonian method for bound state eigenvalues and eigenfunctions.* J. Chem. Phys. **91**, 3571 (1989).

[26] D. T. Colbert and W. H. Miller. *A novel discrete variable representation for quantum mechanical reactive scattering via the S-matrix Kohn method.* J. Chem. Phys. **96**, 1982 (1992).

[27] D. J. Tannor. *Introduction to Quantum Mechanics: A Time-Dependent Perspective.* University Science Books, Sausalito (2007).

[28] T. B. Pedersen, J. L. Cacheiro, B. Fernández and H. Koch. *Rovibrational structure of the Ar–CO complex based on a novel three- dimensional ab initio potential.* J. Chem. Phys. **117**, 6562 (2002).

[29] TURBOMOLE V6.1 2009, a development of University of Karlsruhe and Forschungszentrum Karlsruhe GmbH, 1989-2007, TURBOMOLE GmbH, since 2007; available from `http://www.turbomole.com`.

[30] R. J. LeRoy. *Molecular Constants and Internuclear Potential of Ground-State Molecular Iodine.* J. Chem. Phys. **52**, 2683 (1970).

[31] R. F. Barrow and K. K. Yee. *$B\,^3\Pi_{0_u^+} \rightarrow X\,^1\Sigma_g^+$ system of $^{127}I_2$: rotational analysis and long-range potential in the $B\,^3\Pi_{0_u^+}$ state.* J. Chem. Soc., Faraday Trans. 2 **69**, 684 (1973).

[32] K. T. Tang and J. P. Toennies. *The van der Waals potentials between all the rare gas atoms from He to Rn.* J. Chem. Phys. **118**, 4976 (2003).

[33] T. Lenzer, M. R. Furlanetto, K. R. Asmis and D. M. Neumark. *Zero electron kinetic energy and photoelectron spectroscopy of the XeI-anion.* J. Chem. Phys. **109**, 10754 (1998).

[34] V. S. Batista and D. F. Coker. *Nonadiabatic molecular dynamics simulation of photodissociation and geminate recombination of I_2 liquid xenon.* J. Chem. Phys. **105**, 4033 (1996).

[35] V. S. Batista and D. F. Coker. *Nonadiabatic molecular dynamics simulation of ultrafast pump-probe experiments on I_2 in solid rare gases.* J. Chem. Phys. **106**, 6923 (1997).

[36] R. Böhling, J. Langen and U. Schurath. *A-X and A'-X progressions in dissociative excitation of matrix-isolated I_2: Rare gas effect on lifetimes and intensities.* Chem. Phys. **130**, 419 (1989).

[37] Z. Li R. Zadoyan, V. A. Apkarian and C. C. Martens. *Femtosecond Many-Body Dynamics of Caging: Experiment and Simulation of I_2 Photodissociation-Recombination in Solid Ar.* J. Phys. Chem. **99** (1995).

[38] Z. Bihary, R. B. Gerber and V. A. Apkarian. *Vibrational self-consistent field approach to anharmonic spectroscopy of molecules in solids: Application to iodine in argon matrix.* J. Chem. Phys. **115**, 2695 (2001).

[39] M. Bargheer, M. Gühr and N. Schwentner. *Depolarization as a probe for ultrafast reorientation of diatomics in condensed phase: ClF versus I_2 in rare gas solids.* J. Chem. Phys. **117**, 5 (2002).

[40] L. Onsager. *Electric Moments of Molecules in Liquids.* J. Am. Chem. Soc. **58**, 1486 (1936).

[41] M. E. Jacox. *Comparison of the electronic energy levels of diatomic molecules in the gas phase and in inert solid matrices.* J. Mol. Struct. **157**, 43 (1987).

[42] H. Friedmann and S. Kimel. *Theory of Shifts of Vibration-Rotation Lines of Diatomic Molecules in Noble-Gas Matrices. Intermolecular Forces in Crystals.* J. Chem. Phys. **43**, 3925 (1965).

[43] E. Hulkko. *Spectroscopic Signatures as a Probe of Structure and Dynamics in Condensed-Phase Systems – Studies of Iodine and Gold Ranging from Isolated Molecules to Nanoclusters.* Ph.D. thesis, University of Jyväskylä, Finland (2012).

[44] E. Hulkko, J. Ahokas, J. Lindgren, P. Myllyperkiö and M. Pettersson. *Electronic spectroscopy of I_2-Xe complexes in solid Krypton.* J. Chem. Phys. **136**, 174501 (2012).

[45] J. van Kranendonk. *Rotational and vibrational energy bands in solid hydrogen.* Physica **25**, 1080 (1959).

[46] J. van Kranendonk. *Theory of the infrared and Raman spectra of solid parahydrogen.* Can. J. Phys. **38**, 240 (1960).

[47] J. van Kranendonk and G. Karl. *Theory of the rotational and vibrational excitations in solid parahydrogen, and frequency analysis of the infrared and Raman spectra.* Rev. Mod. Phys. **40**, 531 (1968).

[48] J. van Kranendonk. *Solid Hydrogen.* Plenum Press, New York (1983).

[49] M. Vanhimbeeck, H. De Raedt, A. Lagendijk and D. Schoemaker. *Calculation of rotational T_2 relaxation in solid parahydrogen and orthodeuterium.* Phys. Rev. B **33**, 4264 (1986).

[50] E. Goovaerts, X. Y. Chen, A. Bouwen and D. Schoemaker. *Relaxation Times of $k = 0$ Rotons in Pure Parahydrogen Crystals and Roton Scattering by Orthohydrogen Impurities.* Phys. Rev. Lett. **57**, 479 (1986).

[51] X. Y. Chen, E. Goovaerts and D. Schoemaker. *Scattering-model calculation of the impurity-induced dephasing relaxation rates of the Raman-active $J = 2$ rotons in solid parahydrogen.* Phys. Rev. B **38**, 1450 (1988).

[52] C. Sierens, A. Bouwen, E. Goovaerts, M. De Mazière and D. Schoemaker. *Roton relaxation in parahydrogen crystals measured by time-resolved stimulated Raman gain.* Phys. Rev. A **37**, 4769 (1988).

[53] M. Leblans, A. Bouwen, C. Sierens, W. Joosen, E. Goovaerts and D. Schoemaker. *Dephasing relaxation of $J = 2$ rotons in parahydrogen crystals doped with hydrogen-deuterium impurities.* Phys. Rev. B. **40**, 6674 (1989).

[54] F. Königsmann. *Femtosecond spectroscopy of solid hydrogen: Long lived coherences in a molecular quantum crystal.* Ph.D. thesis, Freie Universität Berlin, Germany (2012).

[55] C. F. Coll III, A. B. Harris and A. J. Berlinsky. *Observation of libron-libron interactions in solid hydrogen.* Phys. Rev. Lett. **25**, 858 (1970).

[56] W. N. Hardy, I. F. Silvera and J. P. McTague. *Libron Spectra of Oriented Crystals of Paradeuterium and Orthohydrogen in the Ordered State.* Phys. Rev. Lett. **26**, 127 (1971).

[57] L. Khriachtchev, M. Pettersson, N. Runeberg, J. Lundell and M. Räsänen. *A stable argon compound.* Nature (London) **406**, 874 (2000).

[58] B. Fu, B. C. Shepler and J. M. Bowman. *Three-State Trajectory Surface Hopping Studies of the Photodissociation Dynamics of Formaldehyde on ab Initio Potential Energy Surfaces.* J. Am. Chem. Soc. **133**, 7957 (2011).

[59] C. B. Moore. *A spectroscopist's View of Energy States, Energy transfers, and Chemical Reactions.* Annu. Rev. Phys. Chem. **58**, 1 (2007).

[60] D. J. Clouthier and D. A. Ramsay. *The spectroscopy of Formaldehyde and Thioformaldehyde.* Annu. Rev. Phys. Chem. **34**, 31 (1983).

[61] C. B. Moore and J. C. Weisshaar. *Formaldehyde photochemistry.* Annu. Rev. Phys. Chem. **34**, 525 (1983).

[62] S. G. Thomas Jr. and W. A. Guillory. *Condensed-Phase Photochemistry of Formaldehyde.* J. Phys. Chem. **77**, 2469 (1973).

[63] J. R. Sodeau and E. K. C. Lee. *Intermediacy of hydroxymethylene ($H\ddot{C}OH$) in the low temperature matrix photochemistry of formaldehyde.* Chem. Phys. Lett. **57**, 71 (1978).

[64] M. Diem and E. K. C. Lee. *The role of the cage dimer of formaldehyde in the photolysis of formaldehyde: Argon matrix at 12 K.* Chem. Phys. **41**, 373 (1979).

[65] M. Diem and E. K. C. Lee. *Photooxidation of Formaldehyde in Solid Oxygen and Argon/Oxygen Matrices at 12 K.* J. Phys. Chem. **86**, 4507 (1982).

[66] K. J. Vaskonen and H. M. Kunttu. *Photodissociation of Formaldehyde in Rare Gas (Xe, Kr, Ar, and Ne) Matrixes.* J. Phys. Chem. A **107**, 5881 (2003).

[67] M. Péalat, D. Debarre, J.-M. Marie, J.-P. E. Taran, A. Tramer and C. B. Moore. *Cars study of vibrationally excited H_2 produced in formaldehyde dissociation.* Chem. Phys. Lett. **98**, 299 (1983).

[68] D. Debarre, M. Lefebvre, M. Péalat, J.-P. E. Taran, D. J. Bamford and C. B. Moore. *Photofragmentation dynamics of formaldehyde: $H_2(v, J)$ distributions.* J. Chem. Phys. **83**, 4476 (1985).

[69] J. Ahokas, H. Kunttu, Leonid Khriachtchev, M. Pettersson and M. Räsänen. *UV Photolysis and Thermal Annealing of H_2S, HI, and H_2CO in Solid Xe: Electronic Absorption Spectra of the Products.* J. Phys. Chem. A **106**, 7743 (2002).

[70] A. Olbert-Majkut, J. Ahokas, J. Lundell and M. Pettersson. *Raman spectroscopy of formic acid and its dimers isolated in low temperature argon matrices.* Chem. Phys. Lett. **468**, 176 (2009).

[71] A. Olbert-Majkut, J. Ahokas, J. Lundell and M. Pettersson. *Photolysis of HCOOH monomer and dimer in solid argon: Raman characterization of* in situ *formed molecular complexes.* Phys. Chem. Chem. Phys. **12**, 7138 (2010).

[72] S. Tam and M. E. Fajardo. *Observation of the high-resolution infrared absorption spectrum of CO_2 molecules isolated in solid parahydrogen.* Low Temp. Phys. **26**, 653 (2000).

[73] M. Fushitani, T. Shida, T. Momose and M. Räsänen. *UV-Photolysis of $HI \cdots CO_2$ Complexes in Solid Parahydrogen: Formation of CO and H_2O.* J. Phys. Chem. A **104**, 3635 (2000).

[74] A. G. Maki. *Infrared Spectra of Carbon Monoxide as a Solid and in Solid Matrices.* J. Chem. Phys. **35**, 931 (1961).

[75] H. Vu, M. R. Atwood and B. Vodar. *1-0, 2-0, 3-0, Absorption Bands of Dense Forms of Pure CO and Its Solutions in N_2 and Ar.* J. Chem. Phys. **38**, 2671 (1963).

[76] G. E. Leroi, G. E. Ewing and G. C. Pimentel. *Infrared Spectra of Carbon Monoxide in an Argon Matrix.* J. Chem. Phys. **40**, 2298 (1964).

[77] J. B. Davies and H. E. Hallam. *Infra-red cryogenic studies. Part 8.—Carbon monoxide in matrices.* J. Chem. Soc., Faraday Trans. 2 **68**, 509 (1972).

[78] H. Dubost and L. Abouaf-Marguin. *Infrared spectra of carbon monoxide trapped in solid argon. Double-doping experiments with H_2O, NH_3 and N_2.* Chem. Phys. Lett. **17**, 269 (1972).

[79] H. Dubost. *Infrared absorption spectra of carbon monoxide in rare gas matrices.* Chem. Phys. **12**, 139 (1976).

[80] H. Dubost, A. Lecuyer and R. Charneau. *Librational relaxation and IR line broadening of matrix isolated CO.* Chem. Phys. Lett. **66**, 191 (1979).

[81] G. J. Jiang, W. B. Person and K. G. Brown. *Absolute infrared intensities and band shapes in pure solid CO and CO in some solid matrices.* J. Chem. Phys. **62**, 1201 (1975).

[82] Y. Ogawara, A. Bruneau and T. Kimura. *Determination of ppb-Level CO, CO_2, CH_4, and H_2O in High-Purity Gases Using Matrix Isolation FT-IR with an Integrating Sphere.* Anal. Chem. **66**, 4354 (1994).

[83] A. Givan, A. Loewenschuss and C. J. Nielsen. *FTIR studies of CO–water complexes in argon matrices and in porous ices.* J. Chem. Soc., Faraday Trans. **92**, 4297 (1996).

[84] H. S. Han and K. Kim. *Optimum geometry of CO dimer and FT-IR spectra of CO in solid argon.* J. Mol. Struct.: THEOCHEM **418**, 1 (1997).

[85] H. Abe, H. Takeo and K. M. T. Yamada. *Infrared spectroscopy of CO trapped in an argon matrix revisited.* Chem. Phys. Lett. **311**, 153 (1999).

[86] D. T. Anderson and J. S. Winn. *Infrared Spectrum of Matrix-Isolated CO and CO Photoproduct from OCS Photolysis.* J. Chem. Phys. A **104**, 3472 (2000).

[87] H. Abe and K. M. T. Yamada. *Infrared spectra of the CO–H_2O 1–1 cluster trapped in an argon matrix.* J. Chem. Phys. **114**, 6134 (2001).

[88] H. Abe and K. M. T. Yamada. *Spectroscopic identification of the CO-H_2O 2-1 cluster trapped in an argon matrix.* J. Chem. Phys. **121**, 7803 (2004).

[89] L. M. Nxumalo, E. K. Ngidi and T. A. Ford. *The structures of some dimers of carbon monoxide—an infrared matrix isolation spectroscopic and ab initio molecular orbital study.* J. Mol. Struct. **786**, 168 (2006).

[90] J. Manz. *Rotating Molecules Trapped in Pseudorotating Cages.* J. Am. Chem. Soc. **102**, 1801 (1980).

[91] F. T. Prochaska and L. Andrews. *Vibration–rotational and pure rotational laser–Raman spectra of H_2, D_2, and HD in matrices at 12 K.* J. Chem. Phys. **67**, 1139 (1977).

[92] K. D. Bier, H. J. Jodl and H. Däufer. *Raman spectroscopy of matrix-isolated hydrogen: I. Influence of matrices on defects.* Can. J. Phys. **66**, 708 (1988).

[93] K. D. Bier, H. J. Jodl and H. Däufer. *Raman spectroscopy of matrix-isolated hydrogen: I. Influence of defects on matrices.* Can. J. Phys. **66**, 716 (1988).

[94] M. E. Alikhani, B. Silvi, J. P. Perchard and V. Chandrasekharan. *Reinvestigation of the Raman spectra of dihydrogen trapped in rare gas solids. I. H_2, HD, and D_2 monomeric species.* J. Chem. Phys. **90**, 5221 (1989).

[95] E. Alikhani, L. Manceron and J. P. Perchard. *Raman matrix isolation spectroscopy of hydrogen. III. Aggregation processes in solid krypton.* Chem. Phys. **140**, 51 (1990).

[96] M. E. Alikhani, L. Manceron, J. P. Perchard and B. Silvi. *Raman matrix isolation spectroscopy of hydrogen trapped in rare gases: from monomer to high aggregation states.* J. Mol. Struct. **222**, 185 (1990).

[97] M. E. Alikhani, L. Manceron and J. P. Perchard. *Raman matrix isolation spectroscopy of dihydrogen. II. Aggregation processes in argon.* J. Chem. Phys. **92**, 22 (1990).

[98] A. Kornath, A. Zoermer and I. Köper. *Raman spectroscopic studies on matrix-isolated hydrogen and deuterium. 3. Molecular dynamics in matrices.* Spectrochim. Acta, Part A **55**, 2593 (1999).

[99] L. Pauling. *The Rotational Motion of Molecules in Crystals.* Phys. Rev. **36**, 430 (1930).

[100] A. F. Devonshire. *The Rotation of Molecules in Fields of Octahedral Symmetry.* Proc. R. Soc. Lond. A **153**, 601 (1936).

[101] R. E. Miller and J. C. Decius. *Group theory for matrix isolated molecules in static crystal fields.* J. Chem. Phys. **59**, 4871 (1973).

[102] C. Bissonnette, C. E. Chuagai, K. G. Crowell, R. J. Le Roy, R. J. Wheatley and W. J. Meath. *A reliable new potential energy surface for H_2–Ar.* J. Chem. Phys **105**, 2639 (1996).

[103] P. Jankowski and K. Szalewicz. *A new ab initio interaction energy surface and high-resolution spectra A new ab initio interaction energy surface and high-resolution spectra of the H_2–CO van der Waals complex.* J. Chem. Phys. **123**, 104301 (2005).

[104] J. A. Coxon and P. G. Hajigeorgiou. *Direct potential fit analysis of the $X\ ^1\Sigma^+$ ground state of CO.* J. Chem. Phys. **121**, 2992 (2004).

[105] J. J. Barrett. *Generation of coherent anti-Stokes rotational Raman radiation in hydrogen gas.* Appl. Phys. Lett. **29**, 722 (1976).

[106] T. Kiljunen, M. Bargheer, M. Gühr, N. Schwentner and B. Schmidt. *Photodynamics and ground state librational states of ClF molecule in solid Ar. Comparison of experiment and theory.* Phys. Chem. Chem. Phys. **6**, 2932 (2004).

[107] B. Schmidt and P. Zdanska. *Solution of the time-dependent Schrödinger equation for highly symmetric potentials.* Comp. Phys. Comm. **127**, 290 (2000).

[108] R. W. Robinett. *Quantum wave packet revivals.* Phys. Rep. **392**, 1 (2004).

[109] B. M. Garraway and K. A. Suominen. *Wave-packet dynamics: new physics and chemistry in femto-time.* Rep. Prog. Phys. **58**, 365 (1995).

[110] M. D. Feit, J. A. Fleck Jr. and A. Steiger. *Solution of the Schrödinger equation by a spectral method.* J. Comput. Phys. **47**, 412 (1982).

[111] S. Mukamel. *The Principles of Nonlinear Optical Spectroscopy.* Oxford University Press, New York (1995).

[112] V. May and O. Kühn. *Charge and Energy Transfer Dynamics in Molecular Systems.* Wiley-VCH, Weinheim, third edition (2011).

[113] R. Kubo. *A stochastic theory of line shape.* Adv. Chem. Phys. **15**, 101 (1969).

[114] P. Hamm and M. Zanni. *Concepts and Methods of 2D Infrared Spectroscopy.* Cambridge University Press, Cambridge, UK (2011).

[115] E. Hulkko, J. Lindgren, T. Kiljunen and M. Pettersson. *Long-Lived Electronic Coherence of Iodine in the Condensed Phase: Sharp Zero-Phonon Lines in the $B \leftrightarrow X$ Absorption and Emission of I_2 in Solid Xe.* J. Phys. Chem. Lett. **3**, 1847 (2012).

[116] Z. Bihary, R. Zadoyan, M. Karavitis and V. A. Apkarian. *Dynamics and the breaking of a driven cage: I_2 in solid Ar.* J. Chem. Phys. **120**, 7576 (2004).

[117] D. Segale, M. Karavitis, E. Fredji and V. A. Apkarian. *Quantum coherent dissipation: A glimpse of the "cat".* J. Chem. Phys. **122**, 111104 (2005).

[118] D. Segale and V. A. Apkarian. *Dissipative quantum coherent dynamics probed in phase-space: Electronically resonant 5-color 4-wave mixing on $I_2(B)$ in solid Kr.* J. Chem. Phys. **135**, 024203 (2011).

[119] Soo-Y. Lee and E. J. Heller. *Time-dependent theory of Raman scattering.* J. Chem. Phys. **71**, 4777 (1979).

[120] E. J. Heller, R. L. Sundberg and D. Tannor. *Simple Aspects of Raman Scattering.* J. Phys. Chem. **86**, 1822 (1982).

[121] D. L. Rousseau and P. F. Williams. *Resonance Raman scattering of light from diatomic molecule.* J. Chem. Phys. **64**, 3519 (1976).

[122] P. Jungwirth, E. Fredji and R. B. Gerber. *Ultrafast quantum dynamics and resonance Raman spectroscopy of photoexcited $I_2(B)$ in large argon and xenon clusters.* J. Chem. Phys. **104**, 9332 (1996).

[123] J. M. Grzybowski and L. Andrews. *Resonance Raman effect in matrix isolated photolytically produced monomeric iodine: An investigation of the excitation profiles of the overtones.* J. Raman Spectrosc. **4**, 99 (1975).

[124] J. Xu, N. Schwentner and M. Chergui. *Femtosecond dynamics of $I_2(B\,^3\Pi_{0_u^+})$ in liquids from resonance Raman spectra.* J. Chem. Phys. **101**, 7381 (1994).

[125] J. Xu, N. Schwentner, S. Hennig and M. Chergui. *Ultrafast Dynamics of the B state of I_2 in Condensed Rare Gases.* J. Chim. Phys. **92**, 541 (1995).

[126] M. Lamrini, R. Bacis, D. Cerny, S. Churassy, P. Crozet and A. J. Ross. *The electronic transition dipole moment of the $B0_u^+ \rightarrow X0_g^+$ transition in iodine.* J. Chem. Phys. **100**, 8780 (1994).

[127] J. Faeder, I. Pinkas, G. Knopp, Y. Prior and D. J. Tannor. *Vibrational polarization beats in femtosecond coherent anti-Stokes Raman spectroscopy: A signature of dissociative pump–dump–pump wave packet dynamics.* J. Chem. Phys. **115**, 8440 (2001).

[128] D. J. Tannor, S. A. Rice and P. M. Weber. *Picosecond CARS as a probe of ground electronic state intramolecular vibrational redistribution.* J. Chem. Phys. **83**, 6158 (1985).

[129] T. Kiviniemi, T. Kiljunen and M. Pettersson. *Femtosecond coherent anti-Stokes Raman-scattering polarization Femtosecond coherent anti-Stokes Raman-scattering polarization beat spectroscopy of I_2–Xe complex in solid krypton.* J. Chem. Phys. **125**, 164302 (2006).

[130] T. Kiviniemi, E. Hulkko and M. Pettersson. *Impulsive excitation of high vibrational states in I_2–Xe complex on the electronic ground state.* Chem. Phys. Lett. **491**, 44 (2010).

[131] T. Kiviniemi, E. Hulkko, T. Kiljunen and M. Pettersson. *Iodine-Benzene Complex as a Candidate for a Real-Time Control of a Bimolecular Reaction. Spectroscopic Studies of the Properties of the 1:1 Complex Isolated in Solid Krypton.* J. Phys. Chem. A **113**, 6326 (2009).

[132] S. Meyer, M. Schmitt, A. Materny, W. Kiefer and V. Engel. *A theoretical analysis of the time-resolved femtosecond CARS spectrum of I_2.* Chem. Phys. Lett. **281**, 332 (1997).

[133] R. Zadoyan and V.A. Apkarian. *Imaging the molecular rovibrational coherence through time-gated frequency-resolved coherent anti-Stokes Raman scattering.* Chem. Phys. Lett. **326**, 1 (2000).

[134] R. Zadoyan, D. Kohen, D.A. Lidar and V.A. Apkarian. *The manipulation of massive ro-vibronic superpositions using time-frequency-resolved coherent anti-Stokes Raman scattering (TFRCARS): from quantum control to quantum computing.* Chem. Phys. **266**, 323 (2001).

[135] R. Lausten, O. Smirnova, B. J. Sussman, S. Gräfe, A. D. Mouritzen and A. Stolow. *Time- and frequency-resolved coherent anti-Stokes Raman scattering spectroscopy with sub-25 fs laser pulses.* J. Chem. Phys. **128**, 244310 (2008).

[136] S. Meyer, M. Schmitt, A. Materny, W. Kiefer and V. Engel. *Simulation of femtosecond time-resolved four-wave mixing experiments on I_2.* Chem. Phys. Lett. **301**, 248 (1999).

[137] S. Meyer and V. Engel. *Non-perturbative wave-packet calculations of time-resolved four-wave-mixing signals.* Appl. Phys. B **71**, 293 (2000).

[138] S. Meyer and V. Engel. *Femtosecond time-resolved CARS and DFWM spectroscopy on gas-phase I_2: a wave-packet description.* J. Raman Spectrosc. **31**, 33 (2000).

[139] B. E. Wurfel, G. Schallmoser, G. Lask, J. Agreiter, A. Thoma, R. Schlachta and V. E. Bondybey. *Infared fluorescence and absorption studies of CN: spectra and relaxation in solid rare gases.* Chem. Phys. **174**, 255 (1993).

[140] G. Schallmoser, A. Thoma, B. E. Wurfel and V. E. Bondybey. *Rotation of CN in solid rare gases.* Chem. Phys. Lett. **219**, 101 (1994).

[141] A. Thoma, G. Schallmoser, A. M. Smith, B. E. Wurfel and V. E. Bondybey. *Visible absorption and infrared emission of CN-Xe in an argon matrix.* J. Chem. Phys. **100**, 5387 (1994).

[142] T. Seideman. *On the dynamics of rotationally broad, spatially aligned wave packets.* J. Chem. Phys. **115**, 5965 (2001).

[143] T. Seideman and E. Hamilton. *Nonadiabatic alignment by intense pulses. Concepts, theory, and directions.* Adv. At. Mol. Opt. Phys. **52**, 289 (2005).

[144] M. Morgen, W. Price, L. Hunziker, P. Ludowise M. Blackwell and Y. Chen. *Femtosecond Raman-induced polarization spectroscopy studies of rotational coherences in O_2, N_2 and CO_2.* Chem. Phys. Lett. **209**, 1 (1995).

[145] M. Morgen, W. Price, P. Ludowise and Y. Chen. *Tensor analysis of femtosecond Raman induced polarization spectroscopy: Application to the study of rotational coherences.* J. Chem. Phys. **102**, 8780 (1995).

[146] Y. J. Yan and S. Mukamel. *Pulse shaping and coherent Raman spectroscopy in condensed phases.* J. Chem. Phys. **94**, 997 (1991).

[147] S. Constantine, Y. Zhou, J. Morais and L. D. Ziegler. *Dispersed Optical Heterodyne Detected Birefringence and Dichroism of Transparent Liquids.* J. Phys. Chem. A **101**, 5456 (1997).

[148] Y. Zhou, S. Constantine, S. Harrel and L. D. Ziegler. *The probe frequency dependence of nonresonant femtosecond pump–probe nuclear responses: Undercutting vibrational inhomogeneities.* J. Chem. Phys. **110**, 5893 (1999).

[149] M. Gühr, M. Bargheer, M. Fushitani, T. Kiljunen and N. Schwentner. *Ultrafast dynamics of halogens in rare gas solids.* Phys. Chem. Chem. Phys. **9**, 779 (2007).

[150] E. T. Branigan, N. Halberstadt and V. A. Apkarian. *Solvation dynamics through Raman spectroscopy: Hydration of Br_2 and Br_3^-, and solvation of Br_2 in liquid bromine.* J. Chem. Phys. **134**, 174503 (2011).

[151] M. Ovchinnikov and V. A. Apkarian. *Condensed phase spectroscopy from mixed-order semiclassical molecular dynamics: Absorption, emission, and resonant Raman spectra of I_2 isolated in solid Kr.* J. Chem. Phys. **105**, 10312 (1996).

[152] M. Ovchinnikov and V. A. Apkarian. *Quantum interference in resonant Raman spectra of I_2 in condensed media.* J. Chem. Phys. **106**, 5775 (1997).

[153] M. Ovchinnikov, V. A. Apkarian and G. A. Voth. *Semiclassical molecular dynamics computation of spontaneous light emission in the condensed phase: Resonance Raman spectra.* J. Chem. Phys. **114**, 7130 (2001).